Unsteady Aerodynamic/Hydrodynamic Analysis of Bio-inspired Flapping Elements at Low Reynolds Number

Hisham M. Shehata

Dissertation submitted to the Faculty of the
Virginia Polytechnic Institute and State University
in partial fulfillment of the requirements for the degree of

Doctor of Philosophy
in
Engineering Mechanics

Muhammad R. Hajj, Co-chair
Craig A. Woolsey, Co-chair
Saad A. Ragab
Mayuresh J. Patil
Haithem E. Taha

February 19, 2020
Blacksburg, Virginia

Keywords: Unsteady Aerodynamic, Hydrodynamic, Low Reynolds number, Frequency response, Flexibility, Pisciform Locomotion

Unsteady Aerodynamic/Hydrodynamic Analysis of Bio-inspired Flapping Elements at Low Reynolds Number

Hisham M. Shehata

(ABSTRACT)

The impressive kinematic capabilities and structural adaptations presented by bio-locomotion continue to inspire some of the advancements in today's small-scaled flying and swimming vehicles. These vehicles operate in a low Reynolds number flow regime where viscous effects dominate flow interactions, which makes it challenging to generate lift and thrust. Overcoming these challenges means utilizing non-conventional lifting and flow control mechanisms generated by unsteady flapping body motion. Understanding and characterizing the aerodynamic phenomena associated with the unsteady motion is vital to predict the unsteady fluid loads generated, to implement control methodologies, and to assess the dynamic stability and control authority of airborne and underwater vehicles. This dissertation presents experimental results for forced oscillations on multi-element airfoils and hydrofoils for Reynolds numbers between $Re = 10^4$ and $Re = 10^6$. The document divides the work into four main sections: The first topic presents wind tunnel measurements of lift forces generated by an oscillating trailing edge flap on a NACA-0012 airfoil to illustrate the effects that frequency and pitching amplitude have on lift enhancement. The results suggest that this dynamic trailing edge flap enhances the mean lift by up to 20% in the stalled flow regime. Using frequency response approach, it is determined that the maximum enhancement in circulatory lift amplitude occurs at stalled angles of attack for lower pitching amplitudes. The second topic presents wind tunnel measurements for lift and drag generated by a sinusoidal and non-sinusoidal oscillations of a NACA-0012 airfoil. The results show that 'trapezoidal' pitching enhances the mean lift and the RMS lift by up to 50% and 35% in the pre-stall flow regime, respectively, whereas the 'reverse sawtooth' and sinusoidal pitching generate the most substantial increase of the lift-to-drag ratio in stall and post-stall flow regimes, respectively. The third topic involves a study on the role of fish-tail flexibility on thrust and propulsive efficiency. Flexible tails enhance thrust production in comparison to a rigid ones of the same size and under the same operating conditions. Further analysis indicates that varying the tail's aspect ratio has a more significant effect on propulsive efficiency and the

thrust-to-power ratio at zero freestream flow. On the other hand, changing the material's property has the strongest impact on propulsive efficiency at non-zero freestream flow. The results also show that the maximum thrust peaks correspond to the maximum passive tail amplitudes only for the most flexible case. The final topic aims to assess the unsteady hydrodynamic forces and moments generated by a three-link swimming prototype performing different swimming gaits, swimming speeds, and oscillatory frequencies. We conclude that the active actuation of the tail's first mode bending produces the most significant thrust force in the presence of freestream flow. In contrast, the second mode bending kinematics provides the most significant thrust force in a zero-freestream flow.

Unsteady Aerodynamic/Hydrodynamic Analysis of Bio-inspired Flapping Elements at Low Reynolds Number

Hisham M. Shehata

(GENERAL AUDIENCE ABSTRACT)

It is by no surprise that animal locomotion continues to inspire the design of flying and swimming vehicles. Although nature produces complex kinematics and highly unsteady flow characteristics, simplified approximations to model bio-inspired locomotion in fluid flows are experimentally achievable using low degrees of freedom motion, such as pitching airfoils and trailing edge flaps. The contributions of this dissertation are divided into four primary foci: (a) wind tunnel force measurements on a flapped NACA-0012 airfoil undergoing forced pitching, (b) wind tunnel measurements of aerodynamic forces generated by sinusoidal and non-sinusoidal pitching of a NACA-0012 airfoil, (c) towing tank measurements of thrust forces and torques generated by a one-link swimming prototype with varying tail flexibilities, and (d) towing tank measurements of hydrodynamic forces and moments generated by active tail actuation of a multi-link swimming prototype. From our wind tunnel measurements, we determine that lift enhancement by a trailing edge flap is achieved under certain flow regimes and oscillating conditions. Additionally, we assess the aerodynamic forces for a sinusoidal and non-sinusoidal pitching of an airfoil and show that 'trapezoidal' pitching produces the largest lift coefficient amplitude whereas the sinusoidal and 'reverse sawtooth' pitching achieve the best lift to drag ratios. From our towing tank experiments, we note that the role of tail flexibility enhances thrust generation on a swimming device. Finally, we conclude that different kinematics on an articulating body strongly affect the hydrodynamic forces and moments. The results of the towing tank measurements are accessible from an online public database to encourage research and contribution in underwater vehicle design through physics-based low-order models that can accommodate hydrodynamic principles and geometric control concepts.

Dedication

In dedication to my wife Dalya, mother Amani, father Mohamed, sister Nariman, and my dearest and beloved son Adam, who made his way into this world in the summer of 2018.

Acknowledgments

I would first like to thank my advisors, Dr. Muhammad Hajj and Dr. Craig Woolsey, for their immeasurable support and guidance. I began research under Dr. Hajj, and throughout my time as a student, collaborative work with Dr. Woolsey has been of considerable importance to my graduate education. Both individuals were persistent and constructive in making me into a better researcher and an effective writer.

I would like to extend a sincere gratitude to the rest of my committee members: Dr. Saad Ragab, Dr. Mayuresh Patil, and Dr. Haithem Taha, for their continuous support, and for adding valuable contributions to the improvement of my research.

I appreciated all the discussions I had with Dr. Mohamed Zakaria, and the time spent with my research group: Dr. Ahmed Hussein, Dr. Jamal Alrowaijeh, Saeed Al Nuaimi, Vamsi Chandra, Guillermo Gonzalez and Amir Rezai. I want to extend an appreciation to the team of undergraduates, who made a substantial contribution to the experimental work of this dissertation. The team includes Alex McLean, Khanh Nguyen, Charles Watson, Lt. Luke Bergeron, Ahmed Nayfeh, Matthew Young, Minh Vu, and Jeremy Smith.

Furthermore, I would like to thank my in-laws, Professor Nabil Ismael and Professor Seham Darwish, for sharing their experience and words of wisdom about the academic world.

I would like to thank the administrative staff at the departments of Biomedical Engineering and Mechanics (BEAM) and Aerospace and Ocean Engineering (AOE) for their assistance in getting me through the process of graduate education.

Lastly, I would like to thank the Department of Engineering Mechanics for sponsoring my first year of Ph.D. working as a Graduate Teaching Assistant, the National Science Foundation (NSF) [1] for sponsoring the rest of my graduate education, and the Graduate School at

[1] Grant Number: CMMI-1635143

Virginia Tech for providing me with supplementary support through the GRDP Scholarship.

Contents

List of Figures

List of Tables

List of Abbreviations

α_{A} Pitching amplitude (deg)

$\alpha(t)$ Pitching trajectory

β Flexural Rigidity

δ_0 Mean flap deflection angle (deg)

δ_{A} Flap deflection amplitude (deg)

δ_{TE} Static flap deflection angle (deg)

η_{P} Propulsive efficiency

μ Mass ratio

ω Angular frequency (rad/s)

ϕ Phase angle (rad)

ρ Fluid density (kg/m^3)

τ_{PF} Panel-free torque (Ncm)

τ_H Hydrodynamic torque (Ncm)

τ_T Total torque (Ncm)

A_{p} Tail peak amplitude

a Airfoil pitching point relative to leading edge (m)

b Airfoil semi-chord, $c/2$ (m)

c Airfoil chord length (m)

C_D Drag coefficient

C_L Lift coefficient

C_{M_z} Yaw moment coefficient

$C_{\mathcal{P}}$ Power coefficient

$C_{\mathcal{T}}$ Thrust coefficient

C_x Axial force coefficient

C_y Side force coefficient

$C(k)$ Lift deficiency factor

e Flap hinge location, % semichord

E Young's modulus (Pa)

F_x Axial force (N)

F_y Side Force (N)

f Forcing frequency (Hz)

G Gain function

k Reduced frequency, $\pi f c/U_\infty$

l Lift force per unit span (N/m)

M_z Yaw moment (Ncm)

$\mathcal{P}$ Power (W)

Re Reynolds number

S Wing/body span (m)

$\mathcal{T}$ Thrust Force (N)

T Period

t Time (s)

U_{p} Tail peak velocity (m/s)

U_∞ Free stream velocity (m/s)

U_{ref} Reference velocity (m/s)

Chapter 1

Introduction

The ability of birds to fly or hover by flapping their wings and fish to swim and maneuver by flapping their tails has generated interest in using flapping wings, control surfaces, and tails to enhance lift, generate propulsion and improve an operating vehicle's overall system efficiency. The biological creatures have inspired an interest in modeling unsteady hydrodynamic and aerodynamic forces on pitching, plunging and surging airfoils. The modeling can be performed at different levels of fidelity. The high-fidelity models yield accurate results but involve many degrees of freedom, which make them computationally expensive. Additionally, few simulations may not provide an accurate physical insight into the relative roles of the different aspects of the flow, and the coupled dynamics between the fluid and the flapping element. Alternatively, simplified reduced-order models of unsteady loads generated by such elements can be effective in aeroelastic or hydrodynamic stability analysis, implementation of a control strategy, and uncertainty quantification and sensitivity analysis within the context of multi-disciplinary optimization.

Conventional flow control techniques can be impractical to utilize on small-scaled vehicles due to weight and space constraints. The unsteady aerodynamic phenomena that allow birds and fish to operate efficiently at low Reynolds numbers are produced by non-conventional mechanisms such as pitching and flapping. Non-conventional active flow control mechanisms can be used to utilize the fluid-structure interactions to delay stall, increase lift, and control separated flow. The intrinsically unsteady characteristic of flapping kinematics is the primary

source of force production and distinguishes unsteady-element motion from conventional rotary and fixed element configurations.

The effects of low Reynolds number on the fluid response of flapping-element motion require more considerable attention due to flow transition effects from laminar to turbulent flow regimes. Additionally, flow behavior around airfoils at these low Reynolds numbers can result in unsteady flow phenomena that include laminar flow separation, vortical flows, and associated non-linearities such as hysteresis effects; these dynamics can make lift and thrust generation challenging due to the strong viscous interactions that take place.

It is essential in low Reynolds numbers flow to understand the impact of an element performing unsteady motion on aerodynamic/hydrodynamic performance in the study of flapping-wing flights of birds and flapping-tail motions of fish. As such, we can utilize quasi-steady and unsteady models that can capture general trends of unsteady forces to aid the preliminary design of flow control devices on small Unmanned Ariel Vehicles (UAV), Micro-Air Vehicles (MAV), and Autonomous Underwater vehicles (AUV). The accuracy and reliability of the unsteady fluid models rely heavily on the extension of strictly quasi-steady models that incorporate unsteady flow parameters which are determined from computational and experimental work.

The complicated wing or tail kinematics presented by animal bio-locomotion is highly dimensional and represent a large number of degrees of freedom. We use pitching airfoils, trailing edge flaps and, rigid and deformable hydrofoils as simplified models for bio-inspired motion. This dissertation presents force measurements conducted on elements undergoing forced oscillations in flow regimes between $Re = 10^4$ and 10^6. The scope of the work is divided into several sections. This introductory chapter presents a literature review, discusses the motivation behind the work, and delivers a statement of motivation and contributed work for each chapter. The next two chapters present wind tunnel measurements for lift and drag

forces in different flow states and forced oscillatory conditions generated by a pitching trailing edge flap (TEF) of a NACA-0012 airfoil with a fixed leading-element, and a NACA-0012 airfoil undergoing sinusoidal and non-sinusoidal pitching at $Re = 2.1 \times 10^4$. The following two chapters present water towing tank measurements for thrust and torque generated by flapping a deformable tail with varying flexibilities by a one-link pisciform prototype, and by a multi-link prototype called *Modular Biolocomotion Emulator* (MBE) performing different forced swimming gaits. The measurements were taken for a variety of towing speeds corresponding to length-based Reynolds numbers between $Re = 1.4 \times 10^5$ and $Re = 4.8 \times 10^5$, and for a parametric space that covers a wide range of oscillatory inputs.

1.1 Literature Review

Non-conventional lifting mechanisms involving unsteady airfoil motion have been recently proposed to enhance lift performance, improve flight stability, and provide better control for flying vehicles. Exploiting these mechanisms requires accurate modeling of the associated unsteady aerodynamics and control laws. Early into the 20^{th} century, the step and frequency response functions were used to model the unsteady aerodynamics of maneuvering airfoils. The analytical representations done by Wagner [1], Prandtl [2], Theodorsen [3] and Garrick [4] provide some fundamental physics of unsteady fluid flows. These representations in a potential flow framework and small disturbance theory yielded analytical expressions of aerodynamic forces and moments, and they remain useful to capture general trends in aerodynamic response for unsteady airfoil motions. In these representations, the forces are usually split into two components: an added mass term, and a circulatory term. The first is a non-circulatory component that consists of the pressure-induced forces and moments due to the element's acceleration relative to the fluid. The second is a non-circulatory component associated with the vorticity field in the wake.

In addition to analytical representations, extensions of strictly quasi-steady models were constructed, and semi-empirical methodologies were implemented to provide an approximate representation of the unsteady non-linear aerodynamics (Taha et al. [5], Taha and Rezaei [6], Brunton and Rowley [7], and Leishman [8]). These unsteady models made use of quasi-steady parameters and static experimental data to account for LEV contribution, rotational effects, low Reynolds number effects, and time lag in flow response. For instance, Rao et al. [9] introduced an empirical delay parameter into the effective angle of attack relationship to extend a viscous-inviscid interaction method to dynamic stall.

Unsteady aerodynamics can result from several independent or combined airfoil motions such

as pitching [10, 11], plunging [12, 13, 14, 15], and surging [16]. The effects of an oscillating airfoil can lead to delayed flow separation [17, 18, 19], enhanced flow reattachment [20, 21], and higher lift production [22, 23, 24], giving rise to the formation of passive non-conventional flow control mechanisms such as dynamic stall [25, 26, 27], leading edge vortex (LEV) [28, 29], suction, [30, 31], and vortex trapping [32, 33].

1.1.1 Pitching Flapped Airfoils

Movable trailing edge flaps (TEFs) have been proposed for flow control to improve aerodynamic performance [34, 35, 36]. A statically extended trailing edge flap can indeed achieve enhanced lift, but that lift is often accompanied by a drag penalty. Oscillating flaps, on the other hand, serve a beneficial role by increasing lift without a measurable increase in the drag. More recently, TEFs have been commonly used to mitigate flow separation by gaining flow authority over the boundary layer usually by disrupting the flow instabilities in the separated shear layers and near body wake vortices [37]. In specific, the concept of oscillating a TEF is to enhance the reattachment process of boundary layer separation over the wing. TEF oscillation can overcome and withstand the adverse pressure gradient by energizing the boundary layer [38]. Vortices created by oscillating TEF can induce additional pressure difference that will enhance the momentum transfer from the free stream flow to the upstream boundary layer. This process leads to a flow reattachment (or in other words, delays separation), and achieves higher lift production [39]. The further upstream the reattachment takes place, the higher is the maximum lift coefficient that can be reached [40]. Flap oscillations can also restrain trailing-edge flow separation and prevent the separation point from moving upstream to the airfoil. Figure 1.1 shows dye visualization results reported by Medina and Hemati [41] on a dynamic deflection of a flap on a NACA-0006 at $Re = 4 \times 10^4$. In a nominally separated flow regime, the dynamic flap deflection gives rise

to a dynamic stall event, i.e., LEV roll-up, and the formation of trailing edge vortices.

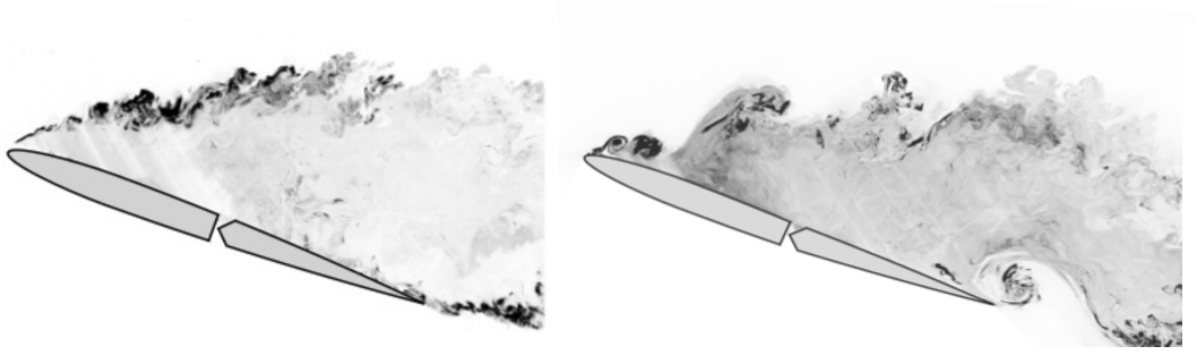

Figure 1.1: Dye visualization of a static NACA- 0006 airfoil at 20° AoA (left) and a NACA-0006 airfoil at 20° AoA with a 2° dynamic and downward flap deflection (right). Test conditions: 6 Hz actuation, convective time, $\Delta t U_\infty/c$=0.5. (Copyright permission obtained)

Analytical work

Most analytical studies on airfoils are extensions of classical aerodynamic theories developed by Theodorsen [3], and Wagner [1]. There are a few analytical studies on the lift enhancement generated by flapped airfoils. Leishman [8] derived an unsteady aerodynamic theory for an airfoil due to an arbitrary motion of a TEF. The theory was derived from Theodorsen's solution of the lift force for a rigid and thin airfoil undergoing oscillatory forcing. With the addition of a TEF hinged at a distance from the airfoil's mid chord, superimposed forces and moments as a function of the flap's size relative to the airfoil's chord can be formulated. Leishman further extended the theory in state-space form by employing Duhamel superposition principle and utilizing an improved exponential approximation to Wagner's indicial lift function. Taha et al. [5] constructed a state-space model also by extending Duhamel's superposition principle from classical unsteady theory. The state-space model allows a quasi-steady circulation as a state variable input integrated with Wagner's step response to output

the non-linear effects of LEV as a result of lift modulation due to the input of an arbitrary motion.

Numerical work

Xu et al. [42] optimized the configuration of a trailing edge with an additional hinged flap in motion using an adjoint-based approach to model a flexible/morphing wing in hovering flight at $Re = 100$. A 2-D immersed boundary computational method was used to solve the incompressible Navier Stokes equations on the optimized flapping configuration. Simulations indicated that the lift enhancement by the trailing edge flapping was due to a change in local circulation caused by (a) the rotation motion of the flap and (b), the modulation of trailing edge vortex shedding process as a result of the relative motion between the primary trailing edge element and the secondary TEF.

Feszty et al. [35] considered a 15%-chord dynamic flap on a NACA-0012 airfoil at $Re = 1.46 \times 10^5$ and reduced frequency, k, of 0.173 oscillating around 15° mean AoA, and 10° pitching amplitude. They performed numerical simulations and discovered that the nose-down pitching moment could be reduced using pulsed TEF motions. Furthermore, the formation of the trailing edge vortex induced the convection of LEV further downstream towards the trailing edge and the wake. This flow mechanism was the main effect behind the significant negative pitch moment and negative aerodynamic damping.

Experimental work

In addition to the numerical and theoretical developments mentioned above, the experiments by Greenhalgh [43, 44] describes the design of a wing mechanism with an oscillating flap to improve the lifting capability of the wing for modern aircraft design. The effects of oscillating

the 14.4% chord's flapped airfoil with pitching amplitudes of 12° resulted in an increase in lift coefficient over a modified reduced frequency range between 0.04 and 0.048. Lift enhancement of up of 54% was reported for a modified reduced frequency of 0.048 and an 8° increase in the angle at which the maximum lift occurred. The oscillating airfoil produced substantial lift enhancement in the +10° to +20° angle-of-attack range without a noticeable increase in drag. This improved lift to drag ratio was recorded for all tested mean AoAs.

Lee and Gerontakos [45] and Gerontakos and Lee [46] performed surface pressure distributions and PIV of an oscillating NACA-0015 airfoil with a 25%-chord dynamic TEF executing a similar pulsed flap motion employed by Feszty et al. [35] at $Re = 1.65 \times 10^5$, $k = 0.1$, and deep-stall flow condition. A linear ramp-up motion followed by a steady hold then a linear ramp-down motion was the prescribed pulse motion. The most significant finding from both studies was the substantial reduction in the nose-down pitching moment during the flap's upstroke motion. They also showed that LEV formation and detachment were not affected, although low-pressure trails of the LEV was the main cause of a loss of dynamic lift during an upstroke TEF motion. Also, no TEV was observed during the upstroke motion. Neither did it render any significant changes in the formation and detachment of the LEV during the downstroke motion. Using the same airfoil profile, Lee [47] considered the impact of TEF motion on hysteresis effects at $k = 0.1$ and $Re = 1.65 \times 10^5$ in attached flow and light-stall flow conditions. The flap performed a 6° pitching amplitude at mean AoA's of 12° and 14°. The effects of actuation start points relative to the periodic motion played a significant role in vortex evolution, and discovered that an actuation point from an upstroke flap position could cause the improved trade-off between reducing the nose-down pitching moment and maximizing the dynamic lift. The authors asserted that the TEF motion did not render a strong influence on the initiation, growth, and detachment of the LEV. During the downstroke motion, positive camber effects caused a measurable increase in maximum

lift coefficient but promoted a large nose-down pitching moment. At all mean angles of attack, no phase shift in transient the LEV effects were noticed in both attached and light stall oscillations. Lift coefficient hysteresis was observed during the downstroke TEF motion, which also created an increase in positive damping.

Medina and Rockwood [48] performed fluorescent dye visualization on a harmonically pitching 50%-chord TEF of a NACA-006 airfoil at $Re = 4 \times 10^4$ and AoA's of 10° and 20°. The results showed that one half stroke motion of the TEF at 1° amplitude and 6 Hz presented a significant roll up of the separated shear layer at $\alpha_0 = 10°$ and $\alpha_0 = 20°$. The authors further investigated the effects of harmonic flap oscillation with a 1° pitching amplitude at 0.13, 0.175, 0.21 Strouhal numbers, and 10° mean AoA. At these set frequencies and pitching amplitudes, the influence of the sinusoidal pitching motion did not impose as much flow authority over the shedding pattern in the near wake as was seen for the rapid deflection case. Between the tested actuation rates, there was a general trend of increasing lift amplitude with increasing Strouhal number. An increase of Strouhal number from 0.13 to 0.175 and 0.21 caused an increase in lift amplitudes by 10.2% and 16.7%, respectively.

1.1.2 Non-sinusoidal Pitching Airfoils

The most traditional form of pitching with readily available literature is the sinusoidal form. On the other hand, varying oscillatory parameters to achieve non-sinusoidal oscillations of airfoils can generate different wing kinematics and is an opportunity to produce complex LEV and TEV vortex patterns whose fluid-structure interactions are worthy of investigation.

Experimental work

Ol et al. [49] investigated the evolution of vortex shedding on an SD-7003 airfoil undergoing sinusoidal, trapezoidal, and triangular pitching at 20° amplitude and $Re = 1 \times 10^4$. Their results showed that trapezoidal pitching generated the highest amplitude of lift coefficient and was associated with the largest LEV associated with the three airfoil kinematics. Additionally, the trapezoidal pitching resulted in a pairing of TEVs in the near wake for every half stroke of motion. That same double vortex structure was not observed for the sinusoidal and triangular pitching cases. Sinusoidal and triangular pitching showed similar vortex structures, although the triangular pitching generated weaker LEVs. Koochesfahani [50] performed dye visualization on the vortex structure of the wake of a NACA-0012 airfoil undergoing asymmetrical pitching motion. Flow conditions were set at $Re = 1.2 \times 10^4$, with varying parameters that include reduced frequencies between 0.83 and 10, pitching amplitudes of 2° and 4°, and zero mean angle of attack. The asymmetrical motions were governed by a symmetry parameter, S, that prescribes the varying pitch up and pitch down rates. Flow visualization analysis concluded that an enhancement in vortex shedding occurred at lower pitching rates and the largest pitching amplitude. Among the pitching motions, a single strong vortex was formed in the wake of the pitching airfoil during the rapid motion of the pitching cycle, whereas more than one vortex was observed during the slower motion of the pitching cycle.

Numerical work

Eldredge et al. [51] simulated a large amplitude canonical pitch maneuver with a single linear pitch up and pitch down motion to examine the role of the LEV in lift generation. The canonical motion performed pitch amplitudes of 25° and 45° at $Re = 1 \times 10^4$. During pitch

up motion, lift and drag monastically increased with increasing pitch rate. Higher pitching rates led to stronger LEVs, and exhibited distinct paired vortices in the wake. Although the lower pitch rates also generated large LEVs, they yielded relatively weaker vortices shed into the wake. During the pitch down motion, high pitch rates generated negative lift and positive thrust, whereas lower pitching rates sustained most of the positive lift and drag generated during the motion. Zaman et al. [52] investigated the impact of non-sinusoidal pitching using 2-D Navier-Stokes simulations on a NACA-0012 airfoil at $Re = 500$ and high reduced frequencies between 8 and 16. The non-sinusoidal pitching profile was a close resemblance of a trapezoidal waveform. An effective parameter that combines pitching amplitude and frequency was derived to characterize the flow as periodic or chaotic, where $\theta_o = 1.4k^{-1/4}$ and $\theta_o = 1.7k^{-1/4}$ represent the periodic and chaotic flow regimes, respectively. The authors reported a maximum increase in mean thrust coefficient of 55% at $k = 8$ and pitching amplitude of 30° for the non-sinusoidal pitching in the periodic regime. On the other hand, the sinusoidal pitching was found to be the favorable waveform in the chaotic flow regime and was able to sustain thrust development. Because the nature of the non-sinusoidal waveform allows for prolonged periods at maximum amplitudes during the motion cycle, high suction pressure on the backside of the airfoil has enough time to generate larger TEV, causing a drop in mean thrust.

Additionally, Xiao and Liao [53] carried numerical simulations using the unsteady Navier-Stokes simulations to assess the flow around non-sinusoidal pitching of a NACA-0012 airfoil at $Re = 1 \times 10^4$. The non-sinusoidal motion was controlled by an asymmetric parameter, s, to execute asymmetrical motions which vary from triangle to square waveforms. Pitching amplitudes of 2°, 4° and 6°, and reduced frequencies between 2 and 8 were considered. Their results showed that the non-sinusoidal pitching resulted in a stronger reverse Von-K*árm*án vortex street that is responsible for an increase in thrust production. The more asymmetric

the airfoil motion was (lower s values), the stronger the reverse Von-K*árm*á*n* vortices were. However, the increase in thrust was accompanied by an exponential increase in power input that resulted in lower propulsive efficiencies. Thrust generation was reported at $k = 5$ for lower pitching amplitudes. An increase in pitching amplitude resulted in sustaining that thrust production across all range of tested reduced frequencies.

K. Lu [54] performed a two-dimensional numerical simulation to examine the effects of non-sinusoidal large-amplitude pitching of a NACA-0012 airfoil on thrust forces. Flow conditions of $Re = 1.35 \times 10^5$, pitching amplitudes between 5° and 30°, and reduced frequencies between $k = 6$ and 18 were considered. The authors of this paper introduced an adjustable parameter K into an equation that describes the kinematics of the waveform, which can vary between sinusoidal, triangular, and trapezoidal pitching. For sinusoidal motions, large-amplitude pitching generated more thrust at higher reduced frequencies. Out of many tested K values, the authors concluded that a waveform resembling a square wave has the most influence in wake patterns and induced stronger reverse Von-K*árm*á*n* vortex street that led to lower momentum deficits (i.e., lower drag forces). However, they discovered that this choice of kinematics came with a penalty of lower propulsive efficiency. From an earlier study, K. Lu [55] revealed that larger values of parameter K (square wave) resulted in flow reattachment at higher AoA. Increasing parameter K also induced a noticeable increase in maximum lift and drag coefficients.

Yonghui Cao [56] ran two-dimensional numerical simulations using Navier-Stokes solvers to investigate the hydrodynamic performance of a flapping NACA-0012 hydrofoil. They considered the effects of symmetric pitching and non-symmetric pitching at $Re = 2.63 \times 10^4$, pitching amplitude of 30° and reduced frequencies between 1 and 6. For the case of asymmetric motion, the instantaneous thrust and lift generation improved, the average absolute value of the lift coefficient increased, but the overall propulsive efficiency decreased relative

to the symmetric case. Optimized thrust coefficient and propulsive efficiency were achieved when parameter $K = -0.97$, closer to a representation of a square wave input. At $k = 4$, the thrust coefficient increased by 25%, and the propulsive efficiency increased by 60% in comparison to pure sinusoidal pitching.

Finally, Bos et al. [57] modeled the lift and drag forces using two-dimensional time-dependent Navier–Stokes simulations, and introduced more complex kinematics into a pitching airfoil by incorporating a mix of trapezoidal and sawtooth amplitudes as a simple representation of the kinematics of a fruit-fly at $Re = 100$. They notably discovered that the introduction of a sawtooth-shaped amplitude resulted in a mean drag increase of 24.3% in cases where large accelerations of downstroke motion were performed.

Analytical work

Analytical work by Tahmasian et al. [58] optimized input amplitudes for mechanically controlled systems with high frequency, high amplitude inputs. They used geometric control and averaging theory on non-zero mean periodic functions to investigate the effects of nonlinearities produced by the input waveforms on amplitude and energy system requirements. As part of their optimization objectives, out of the square, sinusoidal and triangle waveforms, a square waveform required the least input amplitude to achieve system control. However, a sinusoidal input was found to be the optimal waveform to minimize energy input.

1.1.3 Applications in Low Reynolds Number

The intrinsic behavior of animal bio-locomotion inspires the design of vehicles such as small unmanned aerial vehicles (UAV), micro-air vehicles (MAV), and autonomous underwater vehicles (AUV). Animals and insects are small in size relative to large-scaled rotorcrafts and fixed wings, yet they can operate with enough agility to perform efficiently within their respective operational limits. The application of bio-inspired vehicle design in low Reynolds number gives rise to the importance of understanding the fluid-structure interaction that takes place during animal bio-locomotion. Figure 1.2 illustrates a range of applications operating at different Reynolds numbers. The range of applications spans across many orders of magnitude in the Reynolds number. Each flow regime has significant effects on forces generated and boundary layer events, and so, scaling conventional aircraft, and macroscopic animal locomotion becomes an area of focus in research.

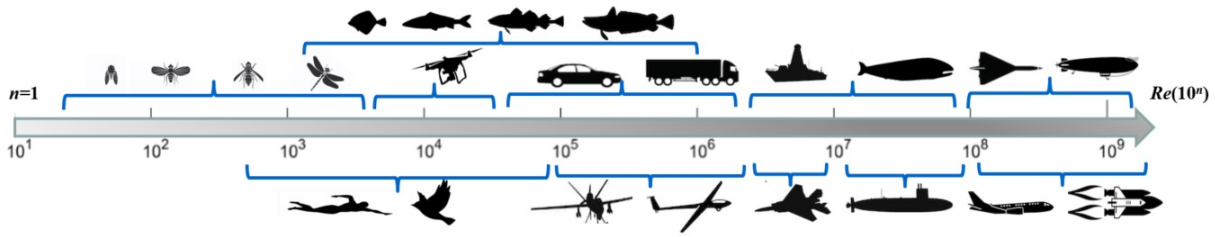

Figure 1.2: Overview of a range of applications to which Reynolds number varies across. (Note: Individual images are copyright free. Credit is extended to I.D. users of shutterstock/{AlexHliv, VectorPot, Mrs. Opossum, Black creator 24, vadimmus, Leremy, Barry Barnes})

1.1.4 Pisciform Locomotion

The ability of a fish to deform its body in order to propel itself with desired speed, agility, maneuverability, and stability motivates the analysis and design of biomimetic underwater

locomotion devices. There is a wide variety of pisciform (fish-like) morphologies and motion patterns ("gaits"), which are broadly classified according to how much of the body undulates to create propulsion. A boxfish, for example, uses "ostraciiform" locomotion in which the tail oscillates about a pivot point to generate propulsion. Jacks and mackerel are "carangiform" swimmers, undulating about one-third to one-half of their body length. Eels use "anguilliform" locomotion, in which nearly the entire body length undulates [59]. Figure 1.3 summarizes the motion seen by pisciform swimmers [60, 61, 62]. The shaded area represents the part of the body that undulates to generate in propulsion for ostraciiform, thunniform, carangiform, subcarangiform, and anguilliform swimmers.

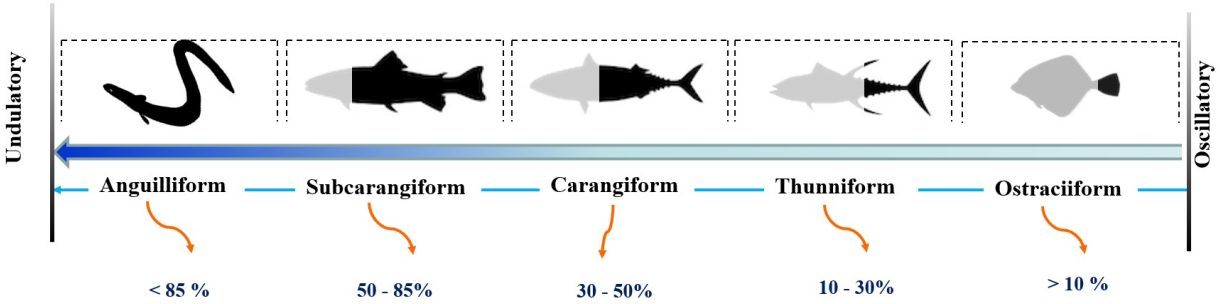

Figure 1.3: Kinematic distinction of pisciform swimmers is governed by how much part of their body undulates. (Note: Individual images are modified from copyright free images. Credit is extended to I.D. users of shutterstock/{Kuryanovich, Tatsiana, Koshevnyk}).

The notion of biomimetic autonomous underwater vehicles (AUVs) is not new, and researchers have proposed a variety of designs over the years, from the simpler carangiform concepts [63, 64, 65] to those that more closely resemble snakes or eels [66, 67, 68]. Modeling efforts generally rely on analytical or semi-empirical quasi-steady hydrodynamic approximations, even though these models are often inaccurate, particularly when considering the three-dimensional flow over a low aspect ratio device such as a robotic eel.

Like unsteady aerodynamic forces, the forces on an oscillating hydrofoil are transmitted by two primary mechanisms: added mass and circulatory effects. The force associated with

added mass is purely a potential flow effect, independent of viscosity, which is a consequence of the fluid being accelerated around the body as the body moves through it. The circulatory force is associated with the introduction of vorticity into the flow by the hydrofoil. For a fish swimming at a high reduced frequency (highly unsteady flow), added mass effects are the dominant mechanism for force transmission [60, 69].

Detailed analyses of the morphologies and gaits in pisciform swimming and the effects on the surrounding flow pattern have helped scientists better understand the locomotion of fish. Consider, for example, a simple articulating hydrofoil which generates a sequence of shed vortices whose rotational direction is reversed, relative to the familiar Von-K*árm*á*n* wake. This phenomenon results in the formation of the so-called "reverse Von-K*árm*á*n* street" [50]. The pattern formed by the vortices in the wake induces a jet-like push in the direction of the mean flow. Figure 1.4 compares the Von-K*árm*á*n* street in a cylinder's wake with the analogous "reverse Von-K*árm*á*n* street" as a result of different tail beat frequencies of a fish tail. At low non-dimensional reduced frequency, the wake of an oscillating fish tail produces the classic Von-K*árm*á*n* vortex street, similar to the top diagram of Figure 1.4. The wake induces the generation of time-varying mean drag force. On the other hand, at higher reduced frequencies, the wake generates a reverse Von-K*árm*á*n*. The street can consist of vortices in the upper row and lower row that rotate counterclockwise and clockwise, respectively. This mechanism induces a time-varying mean thrust force in this scenario. The propulsion force acting on the body is in reaction to this induced fluid momentum. The typical range of reduced frequencies in which significant thrust force begins to form at low oscillation amplitudes can be anywhere between $k = 0.8$ and 2 [50, 70, 71]. In addition, deflected jets caused by the single and double vortex structure are asymmetric in position and circulatory strength. As such, the jet will react at an angle relative to the freestream direction, resulting in a pressure differential in the flow field and asymmetry in the direction where the mean

velocity is acting.

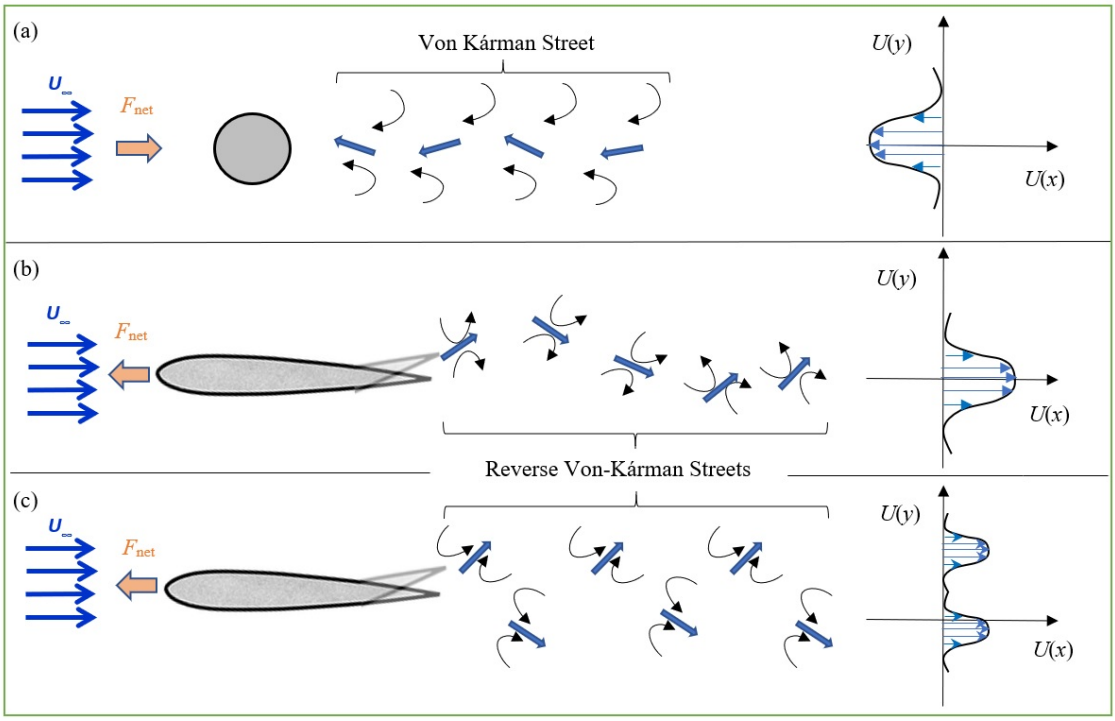

Figure 1.4: Schematic of the familiar Von-K*árm*án and reverse Von-K*árm*án streets in the wake of a cylinder and an oscillating fish tail. The velocity profile represents the resultant jet created by single and double structure vortex. A reactive force would generate an opposite and equal reaction. In the case of (a), a resultant drag force will produce. In the case of (b), a consequent thrust force will generate.

It has also been shown that vortical energy can be recaptured from an incoming flow to minimize energy use during propulsion [50]. The schematic diagram in Figure 1.5 shows that body vortices can shed and self-advect downstream to mix with trailing edge vortices that can potentially provide new fluid mechanisms for thrust enhancement by active or passive deformations. Fish collect vortical energy from upstream flow by curving their bodies and shed the vortex downstream by stretching their bodies to propel forward.

The modeling of pisciform locomotion is non-linear, underactuated, and time varying. These characteristics pose a challenge to implement traditional control methods. A geometric mechanic derivation of the equation of motion was examined by Kanso et al. [63] in which

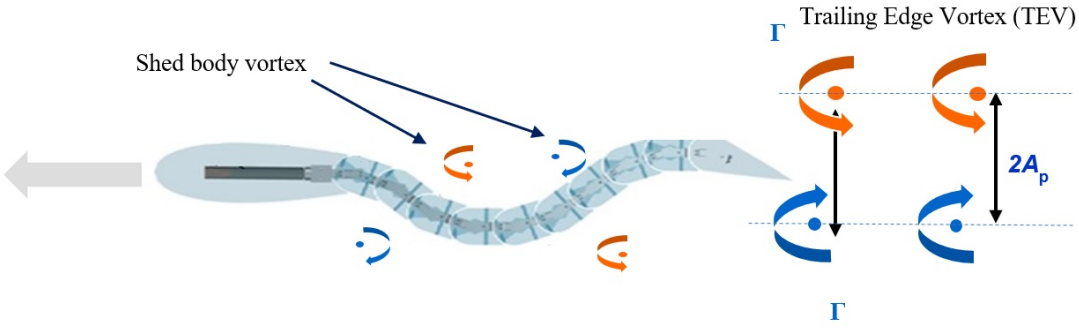

Figure 1.5: Body and trailing edge vortices around an articulating body.

they demonstrated the locomotion of articulated bodies in perfect fluids. Their work shows that articulated bodies in fluids can induce a motion that, in turn, is enough to generate propulsive forces. Bozkurttas et al. [72] showed that for a general fish specimen that operates at $Re = 2\times10^4$, laminar flow over a body most likely retains in a nominally attached flow, but a transition to turbulence downstream of the appendages is expected in regions where flow separation is present. Barrett et al. [73] examined the effects of low Reynolds number on drag reduction of a swimming fish and concluded that the tail beat of a fish controls the vorticity shedding. Their findings additionally showed that the Strouhal number must be within a range between St = 0.12 and 0.35 for the specimen to develop thrust. The body flexing in the form of a traveling wave also has the effect of laminarizing the boundary layer and indicating the importance of waveform kinematics to control the boundary layer and vorticity shedding to the benefit of thrust production. In the context of hydrodynamic assessment for eel-like motion, there have been many efforts to understand the evolution of body shed vortices generated by the carangiform and anguilliform kinematics to study the effects on forward and turning locomotion (Tytell and Lauder [74], Triantafyllou et al. [75]). Small alterations in the kinematics of a pisciform swimmer may cause substantial differences in propulsive performances (Drucker and Lauder [76]). This justifies the importance of supporting the continuous exploration of the effects of different modes of swimming on hydrodynamic force

generation. The continuous exploration of the hydrodynamic differences between different modes of swimming provides an important notice that small differences in kinematics may cause substantial changes in hydrodynamic effects . There have also been few attempts to determine the efficiency of carrangiform and anguilliform swimmers, with reported Froude efficiencies from literature ranging between 43% and 97% (Drucker and Lauder [76], Müller et al. [77], Schultz and Webb [78]).

Kelly et al. [79] developed a prototype that approximates a carangiform locomotion using three articulated modules representing the body, the peduncle and the caudal fin. This approximation was further extended by [65] where a quasi-steady fluid model was proposed with experimentally determined parameters from a three-link robot performing carangiform-like swimming. Optimal controllers were developed for the simplified propulsion model by [80]. Vela et al. [81, 82] employed geometric control theory and averaging of non-linear time periodic responses of a carangiform swimmer, and incorporated feedback to stabilize swimming trajectories. The geometric control model analyzed by Vela et al. [81] is provided by Bullo [83] who demonstrated that open-loop high-frequency forcing can lead to stabilizing the unstable equilibria. Finally, Morgansen et al. [64] performed an open loop control and a closed loop feedback stabilization for a free swimming carangiform robot but for a model with lower order fluid effects derived from quasi-steady assumptions only.

Role of Flexibility on Fluid Forces

Incorporating flexibility in swimming devices has been explored as a mechanism to improve aerodynamic and hydrodynamic performance [84, 85, 86, 87]. Extensive theoretical, numerical and experimental work on the flapping of rigid foils have shown optimum thrust over ranges of Strouhal numbers, a non-dimensional frequency, of $St = 0.25 - 0.4$ consistent with the range observed in nature [88, 89]. Further attention has been recently given to flexible

rectangular panels as propulsors where material stiffness, aspect ratio, and swimming speeds are the primary driving parameters for achieving higher propulsive efficiency [90]. Additionally, most literature shows that propulsive performance of heaving and pitching plates depends strongly on structural resonance. While most experimental studies [86, 91] report that actuation within 10% of the structure's resonant frequency achieved the highest Froude (propulsive) efficiencies, others have found the highest efficiencies within 30-50% of the resonant frequencies [92]. Incorporating flexibility into the pitching mechanism on wings of micro-air vehicles (MAVs) has also been shown to have a profound impact on propulsive efficiency, exhibiting a band of frequencies over which flexible panels produce more thrust than rigid panels [93]. These observations have led to the rise the role of flexibility in propulsive performances.

The coupling of biology-inspired aerodynamics with structural dynamics can lead to nonlinear effects. For example, wing/hydrofoil deformation has been proven to be beneficial for flight performance (Ifju et al. [94], Shyy et al. [95], Rojratsirikul et al. [96]), and swimming performance (Dewey et al. [85], Quinn et al. [86]). Physically, the membrane deformation results in a mean camber and large fluctuations that improve aerodynamic and hydrodynamic forces generated relative to a rigid airfoil/hydrofoil configuration. Force responses generated from flexible flapping of wings of birds or tails of fish lead to complex fluid structure interaction and can give rise to three-dimensional separation, transition in boundary layers, vortical patterns, and shear layer effects. Shyy et al. [84] established that local structural flexibility in a wing can delay stall and enhance aerodynamic performance in fixed wings. Ericsson and Reding [97] examined the combined roles of bending and pitching motions of a plate on flow dynamics at $Re = 10^4$. Results revealed that aerodynamic damping was a result of the bending motion whereas the time lag (unsteady effects) in flow response was a result of the pitching motion. Quinn et al. [86] determined experimentally that the optimum

propulsive efficiencies of heaving flexible panels under freestream flow conditions peaked at frequencies close to resonant frequencies and maximized trailing edge amplitudes. Enhanced propulsive efficiencies were also reported for more flexible tails at low swimming speeds for a chord-based Reynolds numbers ranging between 7.8×10^4 to 4.7×10^5.

1.2 Motivations and Contributions

It is essential to understand the fluid-structure interaction of flapping elements at low Reynolds number for design, control, and improvement of small biomimetic UAVs, MAVs, and AUVs. The objectives of all research efforts are complementary to each other with each section having its unique contribution to the overall research.

Objective 1

One can view lift enhancement in two ways. The first is the enhancement in the mean lift generated. This is useful to predict aerodynamic forces in the preliminary design process of flow control devices. The second is an enhancement in the lift amplitude. The determination of lift amplitude and local maxima in lift coefficients can be useful in assessing the dynamic stability and control authority of a flying vehicle. Although lift enhancement and its association with LEV shedding on oscillating airfoils is well understood, lift enhancement mechanisms on flapped airfoils is less well studied. In this investigation, we utilize forced oscillation of a trailing edge flap on a NACA-0012 airfoil at pre-stall and stall angles of attack to understand the flow physics through force measurements to explore potential lift enhancements on flapped airfoils. The first objective of this dissertation is twofold. First, we aim to assess the flowfield response of a NACA-0012 wing to a harmonically oscillating trailing edge flap (TEF) at a chord-based Reynolds number of $Re = 2.1 \times 10^4$. Static lift measurements for all airfoil and deflected flap positions were first obtained in a wind tunnel to establish a baseline case. In the dynamic cases, the leading element of the airfoil remained fixed while the TEF was allowed to pitch from the airfoil's three quarters chord length at five pitching reduced frequencies. TEF oscillations were examined at two flow states: mean AoA, $\alpha_0 = 0°$, corresponding to a nominally fully attached flow, and $\alpha_0 = 10°$, correspond-

ing to a nominally separated flow. In these comparisons, the TEF executed a sinusoidal pitching with equal amplitudes of $\delta_A = 5°, 8°$ and $10°$. The lift responses are compared and validated with a constructed semi-empirical/quasi-steady formulation of Leishman's model for unsteady flapped airfoil (Leishman [8]). The second objective is to construct a frequency response (gain and phase as a function of reduced frequency) for all cases considered. The approach used here was previously employed by Zakaria et al. [13] with force measurements on a plunging NACA-0012 airfoil at $Re = 9 \times 10^4$ and by Rezaei and Taha [98] with computational analysis on a pitching NACA-0012 airfoil at $Re = 7 \times 10^4$. Beyond the two objectives described above, we also examine the relationship between TEF oscillation and hysteresis in the corresponding aerodynamic forces and moments.

Objective 2

Previous studies by Ol et al. [49] and Eldredge et al. [51] through (PIV) and computations justified how wing kinematics can result in unique vortex shedding events that can lead to potentially new and different force generation mechanisms. The trends in force generation are connected to the LEV and TEV phenomena during these shedding events. The work here references PIV results reported by Ol et al. [49] through direct force measurements of lift and drag forces in a wind tunnel of a NACA-0012 airfoil undergoing different pitching waveforms at 2.1×10^4 Reynolds number. The second objective of this study is to report wind tunnel measurements of the forces produced by a NACA-0012 airfoil undergoing sinusoidal, trapezoidal, sawtooth and reverse sawtooth waveforms. We will examine flow quantities such as mean lift, lift amplitude, and the lift-to-drag ratio at mean angles of attack that will nominally represent pre-stall, near stall, and post-stall flow states. We also report any generated lift enhancements and flow non-linearities. Finally, we compare the measured unsteady lift against a quasi-steady and an unsteady state-space model developed by Taha et al. [5].

Objective 3

Current research and design of fish-like locomotion devices primarily focuses on demonstration of "proof of concept," and acquires hydrodynamic principles to inform the design of efficient biomimetic propulsion and control systems. High-performance underwater vehicles that address the disciplines illustrated in Figure 1.6 brings us a step closer to targeting challenges in the design and control of autonomous vehicle design.

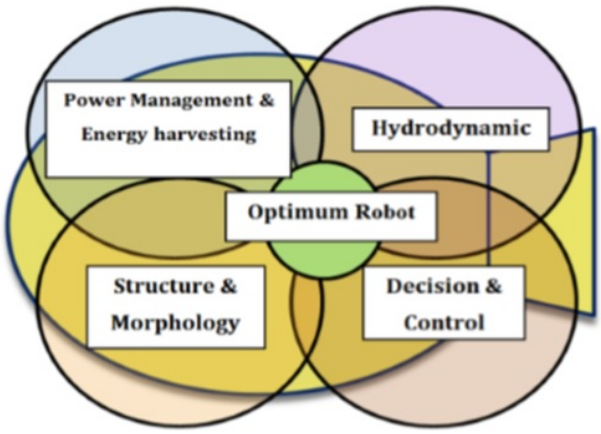

Figure 1.6: Optimum performance for an autonomous underwater vehicle

Incorporating flexibility on hydrofoils can have a profound impact on the hydrodynamic characteristics of a flapping fish-tail. The coupling effects of geometric and hydrodynamic non-linearities on the structure can be responsible for the enhancement of thrust performance on a swimming device. Detailed investigations of the effects of flexibility and the role of structural resonance in enhancing thrust performance are critical for the success of current autonomous undersea vehicles. The third objective of the study is to provide detailed measurements of the thrust forces and servo torques and to determine the effect of fish-tail flexibility on propulsive performance. The experiments were conducted with and without forward towing speed to compare the hydrodynamic performance between the two scenarios. The maximum trailing edge amplitudes were observed using video imagery and a position

tracker Matlab script at specific frequencies to examine briefly the effects of resonant frequencies of the first bending mode on the localized thrust production and propulsive efficiency peaks. This work also aims to provide data that can be used to validate computational tools. Finally, this work will use the instrumentation and design concepts to guide the design and building of the Modular Biolocomotion Emulator (MBE).

Objective 4

Although lower fidelity dynamics models have shown promise in simulating simple system motions for pisciform swimmers, they generally cannot be accurately useful for the full exploration of system capabilities. Accurate parameterized models and high fidelity simulations to examine hydrodynamic performances on pisciform swimmers are complicated and computationally expensive. Several efforts have been attempted experimentally to assess full hydrodynamic effects on swimmers, but the gap of readily available experimental hydrodynamic data for a variety of kinematics and locomotion types remains. Prior work has focused primarily on demonstrating prototypes in free-swimming operation. The fourth objective of this study is to obtain and archive hydrodynamic force and moment data that can be used to validate reduced-order computational methods such as the unsteady vortex lattice method (UVLM). The experimental program focuses on a particular biomimetic device, the modular biolocomotion emulator (MBE), which is forced to oscillate periodically while being towed along a straight line in calm water. This study captures unsteady hydrodynamic forces and moments generated for a test series in which the MBE was towed at different towing speeds (in addition to zero speed) while executing four distinct gaits at a variety of frequencies. The MBE geometry and kinematics are varied further to test a broad range of morphologies and gaits. The MBE also performs artificial modes of bending through active actuation on each module to further support the understanding of flexibility effects.

Chapter 2

A Frequency Response Approach to Measure Lift Enhancement on a Flapped Airfoil at Low Reynolds Number

The contents of this chapter are based on the preliminary results of the following conference paper: *Shehata, Hisham, Mohamed Zakaria, Ahmed Hussein, and Muhammad R. Hajj. "Aerodynamic analysis of flapped airfoil at high angles of attack." In 2018 AIAA Aerospace Sciences Meeting, p. 0037. 2018. [99].*

The objective of this study is twofold. First, we aim to assess the flowfield response of a NACA-0012 wing to a harmonically oscillating TEF at a chord-based Reynolds number of $Re = 2.1 \times 10^4$. Static lift measurements for all airfoil and deflected flap positions were first obtained in a wind tunnel to establish a baseline case. In the dynamic cases, the leading element of the airfoil remained fixed while the TEF located at 75 % chord length from the airfoil's leading edge pitches about the airfoil's mean angle of attack (AoA). TEF oscillations were examined at two flow states: mean AoA, $\alpha_0 = 0°$, corresponding to a nominally fully attached flow, and $\alpha_0 = 10°$, corresponding to a nominally separated flow. In these comparisons, the TEF executed sinusoidal pitching amplitudes of $\delta_A = 5°, 8°$

and 10°, and at five reduced frequencies between k=0.02 and 0.12. The lift responses are compared with a constructed semi-empirical/quasi-steady formulation of Leishman's model for unsteady flapped airfoil (Leishman [8]). The second objective is to construct a frequency response (gain and phase as a function of reduced frequency) for all cases considered. The approach used here was previously employed by Zakaria et al. [13] with force measurements on a plunging NACA-0012 airfoil at $Re = 9 \times 10^4$ and by Rezaei and Taha [98] with computational analysis on a pitching NACA-0012 airfoil at $Re = 7 \times 10^4$. Beyond the two objectives described above, we also examine the relationship between the oscillating TEF and hysteresis in the corresponding aerodynamic forces.

2.1 Experimental Setup

2.1.1 Test Facility and Test Article

The experiments were performed in a suction-type open circuit subsonic wind tunnel at Virginia Tech. The tunnel has a centrifugal fan powered by a 15 HP Leeson motor that drives the airflow past a square honeycomb inlet. The inlet is followed by three turbulence reduction screens to ensure uniform flow with a turbulence intensity of roughly 0.2% at 10 m/s. The test section has dimensions of 120 cm × 52 cm × 52 cm. Figures 2.1 and 2.2 show a photo and a schematic diagram of the test facility and setup used for the experiments. The wing model used is a NACA-0012 airfoil profile fabricated from a foam core and reinforced with carbon fiber casing. The wing's chord length is $c = 7$ cm, and the 51 cm span extends across the width of the wind tunnel test section with 0.5 cm of clearance from the wall on either side. The airfoil has a flap hinged at 75% chord length from the airfoil's leading edge. An aluminum sting is fixed to the airfoil's quarter chord from one end and attached to the

load cell on the other end by a circular bracket. A fairing holding the digital servo is fixed on the lower half of the sting to provide smoother streamlines. Figure 2.3 shows a closeup schematic of the wing actuation mechanism.

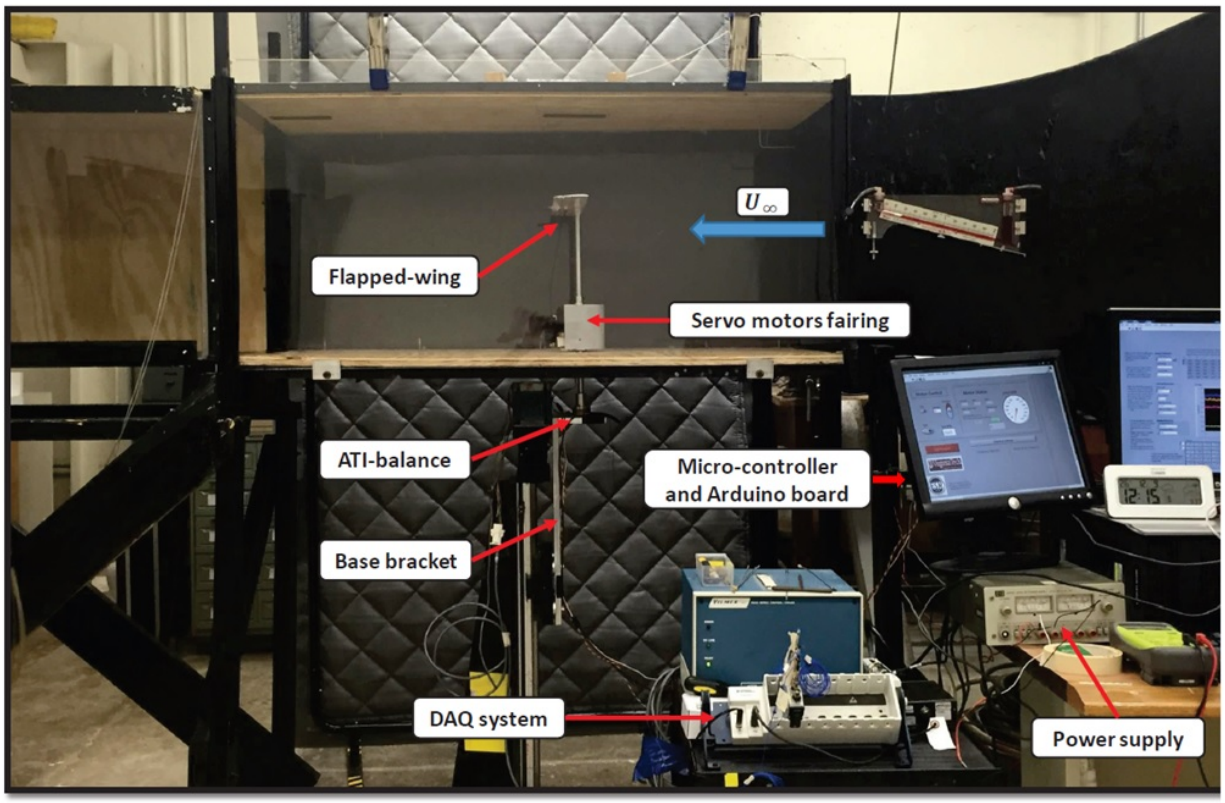

Figure 2.1: Wind-tunnel set up at Virginia Tech

2.1.2 Data Acquisition System

Direct force measurements were acquired using an ATI Industrial Automation six-axis Mini40 force/torque sensor, capable of measuring forces up to ±80 N in the x-direction and ±240 N in the y and z directions, and torques up to ±4 N.m for all three axes. The resolution for force measurements is 0.02 N for F_x and F_y, and 0.04 N for F_z. Data were collected and processed using National Instruments' NIdaq-9172 and NIdaq USB-6210 with a sampling frequency of

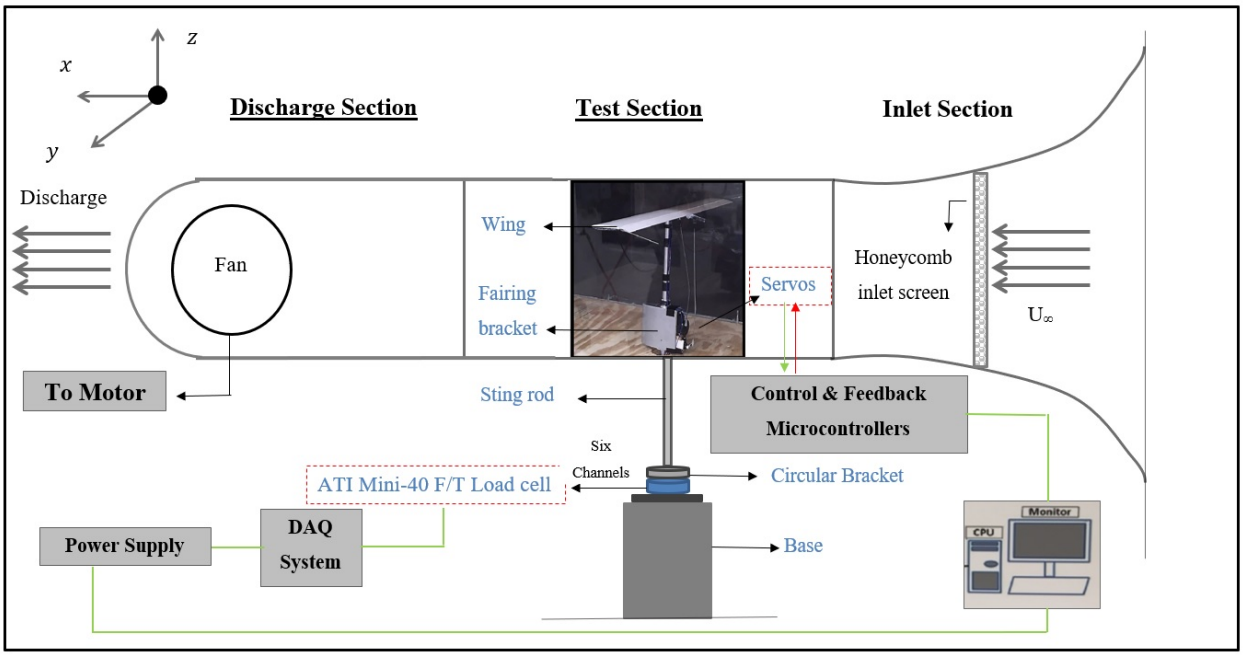

Figure 2.2: Schematic for the tested mechanism fixed inside the tunnel

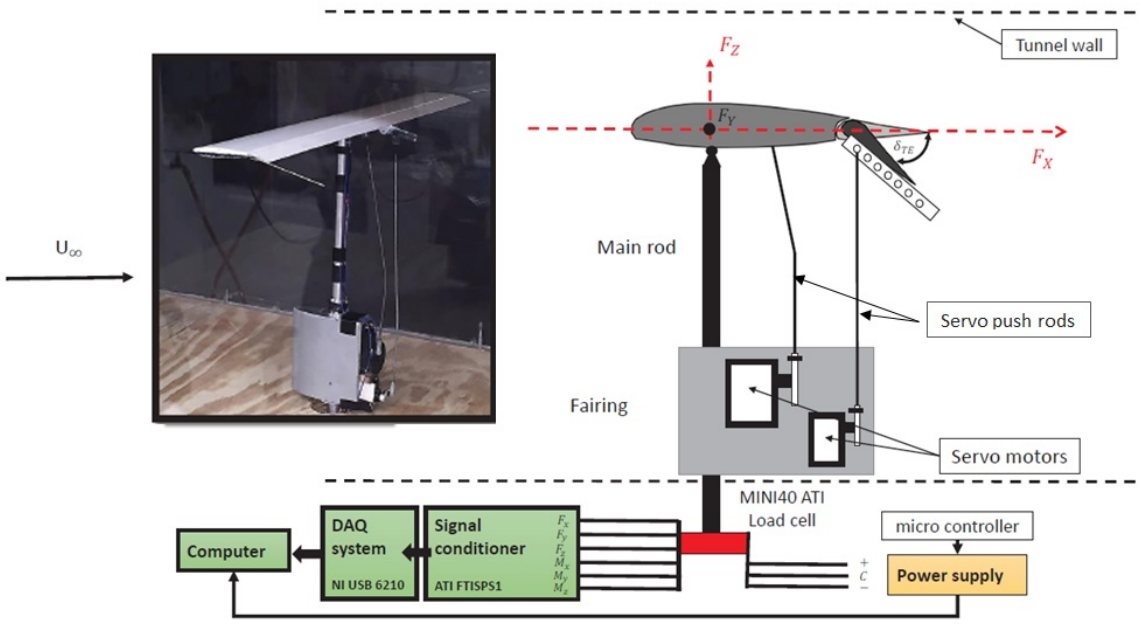

Figure 2.3: Schematic of the tested mechanism

1,000 Hz. The wind tunnel was allowed to run for at least 30 seconds prior to data collection to ensure a fully developed flow. Additionally, the first five seconds of the time series were omitted from the measured data to avoid any transient inertial effects sourcing from the test rig. The measured data were smoothed using a digital fourth-order Butterworth low pass filter with cut-off frequency of at least twice the driving frequency. The oscillatory motion of the TEF is provided by a continuous FS90R micro-servo with maximum torque of 1.5 kg-cm at 6 V. The servo motor is connected to the TEF's surface by a steel push rod and controlled using a Pololu Maestro 6-Channel USB servo micro-controller. The leading element of the airfoil is also supported and held in place by another steel push rod. Finally, the TEF angular positions were measured by acquiring the analog voltage from the servo's potentiometer using an Arduino-Uno R3 sampled at 100 Hz. A calibrated curve fit was used to determine the relationship between the analog voltage output and the TEF angle. We performed a free vibration test (strike test) to make certain that the operational frequency is far from the test article's natural frequency. The fast Fourier transform determined that the first natural frequency of the test rig is approximately 17 Hz, which is at least six times the maximum excitation frequency operated during the experiments.

2.1.3 Uncertainty Analysis

The overall error in force coefficient measurements is found to be 3% accounting for errors in flow speed, angle of attack, bias error introduced during calibration, and sampling precision. Wind tunnel boundary corrections are calculated using the the method used by Pope and Harper [100]. Calculations of the solid two-dimensional blockage factor, wake blockage, and correction for streamline curvature demonstrated an uncertainty in lift coefficient measurements of ± 0.012. The airfoil's AoA was measured using an analogue protractor with an uncertainty error of $\pm 0.5^{\circ}$ degrees. Time delays provided by the Maestro micro-controller's

input clock resulted in an uncertainty in frequency inputs of ±0.01 Hz. The frequency input of the TEF is verified by performing a fast Fourier transform (FFT) on the potentiometer's output data. The uncertainty from the pitot tube used to measure the flow velocity is ±0.01 m/s resulting in a maximum total uncertainty in reduced frequency of $\Delta k \approx \pm 0.01$. The method suggested by Coleman and Steele [101] is used to estimate the uncertainty in the calibrated instrumentation system for potentiometer feedback. The maximum uncertainty in the Analogue-Digital converter (ADC) provided by the Micro-controller's board is ±0.25%, or approximately ±0.01 V relative to the Arduino's reference voltage. With a flap angle measurement uncertainty of ±0.5 degrees, the uncertainty in the calibration curve fit at 95% confidence from the potentiometer feedback for TEF positions is $\delta_{\mathrm{TE}} \approx \pm 0.2°$.

2.1.4 Experimental Test Matrix

Static lift and drag measurements were obtained for the airfoil with and without flap deflections for various mean AoA's at $Re = 2.1 \times 10^4$. Table 2.1 summarizes the range of parameters used for static lift and drag measurements. Lift forces were also measured for a dynamic TEF pitching at amplitudes of $\delta_{\mathrm{A}} = 5°$, 8°, and 10°, and about the leading element at two angles of attack. Pitching rates were varied over a range of operating frequencies from 0.5 Hz to 2.5 Hz which correspond to reduced frequencies from k= 0.02 to 0.12. Operating conditions for the dynamic test cases are summarized in Table 2.2. A schematic diagram in Figure 2.4 demonstrates the airfoil's dynamic operation at $\alpha_0 = 0°$ and $\alpha_0 = 10°$. Flapped angles are positive when deflected downwards.

Table 2.1: Tested parameters for static lift measurements

Parameter	**Range**
Reynolds Number, Re	2.1×10^4
Mean angle of attack, α_0 (deg)	0° to 28°
Flap deflection, δ_{TE} (deg)	+5°, +8°, +10°, +15°

Table 2.2: Operating conditions for dynamic lift measurements

Mean Angle of Attack, α_0 (Deg)	**TEF pitching amplitude, δ_A (Deg)**	**Reduced** frequency, k
0°, 10°, with fixed leading element	5°, 8°, 10°	0.02 - 0.12

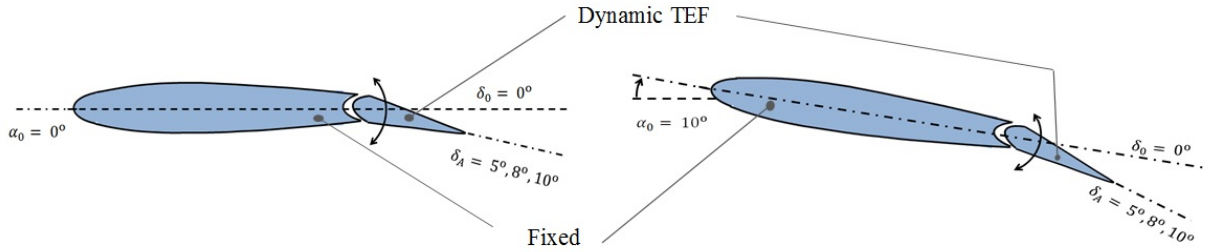

Figure 2.4: NACA-0012 dynamic operating configurations - Left : $\alpha_0 = 0°$, Right : $\alpha_0 = 10°$

A sinusoidal pitching waveform $\delta = \delta_A \sin(\omega t)$ was used as the TEF's motion input. Here, the TEF's mean incidence is relative to the airfoil's leading edge and was set to zero for all cases, δ_A is the TEF's pitching amplitude oscillating equally about δ_0, and $\omega = 2\pi f$ where f the forcing frequency.

The resultant AoA of the airfoil with a TEF deflection relative to the free stream velocity can be approximated in terms of effective angle of attack, α_{eff} and can be computed geometrically by measuring the angle of a line joining the leading edge of the airfoil and the trailing edge of the flap with respect to the freestream flow. The effective AoA for positive flap deflections $\delta_{\text{TE}} = +5°$, $+8°$ and $+10°$ with leading edge element fixed at $\alpha_0 = 0°$ are approximately $\alpha_{\text{eff}} = 1.5°$, $2°$ and $2.5°$, respectively. Similarly, the effective AoA for positive flap deflections of $\delta_{\text{TE}} = +5°$, $+8°$ and $+10°$ with leading edge element fixed at $\alpha_0 = 10°$ are approximately $11.5°$, $12°$ and $13°$, respectively. Both the airfoil's camber and effective angle of attack increase as a result of the flap deflecting downwards. An increase in camber for a static airfoil will generally produce additional lift.

2.2 Results and Discussion

2.2.1 Static Lift Measurements

In this section, we present direct force measurements on a static NACA-0012 with and without flap deflections. Measurements for all static cases were repeated three times, and the results were averaged. Figure 2.5(a) shows the measured static lift curve slope with $\delta_{\mathrm{TE}} = 0$ along with the lift curve slopes published by Laitone [102] and Alam et al. [103]. The static lift curves are in relative agreement, showing lower maximum lift coefficients and lower stall angles of attack for low Reynolds number flow than the theoretical $C_{\mathrm{l}} = 2\pi\alpha$ represented by potential flow theory. Figure 2.5(b) shows the airfoil's corresponding static drag coefficient at $\delta_{\mathrm{TE}} = 0°$. The experimental drag coefficient of the current airfoil is compared with experimentally obtained drag coefficients from Martínez-Aranda et al. [104], Ngo and Barlow [105], and Zakaria et al. [13] for a NACA-0012 with aspect ratios 2, 4, and 7, respectively. Although the wing for the current experiment is assumed to be nominally two-dimensional, the wing may still generate wingtip vortices that would result in an offset drag at zero AoA. The static drag coefficient is in agreement with data from the literature, particularly with results from Zakaria et al. [13] for a wing that is nominally two-dimensional with the same aspect ratio. Results from Martínez-Aranda et al. [104] depict a higher drag coefficient since they performed their experiments for a low aspect ratio and finite (three-dimensional) wing. Figure 2.5(c) shows the measured lift coefficient for various positive static flap deflections, δ_{TE}. The airfoil with $\delta_{\mathrm{TE}} = 0$ stalls around 10° AoA and stalls at lower AoAs with increasing positive flap deflections. Positive flap deflections on the airfoil produce a higher maximum C_L than the clean airfoil configuration. Figure 2.5(d) shows the measured static lift coefficient for selected positive flap deflections δ_{TE}, with the leading element fixed at 0° and 10°. These results show that the static lift continues to rise with increasing flap

downward deflection for a constant mean AoA and is indicative of flow remaining attached over the flapped part of the airfoil. A relevant point of reference would be results from Gildersleeve et al. [106] who showed that the flow over a flap hinged at 67% chord length of a NACA-0012 at $Re = 7.2 \times 10^5$ and zero mean AoA separates at a flap deflection angle of $+40°$.

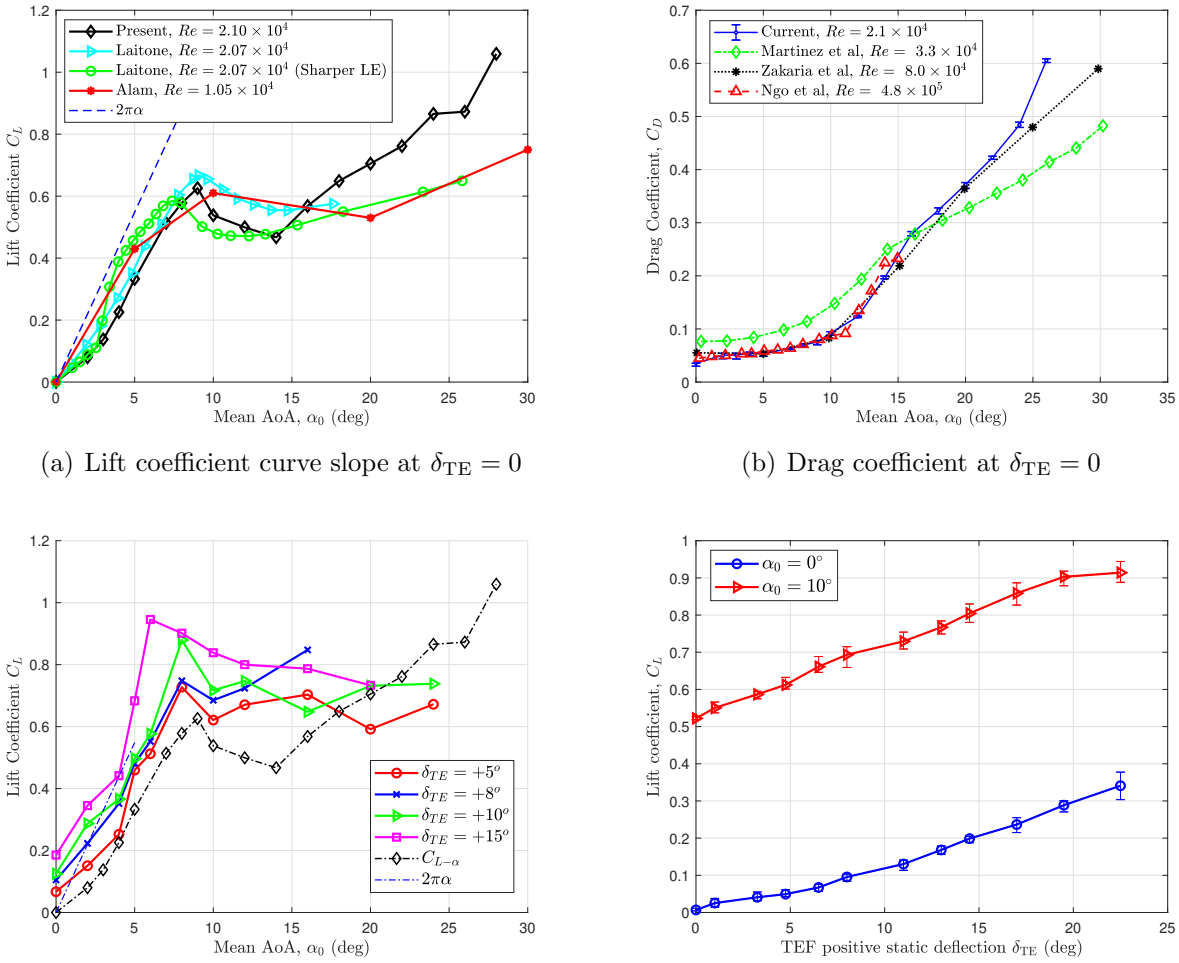

(a) Lift coefficient curve slope at $\delta_{\text{TE}} = 0$

(b) Drag coefficient at $\delta_{\text{TE}} = 0$

(c) Static lift curves for static flap deflections

(d) Static lift coefficient δ_{TE} at $\alpha_0 = 0°$, $10°$

Figure 2.5: Static lift measurements for plain and flapped NACA-0012 airfoil.

The static measurements obtained in Figure 2.5 provide a baseline for comparing experimental results involving oscillatory TEF motion. Additionally, the static measurements

obtained will enable us to tailor an existing quasi-steady aerodynamic model (Leishman's model [8]) using determined flow parameters such as the static mean lift and static lift curve slopes. This technique allows us to match initial quasi-steady conditions that would otherwise not be captured by Leishman's model, which bases assumptions on potential flow theory. Leishman [8] extended Theodorsen's [3] solution to predict the unsteady lift on an airfoil undergoing TEF arbitrary motion. With the addition of a TEF pivoting at a distance from the mid-chord, there are additional air loads that depend on TEF pitching δ and its time rate-of-change $\dot{\delta}$. In the absence of plunging motion, the formulation for the total lift is:

$$C_L = \frac{\pi b}{U_\infty^2}\big(U_\infty \dot{\alpha} - ba\ddot{\alpha}\big) + \frac{b}{U_\infty^2}\big(-U_\infty F_4 \dot{\delta} - bF_1 \ddot{\delta}\big) + 2\pi C(k)\big(\alpha_{\text{qs}} + \delta_{\text{qs}}\big) \tag{2.1}$$

where α is the time dependent pitching angle, U_∞ is the freestream velocity, b is the semi chord length, a is the airfoil's pitching axis measured in chord lengths aft of the leading edge, and $C(k)$ is Theodorsen's transfer function (also known as the lift deficiency factor), $2\pi\alpha_{\text{qs}}$ and $2\pi\delta_{\text{qs}}$ are the theoretical quasi-steady lift coefficients for the airfoil and TEF, respectively, and F_1 and F_4 are geometric terms that depend on the size of the TEF relative to the airfoil's chord length. The reader is referred to Leishman [8] for detailed derivation and notations.

Since the TEF motion is sinusoidal (i.e., linear and time invariant in practice), tailoring Leishman's formulation with experimentally determined quasi-steady parameters can be applied within the frequency domain. Instead of the 2π in the geometric term $2\pi\big(\alpha_{\text{qs}} + \delta_{\text{qs}}\big)$ of Eq. (2.1), the modified Leishman's formula will adopt the lift curve slope relationships obtained from Figure 2.5(c). For the clean wing, the lift curve slope (C_L/α) yields 5.34 per radian of angle of attack, where for the TEF cases, the lift curve slopes are (C_L/α) 5.41 for

$\delta_{TE} = 5°$, 5.45 for $\delta_{TE} = 8°$ and 5.57 for $\delta_{TE} = 10°$.

2.2.2 Dynamic Measurements

The measured unsteady lift responses generated by the dynamic TEF are presented and validated with the responses predicted by Leishman's analytical and quasi-steady formulations. The results are reproduced from Shehata et al. [99] with the additional incorporation of quasi-steady conditions such as the static mean lift and the lift curve slope characteristics into Leishman's analytical formulation. Figures 2.6(a), 2.6(b), and 2.6(c) show the C_L time histories at steady state for a 5° TEF pitching amplitude at $\alpha_0 = 0°$ and reduced frequencies of $k = 0.02,\ 0.07,\ 0.12$. A solid blue line represents experimental data in Figure 2.6. A dotted black line and a dashed red line represent the results for analytical and quasi-steady models, respectively. The static C_L results for the airfoil with maximum constant flap deflection of δ_{TE} (represented by the horizontal green line) are also directly compared with the dynamic results. Additionally, the static C_L value for the airfoil without flap deflection is represented by the horizontal light blue line. The experimental lift time histories show relatively good agreement with both analytical and quasi-steady models at $k = 0.02$ with the exception for $\delta_A = 10°$, and at $k = 0.07$ for $\delta_A = 5°$. Beyond these test cases, dynamic lift predictions made by the analytical model deviate away from the experimental results. In contrast, the responses from the quasi-steady model continue to predict the lift amplitudes accurately. Neither the quasi-steady nor the analytical models respond well beyond $k = 0.07$ and $k = 0.12$ for $\delta_A = 8°$ and $\delta_A = 10°$ indicating that the oscillatory conditions are generating highly unsteady flow around the airfoil. The combined effects of pitching amplitude and reduced frequency governs whether a flow is quasi-steady or unsteady. While examining the peaks of the lift responses at lower TEF pitching amplitudes, the measured C_L peaks (of the solid blue curves) in Figures 2.6(a) to 2.6(e) are closer to their respective static lift at

a maximum constant flap deflection (horizontal green line). This observation helps identify that the flow at these oscillatory conditions is close to a quasi-steady flow. The measured C_L peaks in Figures 2.6(f) to 2.6(i) demonstrate larger lift deficiency from their respective static C_{L} values (with a constant flap deflection) with increasing pitching amplitude and reduced frequency. This behavior is typical for oscillating airfoils and a reflection of Kelvin's circulation theorem (Rayleigh [107]): a rise in lift circulation around the airfoil will result in a drop in the lift circulation within the wake. The effects of the wake due to vortex shedding play a strong role in lift deficiency at higher reduced frequencies, a flow characteristic that is approximated analytically using Theodersen's lift deficiency factor $C(k)$ for potential flow. For all pitching amplitudes at $k = 0.12$, the lift responses are no longer sinusoidal as the flow response exhibits stronger non-linear fluctuations. Overall, isolating the effects of reduced frequency and pitching amplitude, the quasi-steady model provides a reasonable prediction of the unsteady lift up to $k = 0.12$. Large pitching amplitudes also limit the validity of the quasi-steady model even at lower reduced frequencies. The threshold to which the quasi-steady model can be used accurately also depends on the combined effects of pitching amplitudes and reduced frequency.

Figure 2.7 shows the C_L time histories for all TEF pitching amplitudes at mean AoA of 10°. There are two main observations here. First, there is an upward shift in the mean C_L measurement at higher reduced frequencies and pitching amplitudes. Second, the instantaneous peak lift continues to rise with increasing reduced frequency showing no sudden local drop in C_L that would indicate flow separation. For all cases, as the TEF motion sweeps through a range of pitching amplitudes, the airfoil's time-varying camber generates a varying effective angle about the mean AoA that ranges from 8.5° to 11.5° for $\delta_{\mathrm{A}} = 5°$ at $\alpha_0 = 10°$. Thus, the TEF motion is equivalent to oscillating the airfoil AoA between pre and post stall AoA values. Likewise, the varying effective AoA for $\delta_{\mathrm{A}} = 8°$ and $\delta_{\mathrm{A}} = 10°$ are $\alpha_{\mathrm{eff}} \in [8°, 12°]$ and

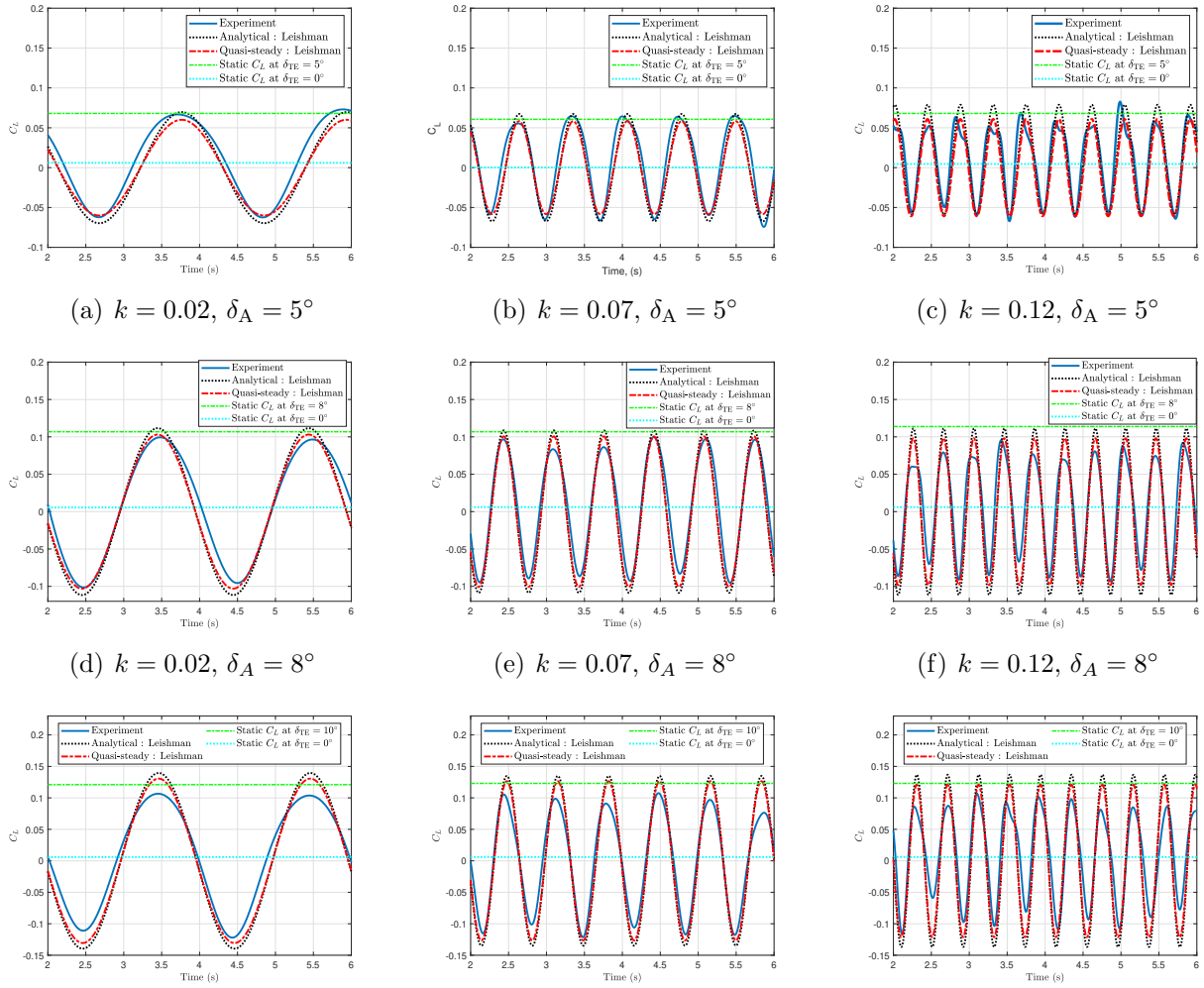

(a) $k = 0.02$, $\delta_A = 5°$ (b) $k = 0.07$, $\delta_A = 5°$ (c) $k = 0.12$, $\delta_A = 5°$

(d) $k = 0.02$, $\delta_A = 8°$ (e) $k = 0.07$, $\delta_A = 8°$ (f) $k = 0.12$, $\delta_A = 8°$

(g) $k = 0.02$, $\delta_A = 10°$ (h) $k = 0.07$, $\delta_A = 10°$ (i) $k = 0.12$, $\delta_A = 10°$

Figure 2.6: Lift coefficient histories at $\alpha_0 = 0°$. The green line is the static lift measured at a constant flap deflection of $\delta_{\text{TE}} = 5°$, $8°$, $10°$

$\alpha_{\text{eff}} \in [7°, 13°]$, respectively. Referring to Figures 2.7(b) and 2.7(c), the C_L time histories show a monotonic increase in lift amplitudes during every flap's upstroke motion. Similar lift response is pronounced at higher reduced frequencies and larger pitching amplitudes for the C_L time histories in Figures 2.7(e), 2.7(f), 2.7(h) and 2.7(i). A boost in lift amplitude is caused by the TEF's downstroke motion, and a net positive lift indicates the presence of a lift enhancement mechanism. This type of lift response can be associated with the presence

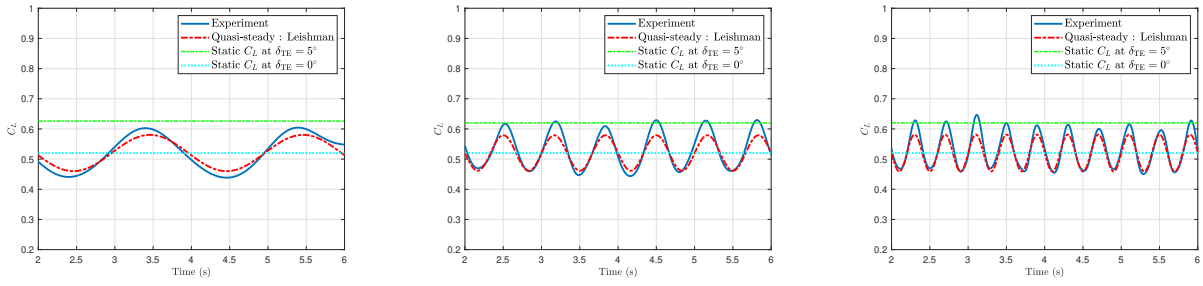

(a) $k = 0.02$, $\delta_A = 5°$ (b) $k = 0.07$, $\delta_A = 5°$ (c) $k = 0.12$, $\delta_A = 5°$

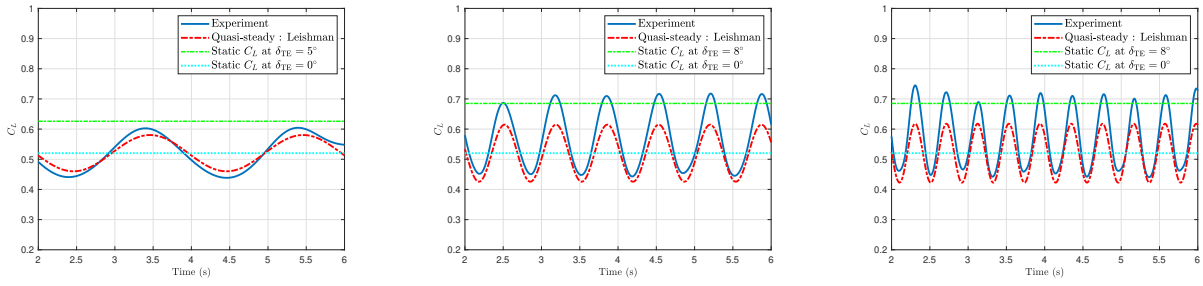

(d) $k = 0.02$, $\delta_A = 8°$ (e) $k = 0.07$, $\delta_A = 8°$ (f) $k = 0.12$, $\delta_A = 8°$

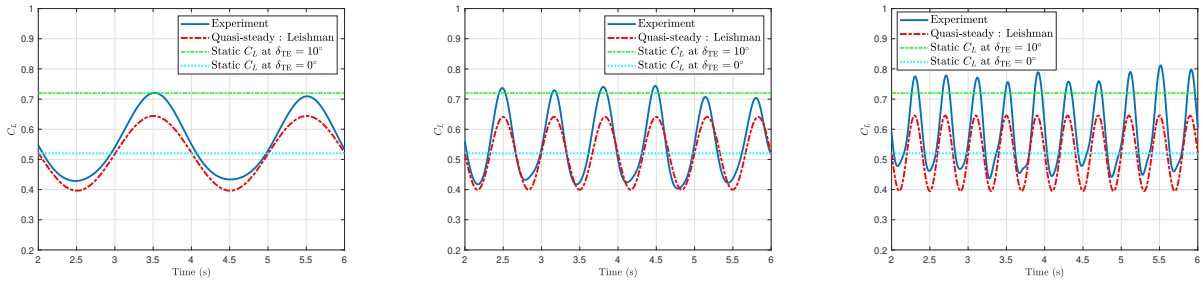

(g) $k = 0.02$, $\delta_A = 10°$ (h) $k = 0.07$, $\delta_A = 10°$ (i) $k = 0.12$, $\delta_A = 10°$

Figure 2.7: Lift coefficient histories at $\alpha_0 = 10°$. The green line is the static lift measured at a constant flap deflection of $\delta_{TE} = 5°$, 8°, 10°

of strong vorticity and large pressure differentials encountered in the flow that can generate additional circulation, thus lift force. Fluorescent dye visualization results from Medina and Rockwood [48] support the claim that resultant vortex elements within the separation envelope can be formed. TEF pitching of 1° amplitude at mean AoA of 10° is sufficient to induce flow reattachment or roll-up of the separated shear layer into a LEV. The system of vortices formed in these cases may be responsible for the attenuated lift amplitude at

these conditions. The behavior of the flow around these vortices can result in incremental lifts as a result of non-linear effects. Finally, predictions made by the quasi-steady model disagree with the unsteady responses generated at these flow conditions. This disparity is expected since the quasi-steady model is not tailored to capture changes in lift amplitude and dynamic mean lift. Predictions by the quasi-steady model are in relative agreement with experimental data only for low amplitude and low reduced frequency (Figure 2.7(a)). Table 2.3 outlines the percentage difference between the *RMS* lift amplitude of the predictions made by Leishman's model and the experimental data. A positive sign means that the *RMS* lift amplitude is greater for the experimental results. The model is limited to capture lift contributions from additional flow mechanisms such as LEV formation, LEV suction, and dynamic stall that may occur at higher TEF pitching amplitudes. Although it may not be clear what could be the primary driving mechanism that produces larger than normal instantaneous peak lifts at these conditions, the time series still provides some insight on a possible lift enhancement generated by the TEF's upstroke motion. Lift enhancement can be generally associated with increased vortical flow patterns, enhanced circulation, and the formation of large pressure differentials on the suction side of the airfoil [29, 48, 108].

Reduced frequency, k	$\alpha_0 = 0°$			$\alpha_0 = 10°$		
	$\delta_A = 5°$	$\delta_A = 8°$	$\delta_A = 10°$	$\delta_A = 5°$	$\delta_A = 8°$	$\delta_A = 10°$
0.02	+6.9%	-4.1%	-11.8%	+7.0%	+6.7%	+6.8%
0.07	+3.0%	-6.0%	-16.5%	+2.3%	+9.6%	+9.1%
0.12	-2.3%	-8.5%	-22.5%	+3.4%	+10.4%%	+15.3%

Table 2.3: Percentage difference in *RMS* amplitude between experimental data and lift predictions from Leishman's model.

Figure 2.8 shows a sample of the measured lift coefficient for a static airfoil with zero flap deflection in freestream flow at $\alpha_0 = 10°$ directly followed by an executed TEF pitching motion at $\delta_A = 8°$ at $k = 0.07$ for the remainder of the time. The data shows an 8%

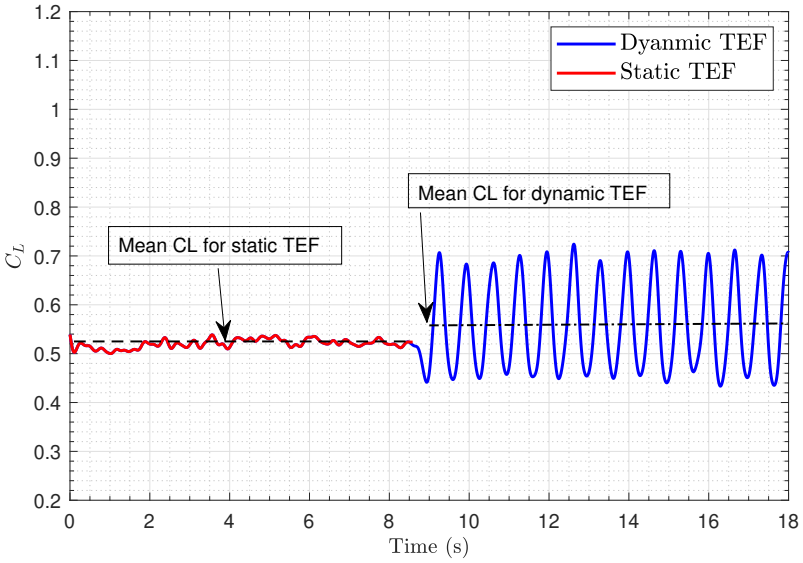

Figure 2.8: A shift in mean C_L is observed between the static airfoil and an airfoil with a dynamic TEF. Case: $\alpha_0 = 10°$, $\delta_A = 8°$ at $k = 0.07$

increase in mean C_L as a result of the dynamic TEF relative to the static airfoil with no flap deflection. Similarly, an increase in mean C_L by 12% was observed for the same reduced frequency at $\delta_A = 10°$. The mean lift coefficients for all test cases are presented in Figure 2.9. Figure 2.9(a) shows there are minor variations in mean C_L at zero AoA. Figure 2.9(b) shows that at $\alpha_0 = 10°$, the dynamic motion of TEF results in a monotonic increase in mean lift coefficient with both increasing pitching amplitude and increasing reduced frequency. For nearly all pitching amplitudes at $\alpha_0 = 10°$, the dynamic TEF produces larger mean lift coefficients than the corresponding static airfoil with no flap deflection at 10° AoA except for a 5° pitching amplitude oscillating at lower reduced frequencies ($k = 0.02$ and $k = 0.05$). In summary, *TEF oscillations about a nominally separated angle of attack consistently generate a higher lift coefficient than a static airfoil with zero flap deflection. An enhanced mean lift of* 12% *is generated by the largest TEF pitching amplitude* (10°) *at the highest pitching frequency* ($k = 0.12$)*, which is also the largest increase in mean lift relative to the static lift with zero flap deflection over the range of tested frequencies and pitching amplitudes.*

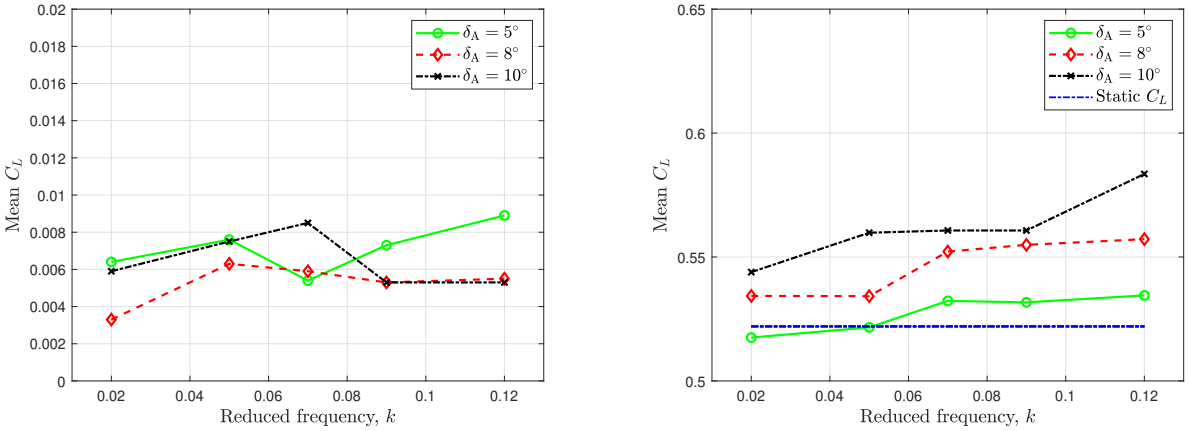

(a) Mean AoA = 0° (b) Mean AoA = 10°

Figure 2.9: Mean lift coefficients for all dynamic test cases

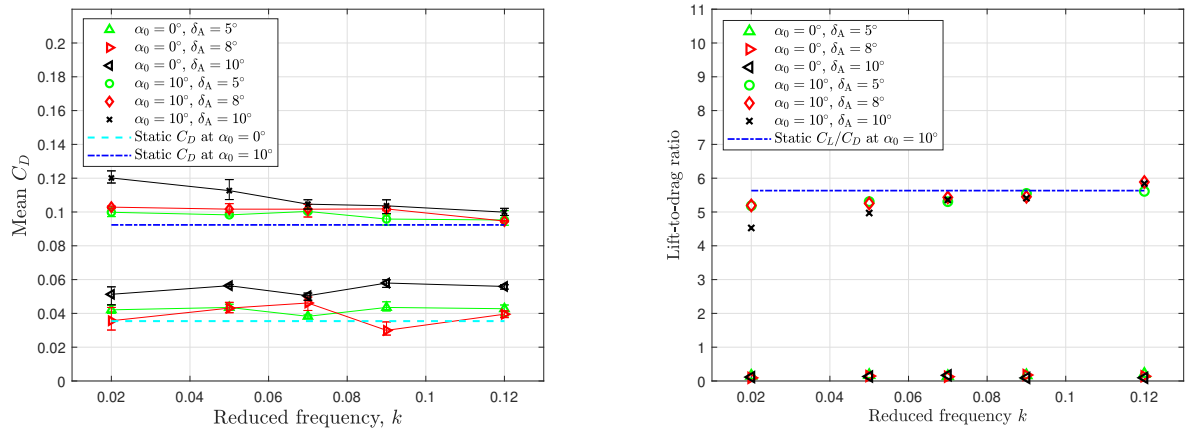

(a) Mean drag coefficient, C_D (b) Lift-to-drag ratios, C_L/C_D

Figure 2.10: Mean drag coefficients and lift-to-drag ratios for all dynamic test cases.

Direct drag force measurements for all dynamic TEF cases are also examined. Figure 2.10(a) presents a plot of the drag coefficients, and Figure 2.10(b) presents a plot of the lift-drag ratios for all tested cases. Figure 2.10(a) shows that no significant variations in drag were noticed at $\alpha_0 = 0°$ as a function of reduced frequency. Larger pitching amplitudes appear to generate a higher increase in mean drag coefficient from the baseline static C_D value at zero flap deflection. The drag coefficient results at $\alpha_0 = 10°$ also demonstrate minor

variations in C_D across the tested reduced frequencies for 5° and 8° pitching amplitudes. In contrast, dynamic TEF oscillations at 10° introduce additional larger mean drag forces into the flowfield at lower reduced frequencies but begin to overcome that additional drag beyond $k = 0.07$. Physically, the TEF oscillation generates enough wake energy (i.e., negative drag) to overcome the wake drag. The plot also shows consistency with results at $\alpha_0 = 0°$ in that small TEF pitching amplitudes achieve the least drag increase amongst other pitching amplitudes and that all pitching cases still produce a more considerable mean C_D than the static C_D. All pitching amplitudes demonstrate a measurable reduction in drag coefficient with increasing reduced frequency. The most substantial drop in mean C_D reduction was noticed for a pitching amplitude of 10° at $\alpha_0 = 10°$. These results are analogous to the formation of a reverse Von-K*árm*án vortex pattern in the wake of the airfoil, which would induce a jet-like flow in the opposite direction to the freestream flow, thus lowering the net drag force by generating thrust [50, 70]. The highest thrust production and arguably the strongest wake energy appear to be the most pronounced at large pitching amplitudes and high reduced frequencies only for $\alpha_0 = 10°$. This type of response is absent for TEF oscillations about $\alpha_0 = 0°$.

Figure 2.10(b) combines the mean lift coefficients obtained from Figure 2.9(b) with mean drag coefficients from Figure 2.10(a). A horizontal blue line is drawn to represent the static $C_L/C_D = 5.63$ at mean AoA of 10° with no flap deflection. When comparing the reported lift-to-drag ratio of 5.63 with literature, the static lift-to-drag ratio is slightly higher than L/D ≈ 3.2 at 10° angle of attack reported by Laitone [109] , who conducted his experiments at an equivalent $Re = 2.07 \times 10^4$ but for a three-dimensional NACA-0012 wing with an aspect ratio of 6. Both experimental and literature reported values represent a significant drop from L/D reported at higher Reynolds numbers that are commonly expected for conventional fixed and rotary aircraft configurations.

The dynamic lift-to-drag ratio continues to increase with increasing reduced frequency monotonically, but only onsets the static lift-to-drag ratio at $k = 0.09$. Only at $k = 0.12$, where the dynamic lift-to-drag ratio overcomes the static lift to drag ratio. An increase in lift-to-drag ratio of merely 5% was observed relative to the static C_L/C_D value was observed at the highest reduced frequency for both 8° and 10° pitching amplitudes. Although the mean lift from Figure 2.9(b) is the largest for 10° pitching amplitude, TEF dynamics at 10° pitching amplitude provides the lowest lift-to-drag ratio at lower reduced frequencies, mainly due to the significantly larger mean drag coefficients in produces at high pitching amplitudes. All data points for $\alpha_0 = 10°$ are quantified and summarized in Table 2.4. Data for mean $\alpha_0 = 0°$ do not show significant changes between static and dynamic force quantities.

In summary, *the least net drag increase relative to the static C_D with no flap deflection was produced for a dynamic TEF at small pitching amplitude (5°) and high oscillatory frequency. Additionally, the most significant increase in the mean lift coefficient is achieved at a large pitching amplitude (10°) and high oscillatory frequency. Despite these results, the optimized lift-to-drag ratio is generated at the intermediate pitching amplitude of 8°.*

Reduced frequency, k	$\delta_A = 5°$			$\delta_A = 8°$			$\delta_A = 10°$		
	C_L	C_D	C_L/C_D	C_L	C_D	C_L/C_D	C_L	C_D	C_L/C_D
0.02	0.518	0.100	5.18	0.534	0.103	5.19	0.544	0.120	4.53
0.05	0.522	0.099	5.31	0.534	0.102	5.25	0.560	0.113	4.97
0.07	0.532	0.100	5.31	0.552	0.102	5.43	0.561	0.105	5.36
0.09	0.532	0.100	5.55	0.555	0.102	5.45	0.561	0.104	5.41
0.12	0.535	0.095	5.61	0.557	0.095	5.89	0.584	0.100	5.84

Table 2.4: Mean lift, drag and lift-to-drag ratio summarized. Case: $\alpha_0 = 10°$

2.2.3 Frequency Response

When a stable linear time-invariant (LTI) dynamical system is driven by a sinusoidal input, the steady-state output is sinusoidal with the same frequency, but with magnitude (gain) and phase components that are modified by the system dynamics. The frequency response is simply the system's steady-state response to persistent sinusoidal forcing (i.e., the resulting magnitude and phase) over the full range of driving frequencies from zero to infinity. It is typically represented by a complex-valued "sinusoidal transfer function" $G(j\omega)$, corresponding to a transfer function $G(s)$ that describes the system's general input/output behavior in the Laplace domain. Specifically, the transfer function $G(s)$ maps input signals $U(s) = \mathcal{L}u(t)$ to output signals $Y(s) = \mathcal{L}y(t)$, where $\mathcal{L}$ denotes the Laplace transform.

The aerodynamic force and moment response of an airfoil to unsteady motion can also be represented by a transfer function whose input is the quasi-steady lift and whose output is the unsteady circulatory lift. We define the *gain function* of the system as an operator $G(k) = C_{L\text{circ}}/C_{L\text{QS}}$ which maps the (non-dimensional) quasi-steady lift force to the unsteady, circulatory lift force as a function of reduced frequency k. A frequency response is an effective way to characterize the aerodynamic response to sinusoidal pitching and plunging motion.

Theodorsen's solution of the lift coefficient per unit span on a thin rigid airfoil that is plunging and pitching harmonically is:

$$C_{L_{\text{Total}}} = \underbrace{\frac{\pi b}{U_\infty^2}\left(\ddot{h} + U_\infty\dot{\alpha} - ba\ddot{\alpha}\right)}_{C_{L_{\text{Added mass}}}} + \overbrace{\underbrace{2\pi\left(\frac{\dot{h}}{U_\infty} + \alpha + b(\frac{1}{2} - a)\frac{\dot{\alpha}}{U_\infty}\right)}_{C_{L_{\text{QS}}}} C(k)}^{C_{L_{\text{Circ}}}} \tag{2.2}$$

where the notations here were previously introduced and described first in (Eq. 2.1). Given

that the airfoil is fixed and does not vary with time (α and $\dot{\alpha} = 0$), and since there is no plunging motion (h=0), Leishman's formulation of lift coefficient from Eq. (2.2) can be re-arranged such that:

$$C_{L_{\text{Total}}} = \underbrace{-\frac{b^2}{U_\infty^2}F_1\ddot{\delta} - \frac{b^2}{U_\infty}F_4\dot{\delta}}_{C_{L_{\text{Added mass}}}} + \overbrace{\underbrace{2\pi\left(\alpha_0 + \delta_{\text{qs}}\right)}_{C_{L_{\text{QS}}}} C(k)}^{C_{L_{\text{Circ}}}} \tag{2.3}$$

The first group of terms in Eq. (2.3) is the non-circulatory lift components originating from the added mass forces due to the acceleration of the fluid around the airfoil. The second group of terms is the circulatory lift components (denoted as 'circ') that constitutes a quasi-steady component (denoted as 'QS') and a lift deficiency function $C(k)$ that accounts for the influence of the wake vorticity on the circulation around the airfoil.

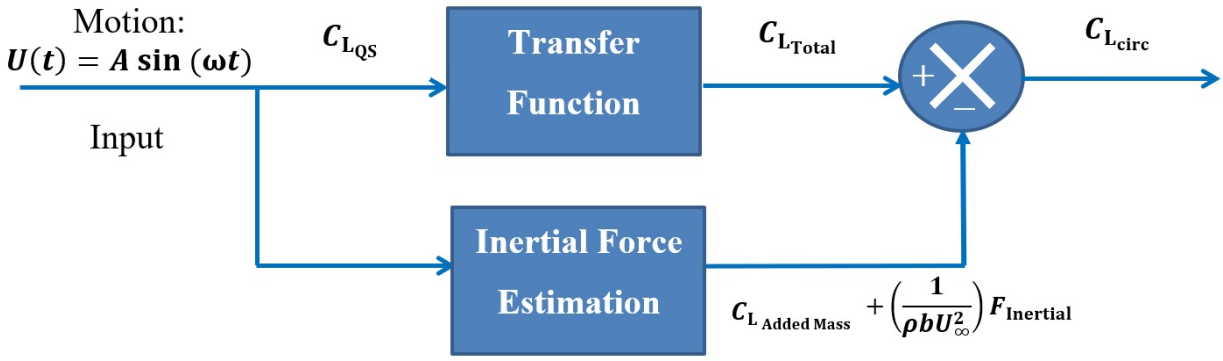

Figure 2.11: A representation of a linear dynamic system of unsteady lift.

Figure 2.11 shows a representation of the dynamic system for the generated unsteady lift. The input motion is a sinusoidal TEF oscillation about zero AoA at a prescribed frequency. The quasi-steady lift can be considered linear in response with the motion input (Taha et al. [5]), and as such, the input motion results in a periodic input to the transfer function (i.e., a sinusoidal variation in $C_{L_{\text{QS}}}$). The unsteady aerodynamic response is represented as an

output function with an associated lift deficiency (or enhancement) $M_G = |G(k)|$, and phase shift $\phi = \angle G(k)$. An additional set of non-circulatory forces that includes the fluid's added mass force and an inertial load arising from the TEF's rigid body motion is tared from the absolute total lift $C_{L_{\text{Total}}}$ in the frequency domain to obtain the "true" value of the unsteady circulatory lift. By experimentally determining the relative magnitude M_G and phase shift ϕ between the TEF's motion input and unsteady circulatory lift output, we can construct the frequency response for the combination of flap pitching amplitudes and reduced frequencies. The lift gain of the system can be determined from force measurements by the left term in Eq. (2.4) :

$$M_G = \frac{|C_{L_{\text{circ}}}|}{|C_{L_{\text{QS}}}|} \quad \text{and} \quad \phi = \cos^{-1}\left(\frac{\vec{\delta_{\text{A}}} \cdot \vec{C_L}}{|\vec{\delta_{\text{A}}}||\vec{C_L}|}\right) \tag{2.4}$$

where $|C_{L_{\text{circ}}}|$ in the left term of Eq. (2.4) is the circulatory lift amplitude of the periodic signal, and $|C_{L_{\text{QS}}}|$ is the quasi-steady lift obtained from the static lift slope in Figure 2.5(d). The right term of Eq. (2.4) is the phase shift ϕ, and is determined using the dot product between two vectors in signal space, with one vector being the measured TEF pitching amplitude from the potentiometer readings, $\vec{\delta_{\text{A}}}$ and the other vector being its respective lift response, $\vec{C_L}$. The dot product was used on 10 seconds of post-filtered steady-state lift response and averaged over the three experimental trials. The numerical approach was applied analytically on Theodorsen's formulation in Eq. (2.2) and produced similar gain and phase outputs to the approximations determined by Bisplinghoff et al. [110] on Theodorsen's transfer function. In equation form, the circulatory lift coefficient amplitude per unit span is expressed as:

$$|C_{L_{\text{circ}}}| = |C_{L_{\text{Total}}}| - |C_{L_{\text{Added Mass}}}|e^{i\phi} - \left(\frac{1}{\rho b U_\infty^2}\right) F_{\text{inertial,max}} e^{i\phi} \tag{2.5}$$

Here, $C_{L_{\text{Added Mass}}}$ is the fluid's added mass, and $F_{\text{inertial,max}}$ is the maximum inertial force arising from the TEF's self-weight executing its motion at a given driving frequency. Both added mass and inertial force terms are a function of $\ddot{\delta}$. The maximum inertial is approximated as $F_{\text{inertial,max}} = mA(2\pi f)^2$, where m is the mass of the TEF section of the wing (measured at approximately 18.2 grams), and A is the TEF's vertical amplitude at its mid-point which is determined by the pitching amplitude δ_A. We can use the theoretical prediction of added mass in the formulation, but for the range of tested reduced frequencies, the circulatory force dominates the non-circulatory added mass lift by nearly three orders of magnitude. Additionally, the fluid's added mass is on the order of $\mathcal{O}(10^{-4})$ N and cannot be accurately measured due to the load cell's limitation with resolution. The added mass term is, therefore, statistically insignificant at the tested reduced frequencies and can be neglected.

In practice, a lag between the build-up of lift response following a TEF motion has to be present. The maximum instantaneous lift development at the time of the maximum inertial force is not physically achievable and has to be associated with a phase lag, ϕ. Precisely, that lag is the between the total lift response and the TEF motion. We previously defined the TEF motion as a pure sinusoidal input, as a function of δ. In theory, the maximum inertial force is a function of the second derivative of a sinusoidal signal, which is also sinusoidal. Therefore, the instantaneous lift response also lags the TEF's acceleration (thus the maximum inertial force) at the maximum upstroke (and downstroke) position by an angle, ϕ.

Computing the phase shifts

Figure 2.12 shows a sample of one steady-state period of lift response (solid blue line), and its respective TEF pitching amplitude (dashed red line) for each test case at $\alpha_0 = 0°$. The two curves are time-stamped at zero initial conditions, and the results show a lag in the lift build up that becomes pronounced at higher reduced frequencies. For a handful of cases, the

lift build-up peaks right before the TEF reaches its maximum downstroke position, a typical lift transient response of a rapidly pitching airfoil. This behavior is observed at $k = 0.12$ for all flap deflections in Figures 2.12(c) 2.12(f) and 2.12(i), and is also noticeable at a lower reduced frequency ($k = 0.07$) for $\delta_A = 10°$ as shown in Figure 2.12(h).

Figure 2.13 shows one steady-state period of the unsteady lift response and its corresponding TEF motion for all pitching amplitudes at $\alpha_0 = 10°$. All responses in phase shift at $\alpha_0 = 10°$ depict similar characteristics to the responses produced at $\alpha_0 = 0°$ by showing a time lag in the lift build up, which increases with increasing reduced frequency. The difference is that the effect of lift transient response almost disappears for TEF oscillations around $\alpha_0 = 10°$.

Figure 2.14 summarizes the phase shifts obtained for all test cases. The phase shift continues to increase with increasing reduced frequency for all pitching amplitudes monotonically. The phase shifts at $\alpha_0 = 10°$ present no significant variation from responses generated at $\alpha_0 = 0°$ for $\delta_A = 5°$. However, the phase shifts for $\delta_A = 8°$ and $10°$ are lower at $\alpha_0 = 10°$ compared to their corresponding phase shifts at $\alpha_0 = 0°$. Larger pitching amplitudes in a nominally separated flow results in the least phase lag between the system's input and output. The relationship between phase shift and reduced frequency is approximately quadratic for all pitching amplitudes.

The rate of evolution of vorticity in the wake that trails an oscillating airfoil produces a phase shift between the aerodynamic response and the airfoil's motion [111]. A phase shift in lift response is likely to occur at high operational frequencies because of strong viscous effects in the flow ([6, 112, 113]). Another study conducted by Ericsson and Reding [97] shows that the phase lag in the unsteady flow response relative to quasi-steady flow can be categorized as (a) circulation lag, (b) convective viscous flow time lag, which is the effect of the induced change of Reynolds number, and (c) moving separation point effect caused by the adversity in pressure gradient. Ericsson and Reding [97] also concluded that boundary layer

characteristics improved as a result of time lags in the accelerated flow around a dynamic airfoil, causing delays in flow separation and the lift build up in rapid pitching airfoils. It is clear from Figures 2.13(f) and 2.13(i) that the lift transients that were otherwise noticeable for flow at $\alpha_0 = 0°$ are delayed at $\alpha_0 = 10°$. By the time the TEF executes an upstroke motion, the flow does not have enough time to catch up with the flap motion. As such, the flow fails to generate a transient lift response.

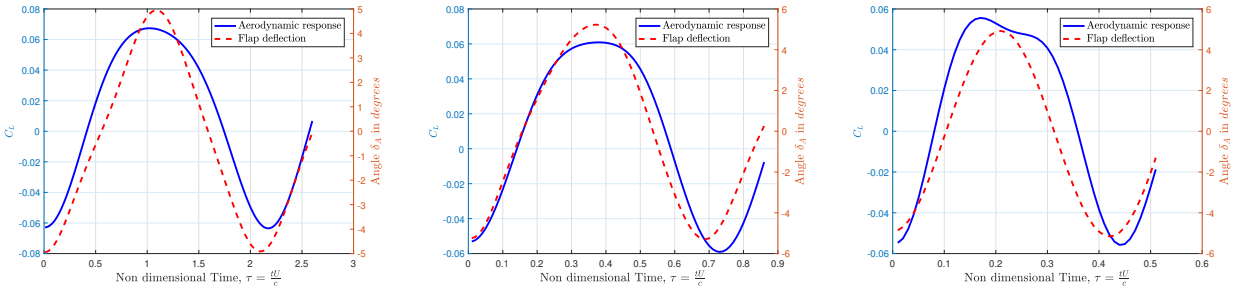

(a) k=0.02, $\delta_A = 5°$ (b) k=0.07, $\delta_A = 5°$ (c) k=0.12, $\delta_A = 5°$

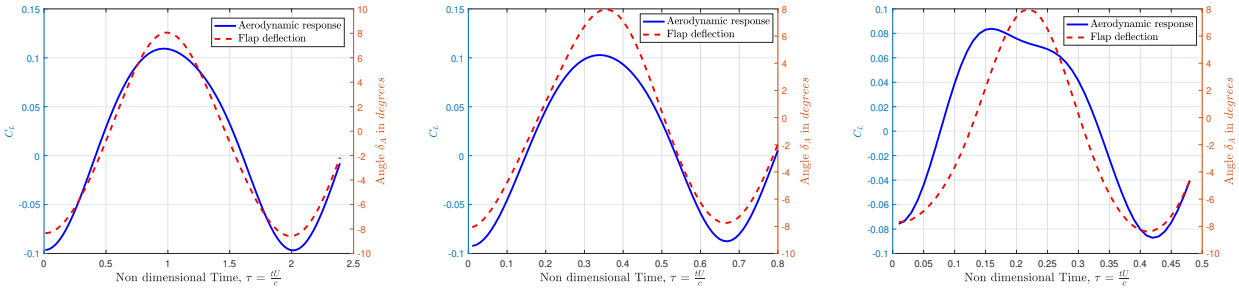

(d) k=0.02, $\delta_A = 8°$ (e) k=0.07, $\delta_A = 8°$ (f) k=0.12, $\delta_A = 8°$

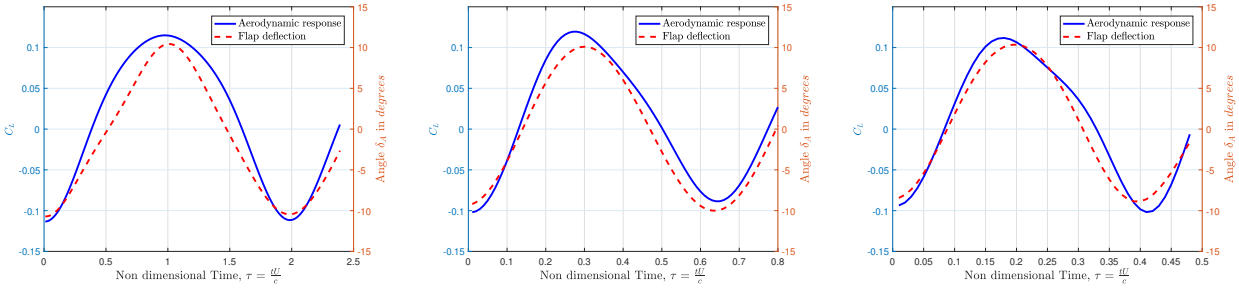

(g) k=0.02, $\delta_A = 10°$ (h) k=0.07, $\delta_A = 10°$ (i) k=0.12, $\delta_A = 10°$

Figure 2.12: Phase shift : Lift response against TEF motion at $\alpha_0 = 0°$

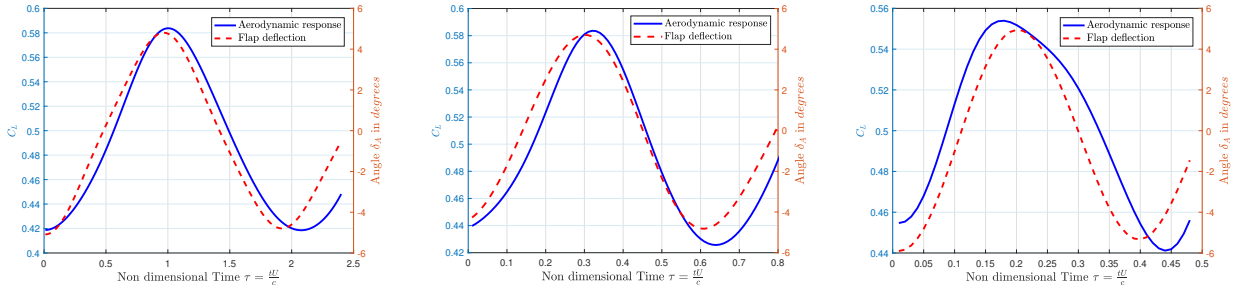

(a) k=0.02, $\delta_A = 5°$ (b) k=0.07, $\delta_A = 5°$ (c) k=0.12, $\delta_A = 5°$

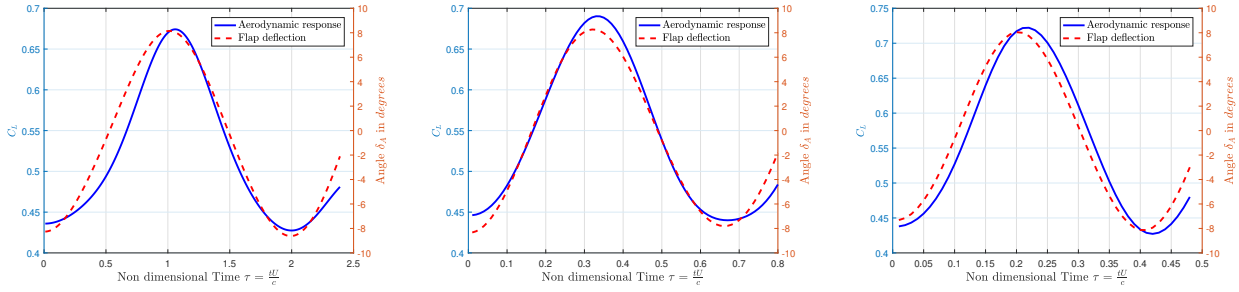

(d) k=0.02, $\delta_A = 8°$ (e) k=0.07, $\delta_A = 8°$ (f) k=0.12, $\delta_A = 8°$

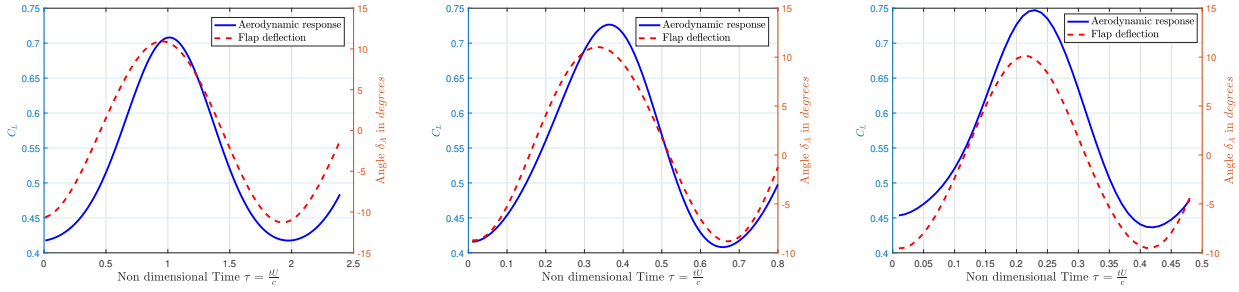

(g) k=0.02, $\delta_A = 10°$ (h) k=0.07, $\delta_A = 10°$ (i) k=0.12, $\delta_A = 10°$

Figure 2.13: Phase shift : Lift response against TEF motion at $\alpha_0 = 10°$

Computing the lift amplitudes

The total lift amplitude generated for each TEF's lift response is obtained from the peak of its respective power spectrum density (PSD) as computed from the FFT of the periodic signal. If only a linear response is considered, the primary component of the PSD is a good approximation of the unsteady linear lift amplitude. To ascribe a physical meaning to the lift amplitude at a specific frequency, take the square root of twice the PSD peak value. Figure

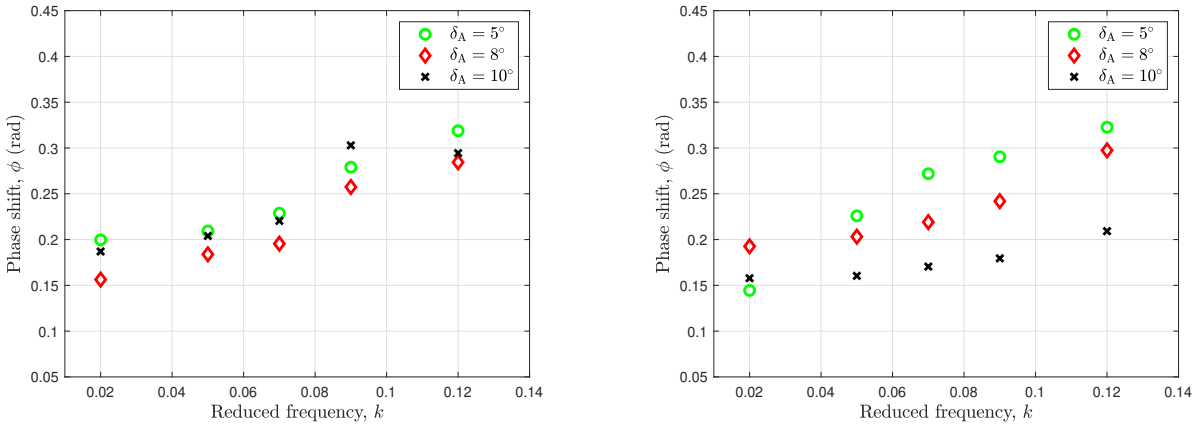

(a) Phase shift at $\alpha_0 = 0°$

(b) Phase Shift at $\alpha_0 = 10°$

Figure 2.14: Phase shift for all flap deflection amplitudes at $\alpha_0 = 0°$ and $\alpha_0 = 10°$

3.14 shows a sample of PSD analysis on the lift coefficient response at $k = 0.12$ for $\delta_A = 8°$ and $10°$ at AoAs $\alpha_0 = 0°$ and $\alpha_0 = 10°$. The power peaks (units of $1/s^2$) show intensified lift amplitude for dynamic TEF around $\alpha_0 = 10°$ compared to $\alpha_0 = 0°$. Non-linear unsteady aerodynamic behavior is observed as shorter peaks at the second and third harmonics of the driving frequency, and these are significantly weaker than the primary peaks at these tested conditions. The presence of lift peaks at the harmonics of the fundamental frequency can be evidence of a non-linear flow mechanism, possibly due to lift enhancement [13, 114].

Figure 2.16(a) displays the maximum rigid body inertia forces supplied by the TEF motion and were found to contribute around 4% to 5% of the maximum lift coefficient. Figure 2.16(b) shows the resultant circulatory lift amplitudes for all test cases after taring the maximum inertia forces from their respective absolute total lift, $|C_{L_{\text{Total}}}|$. Enhanced lift circulation in post-stalled flow is typically associated with increased vorticity and large pressure differentials in the flow field. Force measurements show that the largest TEF pitching amplitude produces the largest circulatory lift amplitude when pitching around $\alpha_0 = 10°$. An increase in inbound circulation over the airfoil could signal LEV formation and stability. The evolution

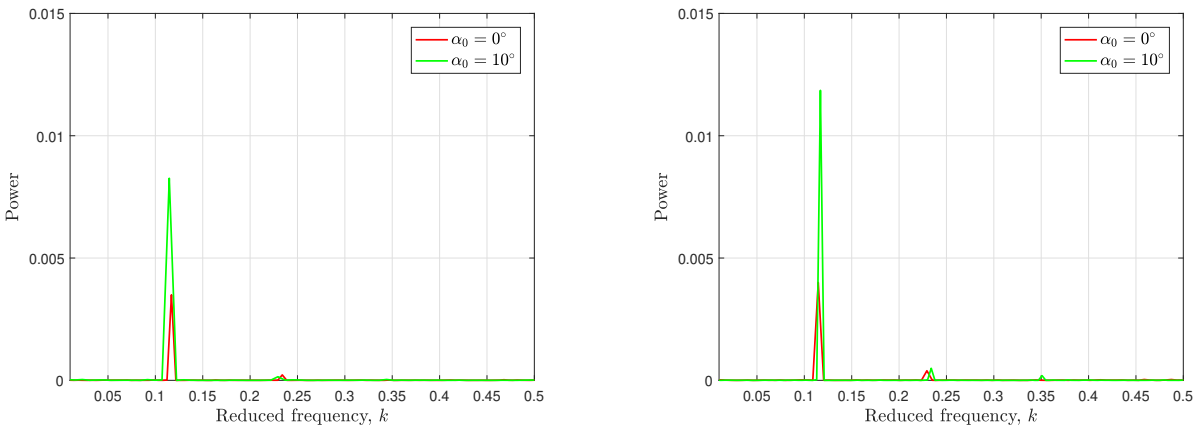

(a) $\delta_A = 8°$ (b) $\delta_A = 10°$

Figure 2.15: A PSD sample on lift coefficient measurements at $k = 0.12$

of vorticity around the TEF and its wake are unique for every test case. If a LEV is formed, it could either remain attached to the airfoil's surface or it could destabilize and detach from the airfoil's surface (Zakaria et al. [13], Medina and Rockwood [48]). An attached LEV is expected to generate more circulation and additional lift. Higher maximum lift coefficients could also be influenced by the location of the reattachment point of the separated flow. It is possible that the reattachment process takes place within the tested conditions and that it occurs farther upstream with increasing reduced frequency.

The lift gain is obtained by normalizing the unsteady circulatory lift gain with the quasi-steady lift determined at various static flap deflection from 2.5(d). The quasi-steady lift is quantified as the lift increment between $\delta_{TE} = 0°$ and $\delta_{TE} = 5°$ for all pitching amplitudes. The lift gain as a function of reduced frequency for $\alpha_0 = 0°$ and $\alpha_0 = 10°$ is quantified in Figure 2.17 and compared with approximations of Theodorsen's transfer function (Bisplinghoff et al. [110]). Isolating the effects of reduced frequency and pitching amplitudes, the lift gain in Figure 2.17(a) agrees with Theodorsen's model in the sense that the lift gain monotonically decreases with increasing reduced frequency. The airfoil experiences lift deficiency in

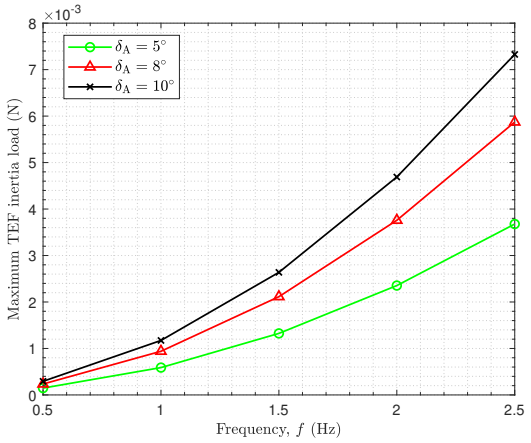

(a) Maximum TEF inertia loads

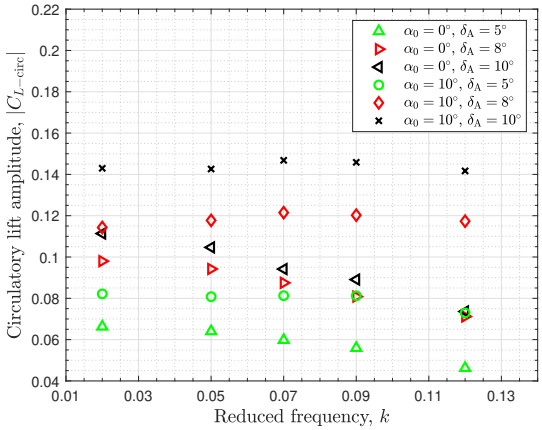

(b) Circulatory lift amplitudes, $|C_{L_{\text{circ}}}|$

Figure 2.16: Computing the circulatory lift component

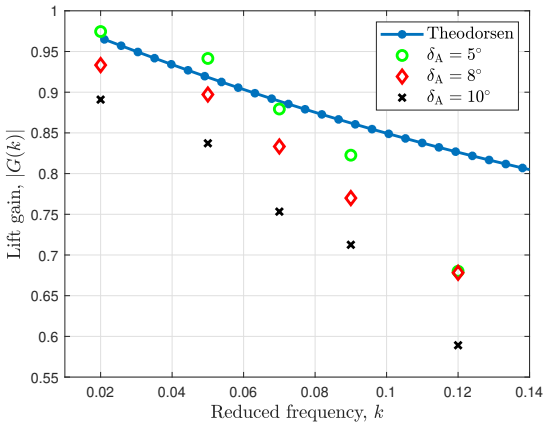

(a) Lift gain - $\alpha_0 = 0°$

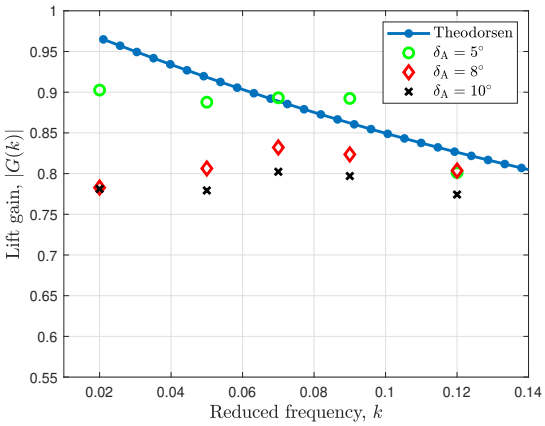

(b) Lift gain - $\alpha_0 = 10°$

Figure 2.17: Lift gain $|G(k)|$ - Frequency response for all TEF pitching amplitudes at $\alpha_0 = 0°$ and $\alpha_0 = 10°$

junction with Theodorsen's approximation from potential flow theory. The lift gain also agrees well with Theodorsen's gain for lower reduced frequencies at $\delta_A = 5°$ (i.e., near quasi-steady conditions). In contrast, the effect of large pitching amplitudes and higher reduced frequencies result in additional lift deficiency. Another important observation from Figure 2.17(b) is that the lift gain peaks at reduced frequencies around $k = 0.07$ and 0.09, and drops off towards $k = 0.12$. This behavior is pronounced at higher pitching amplitudes of 8° and

10° and contradicts the lift responses generated by TEF pitching at $\alpha_0 = 0°$ 2.17(b). Even though the largest circulatory lift was produced by a 10° pitching amplitude, the largest lift gain was noticed for pitching amplitude of $\delta_A = 5°$. On the other hand, although the unsteady circulatory lift is deficient from the quasi-steady value (i.e., the lift gain is lower than 1), the lift contribution increases with increasing frequency. Large pitching amplitudes does indeed produce the least efficient lift within the dynamic system (input/output). The optimum lift gain was observed for pitching amplitude of $\delta_A = 5°$ compared to 8° and 10°. In summary, *the TEF dynamic system is still lift deficient relative to the quasi-steady conditions. But, the fact that the circulatory lift amplitude continues to increase with increasing frequency at a nominally separated flow, which isn't the case in a fully attached flow, implies that the airfoil experienced an enhancement in circulation in its global flowfield.*

2.2.4 Aerodynamic Hysteresis Effects

The investigation of lift hysteresis at low Reynolds number can provide useful information on how dependent the flow history is on the localized change of TEF amplitude. There are several distinct characteristics to look for in a hysteresis loop: the gap width, the slope of the loop, and any shape irregularities in the loop that can signal whether the flow is fully attached, fully separated, or reattached.

Figures 2.18(a), 2.18(c) and 2.18(e) show one cycle of instantaneous lift developed by the TEF motion around $\alpha_0 = 0°$. The shape of the loop at $\delta_A = 5°$ indicates that the flow is fully attached, and a small gap area shows that no significant hysteresis effects take place. Loops with slightly wider gaps are observed for higher pitching amplitudes and higher reduced frequencies. The gap widening signals the presence of a phase shift between the lift response and its respective TEF motion. Significant phase shifts are observed for loops with wider

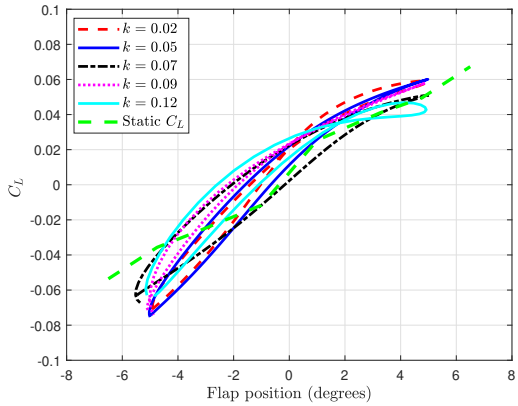

(a) TEF pitching amplitude $\delta_A = 5°$, $\alpha_0 = 0°$

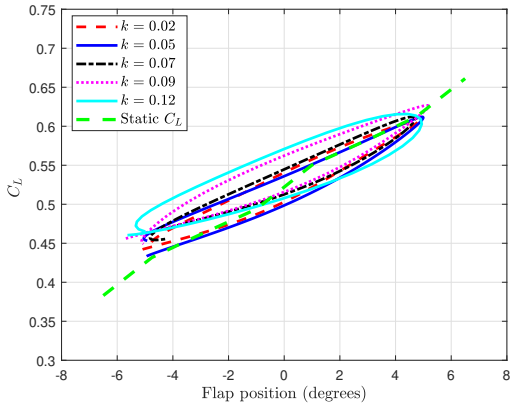

(b) TEF pitching amplitude $\delta_A = 5°$, $\alpha_0 = 10°$

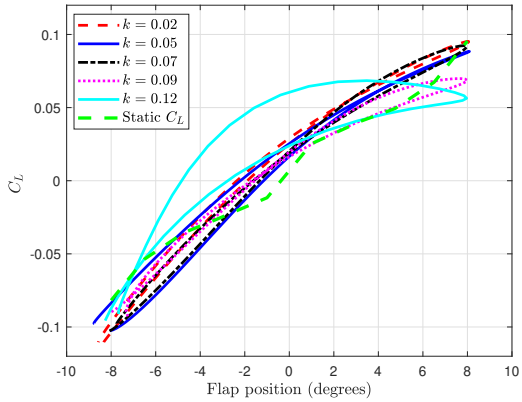

(c) TEF pitching amplitude $\delta_A = 8°$, $\alpha_0 = 0°$

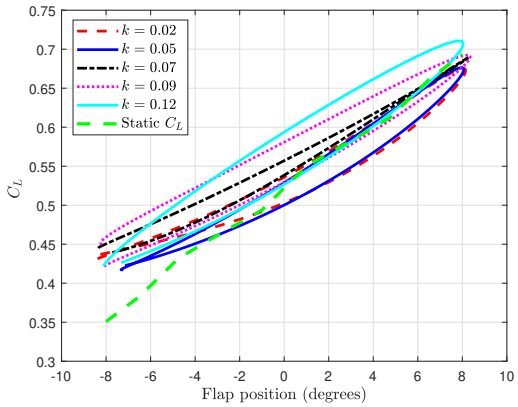

(d) TEF pitching amplitude $\delta_A = 8°$, $\alpha_0 = 10°$

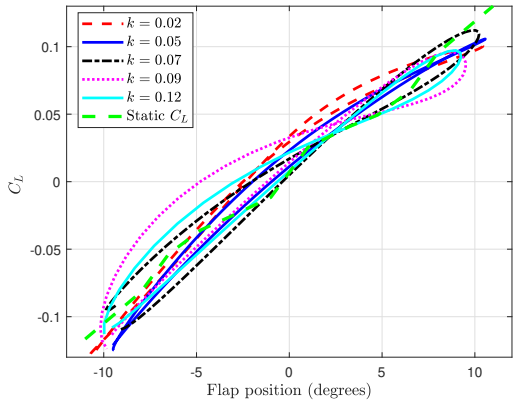

(e) TEF pitching amplitude $\delta_A = 10°$, $\alpha_0 = 0°$

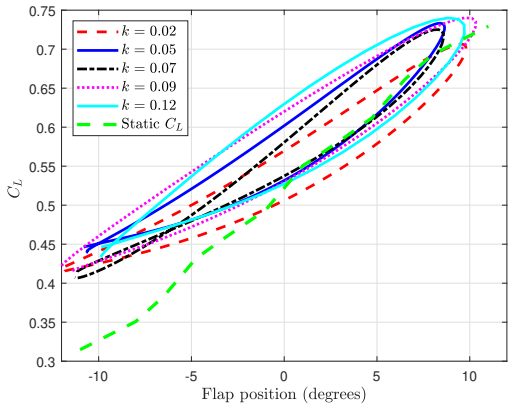

(f) TEF pitching amplitude $\delta_A = 10°$, $\alpha_0 = 10°$

Figure 2.18: Dynamic hysteresis for all test cases

gaps. For all reduced frequencies at $\delta_A = 5°$, the lift responses trace loops with slightly steeper slopes than the measured static slope, and wider gaps compared to lower pitching amplitudes. At $\delta_A = 8°$ and $10°$, the lift responses are looping around a slope similar to the C_L static slope. The outliers from the experimental data are the 'knot-like' shape that is displayed by the loops for $k = 0.09$ and $k = 0.11$ at all pitching amplitudes at $\alpha_0 = 0°$. This behavior was also noticed by Bergami et al. [115] for a pitching amplitude of $5°$ in the attached flow and might be associated with a transient lift dynamic response that results in an overshoot during the inception of a rapid pitching maneuver.

Figures 2.18(b), 2.18(d), 2.18(f) show one cycle of instantaneous lift produced by TEF motion at $\alpha_0 = 10°$. The lift response in separated conditions gives rise to larger dynamic hysteresis effects. Because there is no sudden drop in C_L with the local change of effective AoA, the loops show that there is no flow separation that is typically expected at a static stall AoA of $10°$. The non-constant variation in gap width for cases $\delta_A = 8°$ and $10°$ is evidence of a strong aerodynamic hysteresis effect and can be associated with the enhanced lift as observed by the significant local C_L near larger positive TEF pitching angles. This behavior is also noticed for $\delta_A = 5°$ at $k = 0.12$. It appears that the cycles at $\delta_A = 8°$ and $10°$ present significant temporally evolving mean lift values that are gradually drifting from the static mean value at higher reduced frequencies producing less steep slopes compared to the C_L static slope line. Finally, the dynamic hysteresis loops suggest a mean C_L variation with δ_A that is slightly translated upwards and towards the positive C_L axis. This behavior also agrees with Bergami's [115] simulations for $\delta_A = 5°$ where the hysteresis shows a significant variation in mean C_L for a dynamic TEF oscillating around a statically stalled AoA despite the difference in flow regimes.

2.3 Summary of Contributions

The lift responses of a dynamic TEF undergoing simple harmonic motion at various frequencies and pitching amplitudes were investigated with the airfoil's leading element fixed at two AoAs: $\alpha_0 = 0°$ corresponding to a fully attached steady flow condition, and $\alpha_0 = 10°$ corresponding to a separated flow condition. The unsteady lift responses were obtained from force measurements inside a wind tunnel and compared with lift responses generated by a quasi-steady model using Leishman's formulation for a two-element airfoil configuration. A frequency response was constructed by determining the lift gain and phase shifts between the quasi-steady and unsteady total lift. The change in unsteady circulation was quantified by utilizing the frequency response approach. Based on the results of this chapter, the following was observed:

Experimental results against Leishman's model

The quasi-steady model accurately captures the general trends of unsteady lift obtained from the experimental results for the fully attached flow case ($\alpha_0 = 0°$). Results are validated for the quasi-steady lift as a result of combined oscillatory pitching amplitudes and reduced frequency effects. Minor under-predictions of the results by the quasi-steady model were demonstrated at higher reduced frequencies and pitching amplitudes to which the flow becomes relatively unsteady. The quasi-steady model becomes unable to predict unsteady lift response for the separated flow case ($\alpha_0 = 10°$) for the majority of the oscillatory parameters since there was no incorporation of the changes in the lift amplitude and dynamic variations in the mean lift into the quasi-steady model. However, discrepancies between the experimental results and predictions made by the quasi-steady model provided useful qualitative insight on how much unsteady and non-linear the flow becomes at a given combined pitching

amplitude and reduced frequency.

Lift enhancement and drag reduction

The flow around an oscillating TEF at a nominally separated AoA ($\alpha_0 = 10°$) provides enhanced lift well beyond what would be provided by TEF oscillations in a fully attached flow ($\alpha_0 = 0°$). Lift enhancement was observed in two forms: an increase in the generated mean lift, and an increase in circulatory lift amplitudes, both achieved at the largest TEF pitching amplitudes and high reduced frequencies at $\alpha_0 = 10°$. No variation in the mean lift and no enhancement in lift amplitudes were observed for TEF oscillations around $\alpha_0 = 0°$.

No significant benefits in drag performance were noted for TEF dynamics at $\alpha_0 = 0°$ for the range of tested pitching amplitudes and reduced frequencies. In general, the drag coefficients generated by the dynamic TEF at $\alpha_0 = 0°$ are higher than static C_D. Results indicated that the flow around the airfoil with a dynamic TEF at $\alpha_0 = 10°$ also encountered additional drag for all tested pitching amplitudes and frequencies. No drag reduction was noticed at any of the tested conditions. However, the additional drag was overpowered by negative drag production (thrust) when the TEF oscillated at higher reduced frequencies. The smallest pitching amplitude resulted in the least drag increase from their respective static C_D values. Although the most substantial drag coefficient increase occurred at 10° pitching amplitude, large amplitude TEF oscillations also generated the strongest wake energy as quantified by the largest drop in mean C_D between $k = 0.05$ and $k = 0.07$. The optimum lift-to-drag ratio is achieved at $\alpha_0 = 0°$ for 8° pitching amplitude.

For TEF oscillations about $\alpha_0 = 10°$, the lift gain at $\delta_A = 5°$ closely matches the lift gain from Theodorsen's transfer function at lower reduced frequencies but presented significant discrepancies at higher reduced frequencies and larger pitching amplitudes. For TEF oscil-

lations about $\alpha_0 = 10°$, the TEF dynamic system achieved the most significant lift gain at $k = 0.07$ and 0.09. Isolating the effects of reduced frequency and pitching amplitudes, the system outputs the most significant lift gain at the lowest pitching amplitude. The phase lag between the TEF motion and lift build up monotonically increase with increasing frequency at both $\alpha_0 = 0°$ and $\alpha_0 = 10°$. One significant observation is that the phase shifts for $\delta_{\mathrm{A}} = 8°$ and 10° pitching amplitudes were significantly lower compared to their corresponding phase shifts at $\alpha_0 = 0°$. Viscous effects and transitional flow effects can be reasons that the flow induces significant phase shifts at higher reduced frequencies at the current Reynolds number. For the case of $\delta_A = 10°$ at $\alpha_0 = 10°$, increased circulatory lift and reduced phase shifts between the TEF motion and lift response provide reasonable evidence that the lift lag is also induced by incremental changes in circulatory lift amplitude.

Aerodynamic Hysteresis

Finally, dynamic hysteresis effects showed that there is a local variation in the mean lift with changing TEF motion in every lift cycle. Hysteresis effects also show that for both fixed AoAs, the loop gaps are largest at higher flap deflection reduced frequencies. The dynamic mean lift exhibits a different slope from the static slope. The 'knot-like' loops at $\alpha_0 = 0°$ are evidence of strong hysteresis effects that occurred at higher reduced frequencies. Strong aerodynamic hysteresis effects were also observed for $\delta_{\mathrm{A}} = 8°$ and 10° at $\alpha_0 = 0°$. No flow separation was observed for the dynamic TEF at $\alpha_0 = 10°$.

Beyond these observations, flow through visualization would be of great interest to fully understand the fundamental physics behind the claims presented in this chapter. The results from this effort are also aimed to supplement the ongoing activity of semi-empirical modeling and system identification to represent the unsteady lift of the dynamic system obtained from the constructed frequency response. An improved low fidelity semi-empirical formulation

that extends viscous effects or a phase lag parameter into the model can be useful to study the controllability of TEFs in a regime that is commonly known to be transitional in flow.

2.4 Summary of Major Findings

- Leishman's model compares well with experimental results for low reduced frequencies and low pitching amplitudes.
- Enhancement in the generated mean lift of up 12% to was observed at TEF oscillations of 10° mean AoA.
- The least drag increase relative to the static drag at zero flap deflection occurred at 10° mean AoA for $\delta_A = 5°$.
- The most significant increase in lift-to-drag ratio occurred at 10° mean AoA for higher pitching amplitudes.
- The largest circulatory lift gain was achieved at 10° mean AoA for $\delta_A = 5°$.
- The phase lag between the flap's motion and the lift response is mitigated for larger flap pitching amplitudes at 10° mean AoA.

Chapter 3

Aerodynamic Response of a NACA-0012 Airfoil Undergoing Non-Sinusoidal Pitching Waveforms

The contents of this chapter are based on the preliminary results of the following article: *Shehata, H., Zakaria, M. Y., Hajj, M. R., Woolsey, C. A. (2019). Aerodynamic Response of a NACA-0012 Airfoil Undergoing Non-Sinusoidal Pitching Waveforms. In AIAA Scitech 2019 Forum (p. 0303). [116].*

The forces on a NACA-0012 airfoil undergoing different pitching waveforms were investigated experimentally. Four different pitching trajectories, including sinusoidal, trapezoidal, sawtooth, and reverse sawtooth waveforms, were considered. The airfoil was set at mean angles of attack (AoA) of α_0= 3.5°, 7°, and 12° representative of a fully attached, incipient light-stall, and incipient post-stall flow states. All trajectories execute a nominally identical pitching amplitude of $\alpha_A = 3.5°$ and reduced frequencies between $k = 0.02$ and 0.14. The chord-based Reynolds number for this experiment is $Re = 2.1 \times 10^4$. Static lift and drag coefficients were measured first to provide a baseline for comparison. During the wind tunnel testing, the critical aerodynamic data that were measured are a) lift coefficient time histories, b) unsteady lift coefficient amplitudes (magnitudes), and (c) mean lift, mean drag and lift to drag ratios. Our interest also lies in the assessment of any effects of enhanced lift that may

arise from unsteady pitching motions at various frequencies of oscillations and mean angles of attack. Finally, the validity of utilizing a quasi-steady extension of Theodorsen's model and an unsteady state-space model developed by Taha [117] is examined and compared with the lift from experimental measurements.

3.1 Experimental Setup

Details on the wind tunnel test facility and airfoil test article were previously described in section 2.1.1. The spanwise gap between the flap and the leading element of the airfoil was sealed with a smooth thin tape. The NACA-0012 airfoil is connected to a push rod at the quarter chord point. The push rod connects to a continuous FS90R micro-servo that provides the pitching motion. The lift, drag, and the airfoil's angular positions were acquired using the same data acquisition system described in section 2.1.2.

3.1.1 Experimental Test Matrix

The effects of pitching kinematics are studied for various mean angles of attack and periodic rates. A simple harmonic motion (a sinusoidal waveform) is first executed as the baseline test case for all waveforms. The other pitching kinematics utilized for this study are the trapezoidal, sawtooth and reverse sawtooth waveforms. The airfoil undergoes a pitch-up and a pitch-down maneuver about a mean angle of attack α_0 in a uniform free stream flow, with an identical nominal mean-to-peak pitching amplitude of $\pm 3.5°$. Figure 3.1 provides a schematic overview of the airfoil motion with respect to α_0.

First, the steady force measurements were gathered for angles of attack between 0° and 20°. Second, the dynamic operation of the pitching motion was set to undergo pitching in three

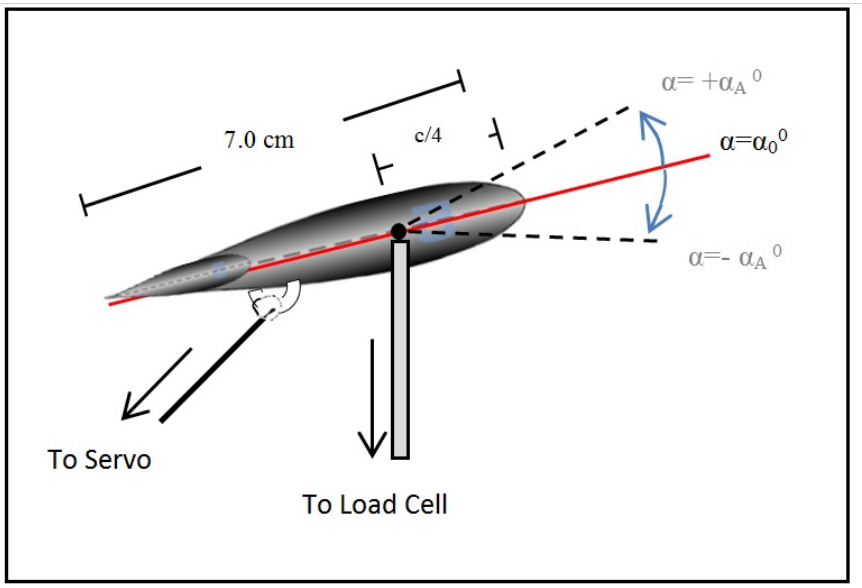

Figure 3.1: Schematic of the airfoil

different flow states. One flow state represents a nominally fully attached flow where the mean angle of attack is set to 3.5°. Another flow state represents incipient light-stall from fully attached with a mean angle of attack of 7°. The third and final flow state represents incipient post-stall from pre-stall flow condition with a mean angle of attack of 12°. Both static and dynamic experiments were conducted at a Reynolds number of $Re = \ 2.1 \times 10^4$. A summary of the dynamic operating conditions is presented in table 3.1.

Table 3.1: Airfoil pitching parameters for all waveforms

Mean AoA, α_0	Pitching amplitude, α_A	Reduced frequency, k	Flow Conditions
3.5°	3.5°	0.02 - 0.14	Fully attached
7°	3.5°	0.02 - 0.14	Attached,light stall
12°	3.5°	0.02 - 0.14	Light stall, post-stall

The prescribed inputs of each waveform are demonstrated in Figure 3.2(a). Figure 3.2(b) shows the equivalent post-filtered angular positions obtained from the servo controller's potentiometer. A Chebyshev Type II filter was used to remove excess noise from the potentiometer readings. We used a less aggressive cut-off frequency while applying the filter to

the sawtooth and reverse sawtooth voltage readings in order to preserve the absolute values of the periodic signal. All analogue voltage readings were transformed to a physical angular position in degrees using a calibrated linear fit curve.

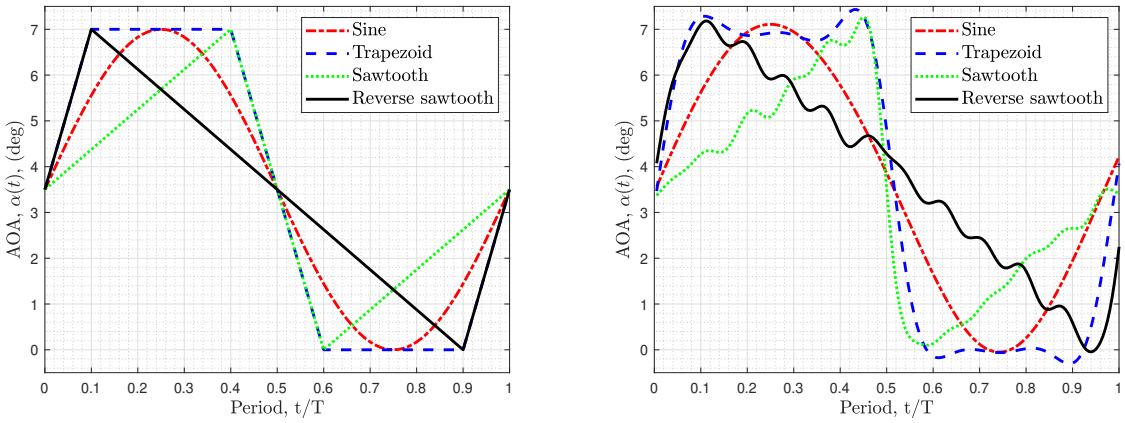

(a) Prescribed waveforms for present study

(b) Waveforms measured experimentally for present study

Figure 3.2: Prescribed vs measured pitching waveforms at 3.5° mean AoA.

Each waveform is prescribed such that selected segments within one period of motion execute a pitch-up and pitch-down motion at different rates. The sinusoidal waveform is prescribed as $\alpha(t) = \alpha_0 + \alpha_A \sin(\omega t)$, where $\omega = 2\pi f$ is the angular pitching rate, and f is the forcing frequency. With T indicating one full period of motion, the remaining three waveforms initially executed from α_0 are prescribed as follows:

- **trapezoidal**: Impulse pitch-up motion for 0.1 T, hold for 0.3 T, impulse pitch-down for 0.2 T, hold for 0.3 T, impulse pitch-up for 0.1 T
- **Sawooth**: Linear pitch-up for 0.4 T, impulse pitch-down for 0.2 T, linear pitch-up for 0.4 T
- **Reverse sawtooth**: Impulse pitch-up for 0.1 T, linear pitch-down for 0.8 T, impulse pitch-up for 0.1 T

The three non-sinusoidal waveforms combine low rates of linear motion with high rates of linear motion, but they remain periodic. The trapezoidal waveform looks like a square wave where the motion is initiated with an impulse pitch-up motion to an angular position of $\alpha_0 + \alpha_\mathrm{A}$, followed by a steady hold, an impulse pitch-down motion to an angular position of $\alpha_0 - \alpha_\mathrm{A}$ before returning to α_0. Because of actuator limitations, the impulse motion is executed at a rate of 0.1 T per 3.5°, or equivalently, 1.64 T per radian. The sawtooth and reverse sawtooth waveforms can be viewed as a "skewed" sinusoidal pitching. The sawtooth motion executes a gradual pitch-up motion to $\alpha_0 + \alpha_\mathrm{A}$ followed by an impulse pitch down motion, whereas the reverse sawtooth is initiated by an impulse pitch-up motion to $\alpha_0 + \alpha_\mathrm{A}$ followed by a gradual pitch-down motion. These three motions present discontinuities in the rate of the angle of attack at periods whenever there is a sudden change in motion states.

3.2 Results and Discussion

3.2.1 Static Measurements

Static lift and drag measurements were taken independent of the measurements in section 2.2.1. Figure 3.3 shows the measured static lift and static drag obtained for angles of attack between 0° and 20°. Both the lift and the drag are similar to the static lift curve slope in Figures 2.5(a) and 2.5(b). The airfoil stalls at 10° AoA, and the linear part of the lift curve has a slope of 0.089 C_L/rad versus 0.093 C_L/rad as shown in Figure 2.5(a). The minor discrepancy might be due to human and systematic errors during the re-positioning process of the test rig as well as the possible difference in ambient pressure and temperature conditions at the time of the experiment. Both experimental values show discrepancy from $C_l = 2\pi\alpha$ that is expected for potential flow theory since potential flow theory only holds for an ideal fluid.

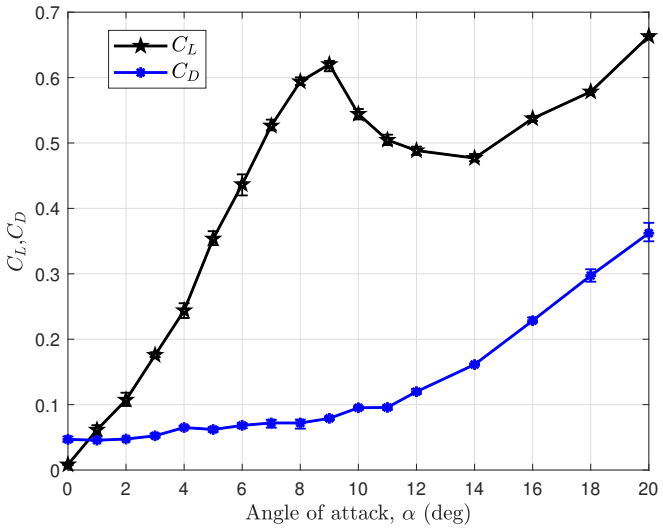

Figure 3.3: Static lift and drag measurements for a NACA-0012 at $Re = 2.1\text{x}10^4$

3.2.2 Dynamic Measurements

A periodic airfoil motion in a uniform freestream flow can generate unsteady flow dynamics such as leading edge vortex (LEV) formation, leading edge suction, vortex wake shedding, and dynamic stall characteristics [50, 118, 119]. The strength of an LEV can also vary with a change in airfoil acceleration (frequency) and a change in pitching mean angle of attack, which may lead to lift enhancements [38, 120]. A typical response for a quasi-steady flow following a simple harmonic airfoil motion will show a lift time history that will linearly rise and drop with an increased or decreased angle of attack, respectively. With the involvement of complex pitching kinematics, complicated vortex wake structures are expected to form and, thus, can generate lift and drag responses different from the ones developed by a sinusoidal input.

Representative snapshots of C_L time histories

Figure 3.4 shows the lift coefficient time history for one period of pitching motion for all four waveforms about a nominally attached flow at 3.5° mean AoA. Figures 3.4(a), 3.4(b) and 3.4(c) demonstrate the lift coefficients for the sub-test cases at reduced frequencies of $k = 0.02$, 0.05 and 0.09, respectively. Three horizontal lines in the plots are displayed to represent the quasi-steady values at the maximum and minimum reachable AoA during pitching, and mean AoA for a stationary airfoil. That is, the static C_L values at α_0=7°, α_0=0° and α_0=3.5°, respectively. A typical example of a smooth linear response is observed for the sinusoidal waveform in Figure 3.4(a), which shows that the lift generated in the dynamic pitching case increases up to a peak C_L value which is equivalent to the C_L value for a stationary airfoil at 7°. This lift behavior becomes uncommon at higher pitching frequencies where the dynamic peak is lift deficient relative to the quasi-steady C_L. The lift

response of the sine wave behaves almost linearly with the static C_L and confirms that the flow is quasi-steady at $k = 0.02$ and $k = 0.05$. The peak lift for the sinusoidal waveform experiences substantial lift deficiency at $k = 0.09$ and reveals that the flow can be regarded as unsteady at that operating frequency. According to Kirchhoff's law [121], the induced circulation around the airfoil is accounted for by the shedding of the wake vorticity. As such, the vortex shedding plays a significant contribution to the resultant lift circulation generated by the unsteady motion.

Out of the four waveforms, the kinematics associated with higher acceleration rates during the pitch-up motion of the airfoil are the trapezoidal and the reverse sawtooth waveforms. The response of the trapezoidal waveform can be characterized by its "shoulders" during the hold period of the airfoil. At that moment, the force undergoes variation in lift amplitude as a result of a sudden transition to a steady angle of attack. Similarly, the reverse sawtooth sees a lift transient response during the pitch-up motion. The time histories show the formation of a transient lift that surpasses the quasi-steady lift value. The characteristic of the airfoil motion represented by the trapezoidal and the reverse sawtooth waveforms is consistent with the large absolute values of instantaneous forces within the lift histories, with local lift transient responses pronounced at higher frequencies as depicted in Figures 3.4(b) and 3.4(c).

Figure 3.5 demonstrates one period of unsteady lift response undergoing pitching between a nominally attached flow and a lightly separated flow. Figures 3.5(a), 3.5(b) and 3.5(c) demonstrate the lift coefficients at reduced frequencies of $k = 0.02$, 0.05 and 0.09, respectively. Three horizontal lines in the plots represent the quasi-steady lift values at α_0=10.5°, α_0=3.5° and α_0= 7°. A stationary airfoil is typically stalled at an angle of attack of 10°; see Figure 3.3. At that AoA, the stationary airfoil generates a substantially lower lift coefficient than the lift generated by the pitch-up motion. The airfoil enters a nominally light stall

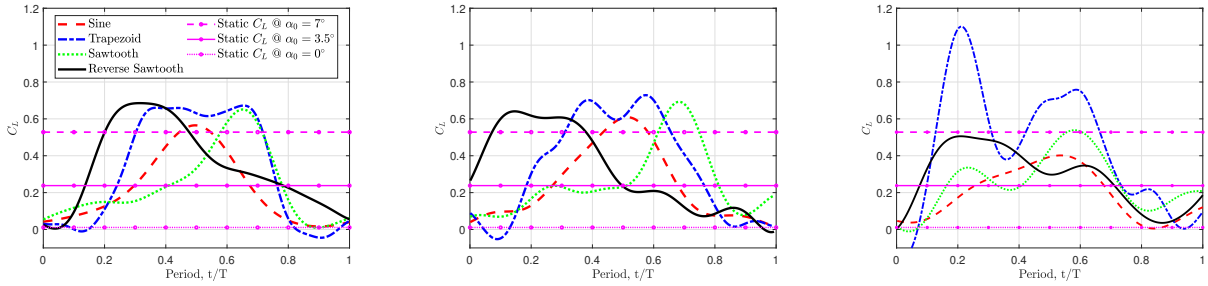

(a) $k = 0.02$ (b) k=0.05 (c) $k = 0.09$

Figure 3.4: Representative snapshots of time histories from experimental data for all four different pitching waveforms at $\alpha_0 = 3.5°$.

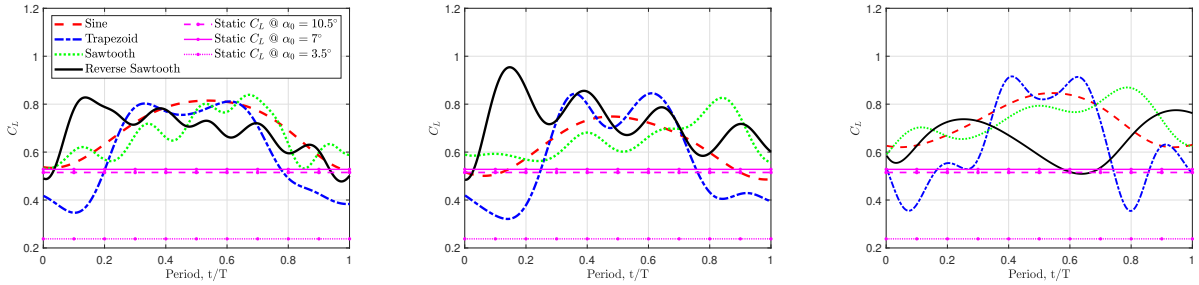

(a) k=0.02 (b) k=0.05 (c) k=0.09

Figure 3.5: Representative snapshots of time histories from experimental data for all four different pitching waveforms at $\alpha_0 = 7°$.

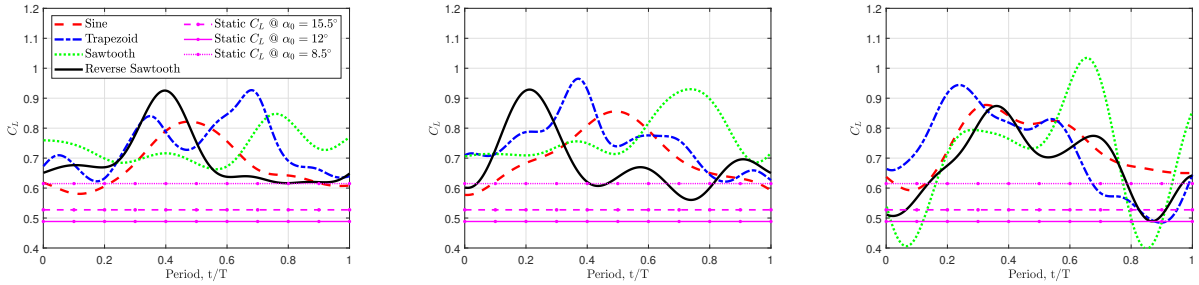

(a) $k = 0.02$ (b) k=0.05 (c) $k = 0.09$

Figure 3.6: Representative snapshots of time histories from experimental data for all four different pitching waveforms at $\alpha_0 = 12°$.

regime but continues to rise beyond the quasi-steady value at the same angle of attack. The lift also rises beyond the static stall AoA which suggests that flow separation is delayed.

Likewise, the lift coefficients at 3.5° and 7° for a stationary airfoil correspond to a lower lift than the lift responses generated by the pitch-up motion. Even during the pitch-down motion, the lift responses for all waveforms do not recover back to their corresponding quasi-steady value at $\alpha_0 = 3.5°$. To physically interpret the results, an increase in lift response beyond the quasi-steady value signals the creation of larger pressure differential during a dynamic stall event. In return, a net lift production following a pitch-up and pitch down motion becomes a net positive lift, i.e., lift enhancement. One final observation from these plots is that the instantaneous C_L values appear to be unaffected by the rate of the pitch up motion at all reduced frequencies since the instantaneous lift values for all waveforms are similar in value.

Figure 3.6 displays one period of aerodynamic response undergoing pitching about a nominally separated AoA of 12°. Figures 3.6(a), 3.6(b) and 3.6(c) demonstrate the lift coefficients at pitching reduced frequencies of $k = 0.02$, 0.05 and 0.09, respectively. Three horizontal lines in the plots represent the quasi-steady lift values at α_0=15°, α_0=8.5° and α_0= 12°. Instantaneous lift peaks are the largest for both impulse pitch-up motion (i.e. trapezoidal and reverse sawtooth) but also for the gradual build-up in motion from the sawtooth motion. A jump in C_L occurs at the discontinuities of a pitch-up airfoil motion. The trapezoidal waveform is by no surprise an outlier out of the tested waveforms in that it produces the largest lift values. The relatively gradual drop-off in the lift for the reverse sawtooth contrasts sharply with the sudden drop-off for the conventional sawtooth. This disparity may be due to the creation and retention of a leading edge vortex following the rapid transient in the reverse sawtooth input. Since most of the LEV formation occurs during the pitch-up of the airfoil, the sawtooth input, by contrast, is less likely to generate a stronger LEV because of the gradual build-up in the lift and the relatively low pitch-up rate.

A rapid pitch-up motion in post-stall conditions can lead to the formation of an LEV

[118, 122]. These trends in force measurements compare well with dye visualization results of Ol [123] on an SD7003 airfoil and a flat plate at $Re = 10^4$. Results show that a pitch-up motion to 25° of a trapezoidal waveform shows an emanating leading edge vortex at discontinuities of angle of attack rate. These discontinuities in the angle of attack do promote LEV shedding during the pitch-up. The strongest LEV was noticed for the trapezoidal pitching motion. Visualizations also qualitatively show that the case with the largest LEV also has the highest amplitude of the lift coefficient. The visualization results show a distinction for the trapezoidal pitch due to the double formation (one positive and one negative) of shed vortices per single stroke. Results from Ol [123] also reveal that the strength of the LEV is somewhat greater for the trapezoidal than for the sinusoidal and triangular waveforms as it forms near the top of the pitch-up stroke. The triangular waveform generated the weakest LEV, followed by the sinusoidal waveform.

C_L time histories against measured angle of attack

The lift and drag responses during the pitch-up and pitch-down motion of the airfoil for each waveform are shown in greater detail in Figures 3.7, 3.8, and 3.9. The force time histories are plotted against their corresponding measured airfoil position obtained from the potentiometer. The plots show the C_L time histories as a dashed blue curve, C_D time histories as a solid black curve, and airfoil angular position as a dotted red curve for all waveforms, as well as mean angles of attack and reduced frequencies. Since data was acquired from two different data acquisition systems, data was recorded for a stationary airfoil subjected to freestream flow for ten seconds after which the airfoil executes its pitching motion. The initiation of the airfoil motion is time-stamped along with the corresponding force reading recorded by the load cell. Any transient effects during the build-up of the motion as well as the build-up of the lift response towards steady-state are ignored. The unsteady linear

lift response is presented in these plots to observe the behavior of the flow dynamics in response to airfoil kinematics. As such, the cut-off frequency for the time series is set at three times the operating frequency except for the trapezoidal waveform, where a cut-off frequency of five times the operating frequency is used to capture the transient lift response at the discontinuities of the waveforms.

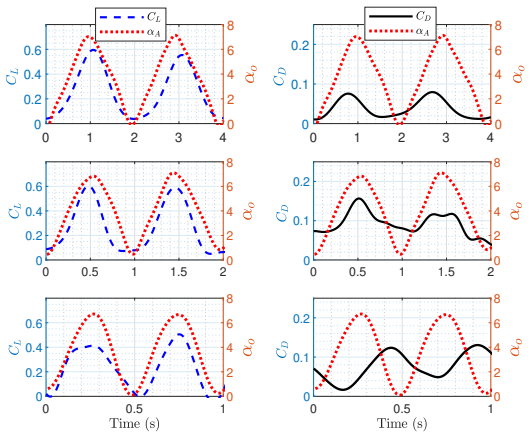

(a) Sine. (Top to bottom: $k = 0.02, 0.05, 0.09$. Left to right: C_L vs α, C_D vs α)

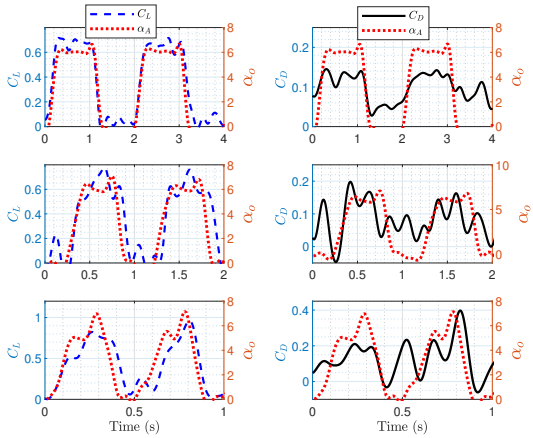

(b) trapezoidal. (Top to bottom: $k = 0.02, 0.05, 0.09$. Left to right: C_L vs α, C_D vs α)

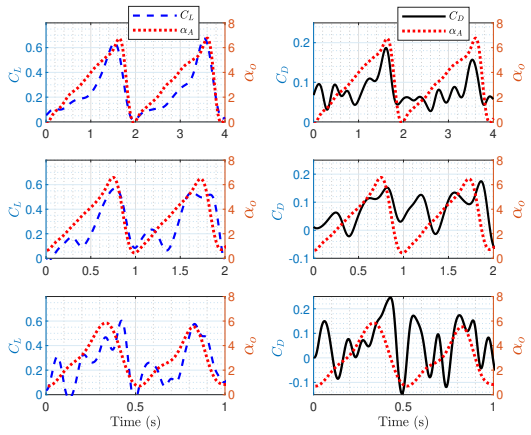

(c) Sawtooth. (Top to bottom: $k = 0.02, 0.05, 0.09$. Left to right: C_L vs α, C_D vs α)

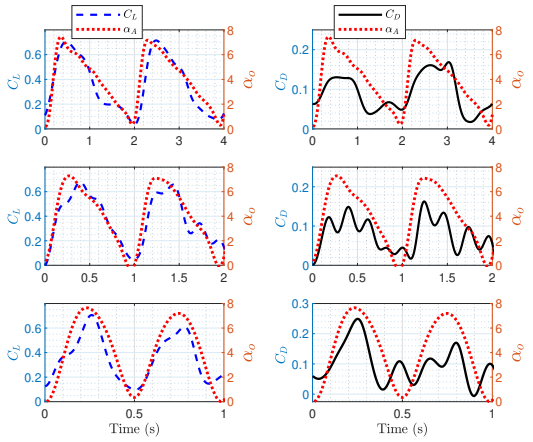

(d) Reverse sawtooth. (Top to bottom: $k = 0.02, 0.05, 0.09$. Left to right: C_L vs α, C_D vs α)

Figure 3.7: Case A - Lift coefficient time histories for all four waveform inputs against measured motion kinematics at $\alpha_0 = 3.5°$

While examining the C_L responses at $\alpha_0 = 3.5°$ in Figure 3.7, the responses at $k = 0.02$

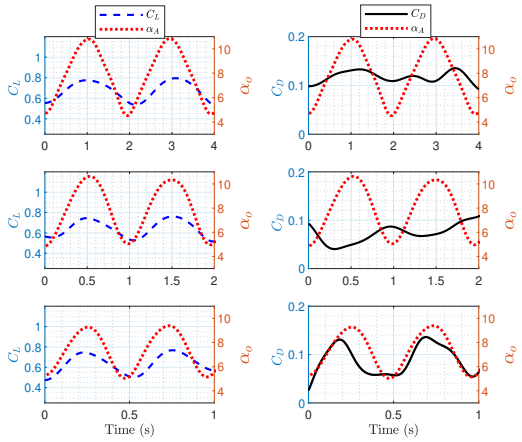

(a) Sine. (Top to bottom: $k = 0.02, 0.05, 0.09$. Left to right: C_L vs α, C_D vs α)

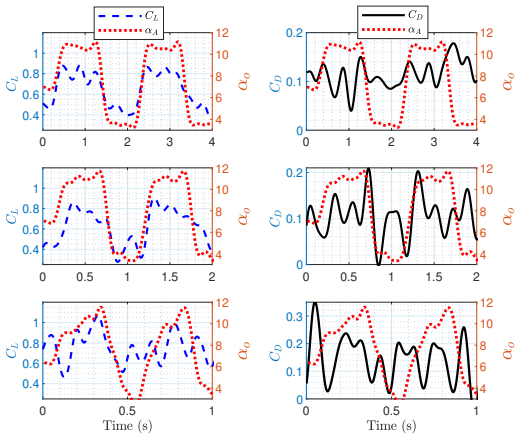

(b) trapezoidal. (Top to bottom: $k = 0.02, 0.05, 0.09$. Left to right: C_L vs α, C_D vs α)

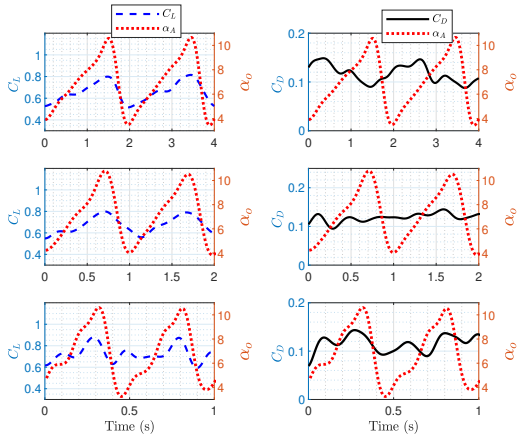

(c) Sawtooth. (Top to bottom: $k = 0.02, 0.05, 0.09$. Left to right: C_L vs α, C_D vs α)

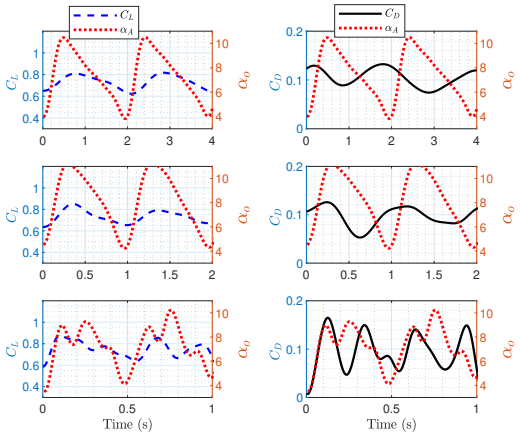

(d) Reverse Sawtooth (Top to bottom: $k = 0.02, 0.05, 0.09$. Left to right: C_L vs α, C_D vs α)

Figure 3.8: Case B - Lift coefficient time histories for all four waveform inputs against measured motion kinematics at $\alpha_0 = 7°$

is linear with the airfoil's kinematics. Some time lag in the lift build-up is evident for all waveforms at all reduced frequencies. For all waveforms, nearly all C_D build up responses are gradual and in-phase with the airfoil's motion. But while the responses for non-sinusoidal waveforms behave linearly with motion, larger superposition of non-linear perturbations on the signal is observed at all reduced frequencies. The drag coefficient at $k = 0.02$ for the sinusoidal waveform in Figure 3.7(a) responds out of phase with the airfoil motion. The

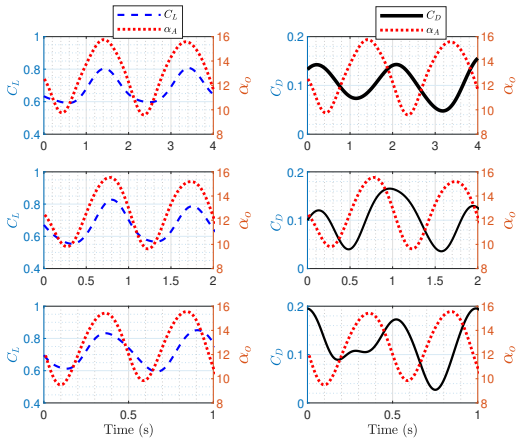

(a) Sine. (Top to bottom: $k = 0.02, 0.05, 0.09$. Left to right: C_L vs α, C_D vs α)

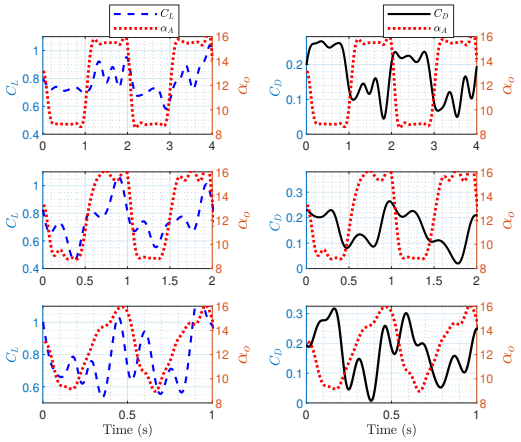

(b) trapezoidal. (Top to bottom: $k = 0.02, 0.05, 0.09$. Left to right: C_L vs α, C_D vs α)

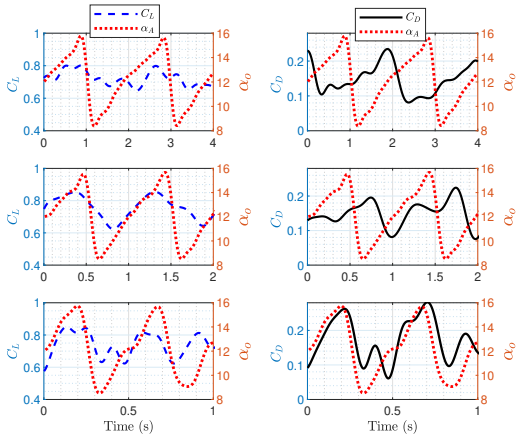

(c) Sawtooth. (Top to bottom: $k = 0.02, 0.05, 0.09$. Left to right: C_L vs α, C_D vs α)

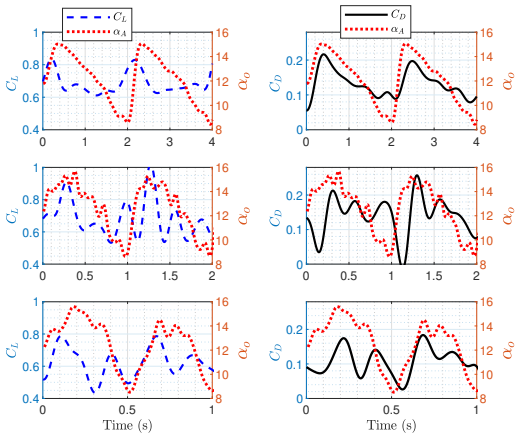

(d) Reverse sawtooth. (Top to bottom: $k = 0.02, 0.05, 0.09$. Left to right: C_L vs α, C_D vs α)

Figure 3.9: Case C - Lift coefficient time histories for all four waveform inputs against measured motion kinematics at $\alpha_0 = 12°$

pitch-up of the trapezoidal waveform generates the greatest lift but experiences greater drag too. Both aerodynamic load histories demonstrate smooth behavior up to the completion of the pitch up motion, and the same goes for all other waveforms at $k = 0.02$, and $k = 0.05$. For higher reduced frequencies, stronger non-linearities are manifested into the lift and drag responses. For the waveforms that are associated with an impulse pitch down motion (i.e., the trapezoidal and the sawtooth waveforms), the drag decreases beyond what it usually

would be in quasi-steady condition, and in some cases beyond $C_D = 0$, indicating a "positive thrust" for a short interval of time before rising steadily again. These short intervals of positive thrust are being formed again at the discontinuities at the end of the pitch-down motion. Examples of that flow behavior are distinguished in Figures 3.7(b) at $k = 0.05$ and $k = 0.09$ and in Figures 3.7(c) at $k = 0.05$ and $k = 0.09$.

Figure 3.8 presents similar C_L and C_D characteristics $\alpha_0 = 7°$ as the responses depicted in figure 3.7 for $\alpha_0 = 3.5°$. Responses in Figure 3.8(a) are linear with the airfoil's motion for all test cases. Non-linear fluctuations are presented at a higher reduced frequency and responses are generally in-phase with the airfoil motion with the exception of C_D at $k = 0.02$. C_L responses for the remaining non-sinusoidal waveforms show notable phase lag in the lift build-up for the trapezoidal waveform compared to the sawtooth and reverse sawtooth waveforms. Substantial non-linear fluctuations are fostered in the C_D responses for non-sinusoidal waveforms. As for the waveforms with impulse pitch-down motions, only the trapezoidal waveform at higher reduced frequencies responded with C_D peaks close to zero. Even though the sawtooth waveform presented some negative drag during the pitch-down motion at $\alpha_0 = 3.5°$, it does not exhibit similar behavior in C_D as seen in the trapezoidal waveform at $\alpha_0 = 7°$.

Figure 3.9(a) shows C_L responses that are in-phase and almost linear with the airfoil's kinematics at $\alpha_0 = 12°$. C_L responses that are slightly out of phase with the airfoil's kinematics also exhibit strong non-linear fluctuations in lift responses as seen at $k = 0.09$ in Figure 3.9(c) and at all frequencies in Figure 3.9(c). The C_D response for the sine waveform shows as a significant out-of-phase response, and the trapezoidal waveform clearly shows nearly a 180° phase shift in response relative to the motion for all frequencies. Out of phase responses at higher reduced frequencies diminish for a sawtooth waveform, whereas the C_D responses for a reverse sawtooth provided an in-phase response with the airfoil motion. No

significant reduction in drag during any of the pitch-down motions was noted, although it appears that the sinusoidal waveform generates the least drag force in post-stall oscillations compared to the non-sinusoidal waveforms.

In summary, a slower pitch-down airfoil motion generates excessive drag, whereas rapid pitch-down rates (impulse motion) incurred by the airfoil during the trapezoidal and the sawtooth waveforms create the least drag, and in some instances negative drag (thrust) although it does not sustain throughout the periodic motion. The behavior is pronounced at lower mean angles of attack where the flow is fully attached. The trends in force generation depicted in Figures 3.7, 3.8, and 3.9 show time histories during pitch-up and pitch-down motions that are consistent with the observed vortex shedding dye-visualization results reported by Ol et al. [49]. After matching these results with the current study, the LEV formed contributes significantly to the lift. LEV is generally associated with an upstroke motion of the airfoil.

Additionally, vorticity fields reported by Eldredge et al. [51] show that during the pitch-up motion, the LEV is large and remains attached at $k = 0.2$ but begins to detach and diffuse away during the pitch down motion. At higher pitch-up rates, the leading edge vortex is more coherent and larger in radius. The detachment during the downstroke motion is further delayed. This behavior appears to show that upward lift generation during the pitch-up motion is enough to overcome the downward lift during the pitch-down motion, and a net positive lift around the airfoil is created. The likelihood of a dynamic stall taking place depends on the formation of LEV, and the roll-up of LEV impinging on the airfoil as a pitch-down motion is initiated. In our current study, a rapid pitch-up motion is presented by both the trapezoidal and the reverse sawtooth waveforms. Thus, a more significant lift is generated for these waveforms as a result of the creation and retention of a LEV that would delay separation and increase lift. In contrast, the sinusoidal and sawtooth waveforms are associated with a slower pitch-up motion. Therefore, dynamic stall events may

be more gradual, mitigating any possibilities of delaying flow separation, which is why the lift responses associated with these two waveforms are generally lower than the trapezoidal and the reverse sawtooth waveforms.

Mean C_L and C_D results

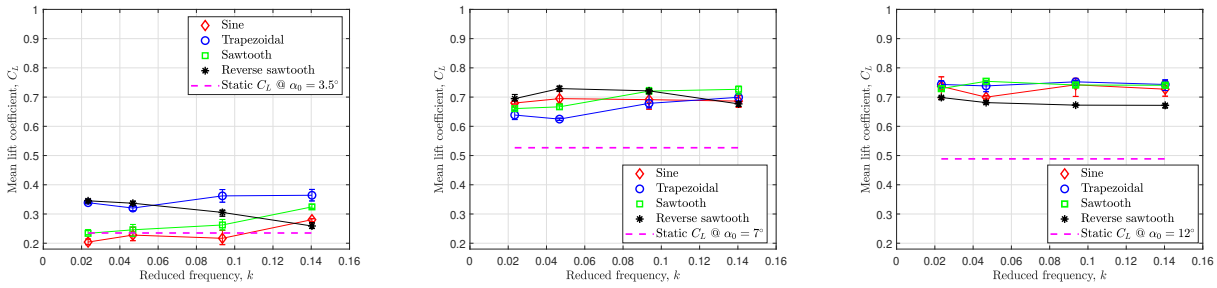

(a) $\alpha_0 = 3.5°$ (b) $\alpha_0 = 7°$ (c) $\alpha_0 = 12°$

Figure 3.10: Time averaged C_L vs Reduced frequency for all mean AoA

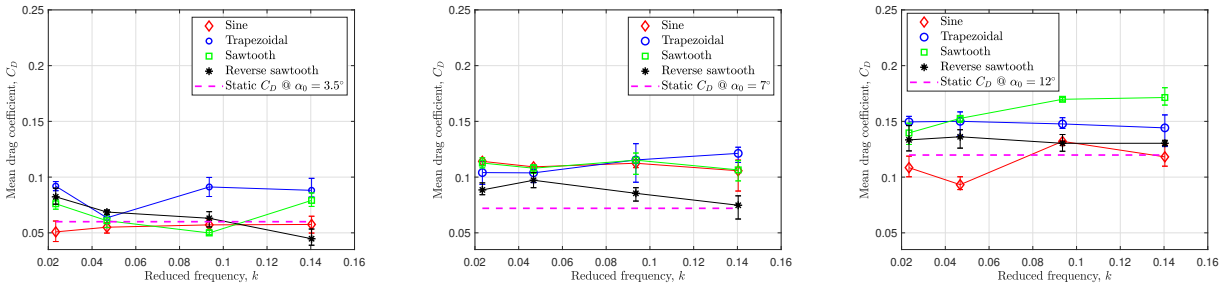

(a) $\alpha_0 = 3.5°$ (b) $\alpha_0 = 7°$ (c) $\alpha_0 = 12°$

Figure 3.11: Time averaged C_D vs Reduced frequency for all mean AoA

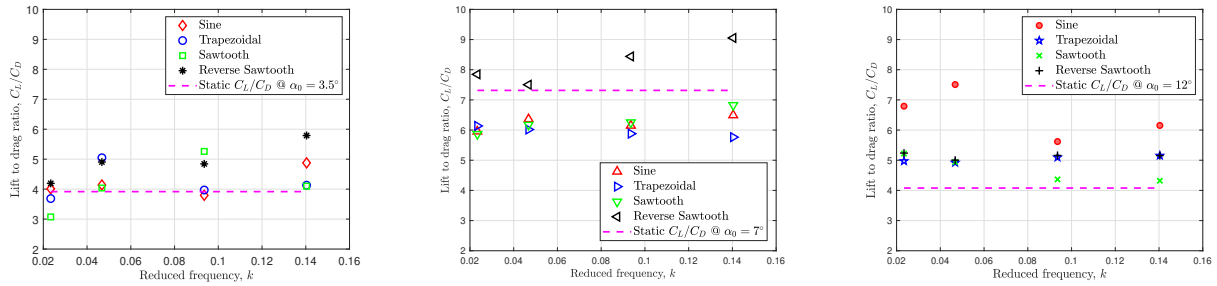

(a) $\alpha_0 = 3.5°$ (b) $\alpha_0 = 7°$ (c) $\alpha_0 = 12°$

Figure 3.12: Time averaged C_L/C_D vs Reduced frequency for all mean AoA

The force generation shown in the time history plots can be better understood by examining the mean lift and drag. In this section, mean results for C_L, C_D, and lift to drag ratios,

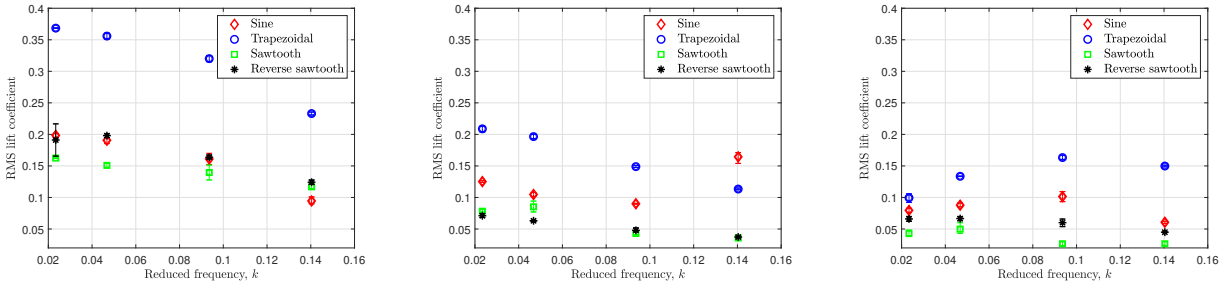

(a) $\alpha_0 = 3.5°$ (b) $\alpha_0 = 7°$ (c) $\alpha_0 = 12°$

Figure 3.13: *RMS* C_L vs reduced frequency for all mean AoA

C_L/C_D are presented. Data for $k = 0.14$ are also included in the analysis to provide a reasonable statistical comparison with the lower tested frequencies.

Figures 3.10 and 3.11 show the effects of reduced frequencies and mean angles of attack on the mean lift and drag coefficients for all pitching waveforms. In a nominally fully attached flow at 3.5°, the trapezoidal and the reverse sawtooth waveforms generated the most significant mean lift coefficients but also generated the largest drag coefficients. At 7° AoA, we can observe that the reverse sawtooth waveform consistently produces a marginally higher mean lift than other waveforms except at k=0.14. The reverse sawtooth waveform also provides the least drag coefficient at all reduced frequencies. In post-stall oscillations at 12°, the trapezoidal and the sawtooth waveforms generate the most significant mean lift coefficients. No definite conclusion was drawn on how the mean drag varies with reduced frequency. While comparing all dynamic results with static results, the trapezoidal and the reverse sawtooth also saw the most significant rise in mean C_L values relative to their corresponding quasi-steady value at $\alpha_0 = 3.5°$. The mean C_L generated by the reverse sawtooth waveform monotonically decreases with increasing frequency consistently across all mean angles of attack, in contrast to the behavior seen by the remaining three waveforms. Among all mean angles of attack, all pitching waveforms generate a more significant dynamic mean C_L relative to the static C_L for a stationary airfoil at $\alpha_0 = 7°$ and $\alpha_0 = 12°$. Comparing the dynamic

mean C_D with static C_D, all waveforms across all mean angles of attack produce larger dynamic mean drag coefficients relative to their corresponding quasi-steady drag coefficient. The only exceptions appear for the sinusoidal waveform at 3.5° AoA, and at lower reduced frequency at 12° AoA with lower dynamic drag coefficients than their corresponding quasi-steady C_D. Consequently, the sinusoidal waveform differs from the other waveforms as it produces a net thrust to overcome the static drag. Force-time histories in Figure 3.7 show that the sawtooth, which is associated with an impulse pitch-down motion, produces thrust at short intervals of time. However, the flow is not able to sustain that for enough time to create a net positive thrust for the tested frequencies.

The overall aerodynamic performance for each waveform is quantified by computing the lift-to-drag ratios. The lift-to-drag ratios for all dynamic test cases are determined and presented in Figure 3.11. The dynamic lift-to-drag ratio is compared directly with the lift-to-drag ratio at the corresponding static mean AoA. For pitching about $\alpha_0 = 3.5°$, higher lift-to-drag ratios are observed at higher reduced frequencies. The combination of an impulse pitch up and a gradual pitch down airfoil motion represented by the reverse sawtooth waveform gives rise to the highest lift-to-drag ratio at pitching about 3.5° and 7° mean AoAs. For pitching about 12° mean AOA, the sinusoidal waveform produces the highest lift-to-drag ratios. Table 3.2 summarizes the performance of some of the outliers in the results from Figures 3.10, 3.11 and 3.12.

The root mean square (RMS) value for each force-time history is computed and presented in Figure 3.13 for all test cases. The RMS value is a way to represent the magnitude of the unsteady lift generated. The RMS of a signal is calculated using the standard RMS definition:

Table 3.2: Dynamic lift vs quasi-steady values quantified

Mean AoA	**Most significant rise in C_L**	**Most significant drop in C_D**	**Most significant rise in C_L/C_D**
3.5°	50% by the trapezoidal at k=0.09 and 0.14	25% by the reverse sawtooth at k=0.14	25% by reverse sawtooth at k=0.14
7°	Not noticeable	None. But the least drag reduction occurred for reverse sawtooth at k=0.14	24% by the reverse sawtooth at k=0.14
12°	Not noticeable. But the reverse sawtooth consistently generated the lowest mean C_L	22% by the sinusoidal at k=0.05	83% by the sinusoidal at k=0.05

$$u_{RMS} = \sqrt{\frac{1}{T}\int_0^T u(t)^2 dt} \tag{3.1}$$

where $u(t)$ is the function of the signal, and T is the period. For the sinusoidal waveform, the *RMS* is approximately $1/\sqrt{2}$ times the signal's (force-time history) peak amplitude. The *RMS* value for the trapezoidal waveform is approximately $\sqrt{0.733}$ times the signal's peak amplitude [124], and the *RMS* value for the sawtooth/reverse sawtooth waveforms is approximately $1/\sqrt{3}$ times the signal's peak amplitude [125]. The frequency content of the force-time history for each waveform is evaluated using the power spectral density (PSD) analysis to determine the peak C_L values for each signal. The trapezoidal waveform at all mean angles of attack generates the most substantial *RMS* C_L values relative to the other waveforms. Since the kinematics of the trapezoidal waveform has a prolonged period of 'hold' position, it can produce higher and sustained lift force. Lift response of the reverse sawtooth waveform generates the second-largest *RMS* lift, but only in a fully attached flow. Beyond 3.5° AoA, the *RMS* lift value produced by the sinusoidal waveform surpasses the *RMS* lift produced by the reverse sawtooth waveform at higher mean angles of attack. Among all mean angles of attack, the generated *RMS* lift coefficient is the greatest in a fully attached flow condition at $\alpha_0 = 3.5°$.

Power Spectra Analysis

The contribution of the linear and non-linear lift responses to the total generated lift is explored through the power spectral density (PSD). A digital fourth-order Butterworth low-pass filter is used to smooth the data with a cut-off frequency of at least three times the operating frequency for all waveforms, except for the trapezoidal waveform where a cut-off frequency of five times the operating frequency is used. The cut-off frequency was selected to capture at least non-linearities in the response up to the second harmonic (five times the fundamental frequency) and to filter out any structural interference from the experimental setup. Although the structure naturally oscillates at nearly six times the highest operating frequency (18 Hz) for this experimental program, the second harmonic of the aerodynamic response is reasonably far from the test rig's natural frequency.

Figure 3.14 shows the PSD for all test cases and sub-test cases. The frequency content for each test case is determined by the fast Fourier transform of the periodic time series. The frequency content displays a linear response in C_L at the driving frequencies. Non-linear responses are also demonstrated by signal content at two and three times the fundamental frequencies. In all sub-figures, the trapezoidal waveform generates the largest lift amplitude for the same actuation frequency and pitching amplitude inputs relative to other waveforms. An important observation to note from these plots is that the PSD peak values monotonically decrease with an increasing mean angle of attack and frequency of oscillation. The only exception is displayed in the results for the mean angle of attack of 12°, where the peak values monotonically increase with increasing frequency of oscillation.

Figure 3.15 shows the lift amplitude coefficients for all reduced frequencies and pitching about mean angles of attack of 3.5°, 7°, and 12°. The peak values of the power spectra can be translated to a physical meaning, (i.e., the unsteady C_L amplitude) by taking the square

root of twice the PSD peak value. The peak values of the linear response are presented as C_L amplitude in Figure 3.15.

A reasonable assumption to make is to consider the response of the power spectrum's primary component as the unsteady linear lift amplitude. But the non-linearities that are manifested in the signal from the first and second harmonics can be statistically significant relative to the primary component. Figure 3.16 presents a close-up plot of the frequency content for a 0.5 Hz frequency driven system. The PSD analysis shows that the system generates most of its energy at the primary input frequency of 0.5 Hz. The system also responds in cascades of harmonics at two and three times the input frequency as a result of non-linear responses. Considerable harmonics are present when their corresponding linear lift responses are significant. What this means is that the total lift coefficient is generated as a superimposition of primary and non-primary frequency content. The peaks that appear at the harmonics show that non-linear C_L response is large relative to the linear C_L response, and indeed, does contribute significantly to the total lift production.

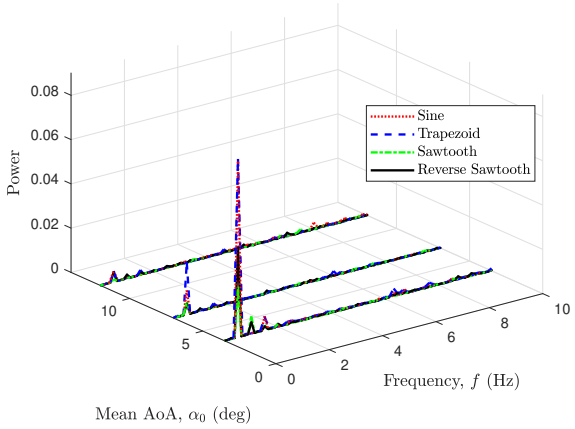

(a) Oscillations at 0.5 Hz, (k=0.02)

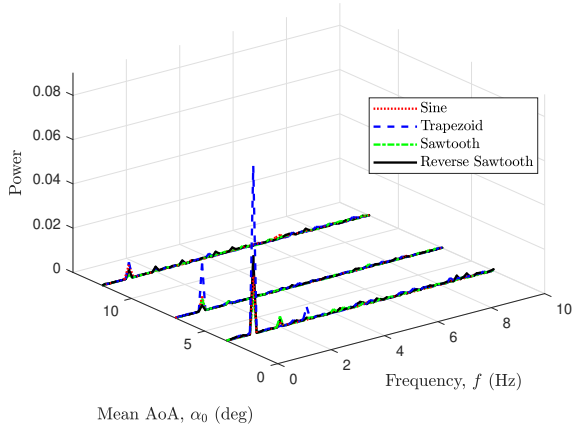

(b) Oscillations at 1 Hz, (k=0.05)

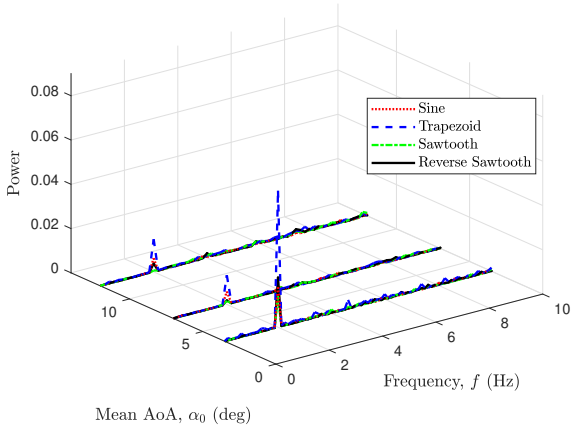

(c) Oscillations at 2 Hz, (k=0.09)

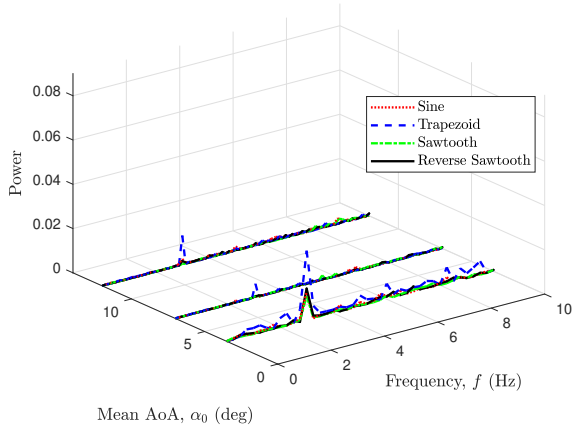

(d) Oscillations at 3 Hz, (k=0.14)

Figure 3.14: Power spectrum for all waveforms at $\alpha_0 = 3.5°$ for 0.5 Hz to 3 Hz airfoil pitching

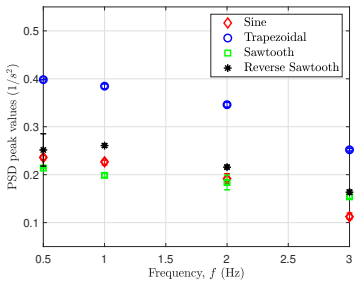

(a) $\alpha_0 = 3.5°$

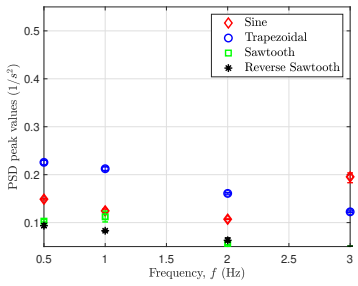

(b) $\alpha_0 = 7°$

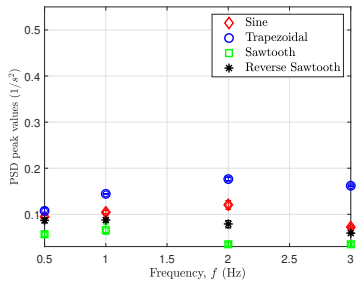

(c) $\alpha_0 = 12°$

Figure 3.15: C_L peak values from PSD analysis at primary oscillatory frequency

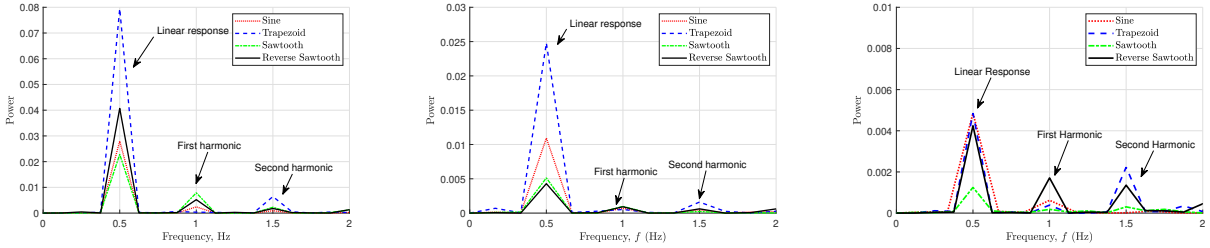

(a) $\alpha_0 = 3.5°$, $k = 0.02$ (b) $\alpha_0 = 7°$, $k = 0.02$ (c) $\alpha_0 = 12°$, $k = 0.02$

Figure 3.16: Power spectrum comparison across all waveforms and mean angles of attack at $k = 0.02$

Figure 3.17 shows the contribution of non-linear effects from first and second harmonics relative to the linear unsteady lift for a handful of frequency inputs at all three mean angles of attack. The superposition of C_L responses from the harmonics onto the linear response adds up to approximately the total lift amplitude generated. The results are consistent with the force-time histories in that the trapezoidal motion causes the largest lift amplitude. The reverse sawtooth also produces larger lift amplitudes compared to the sinusoidal and sawtooth waveforms for all reduced frequencies. The ratios of the lift responses at the harmonics relative to the response at the fundamental frequency are apparent at the post-stall angle of attack oscillations for all waveforms. Among all waveforms, Figures 3.17(a) and 3.17(b) show that the trapezoidal waveform gives rise to substantial second harmonic effects. Figures 3.17(c), 3.17(d), 3.17(e) and 3.17(f) demonstrate significant contribution of the lift response due to first and second harmonics generated by the reverse sawtooth waveform. Although the linear response in C_L for the sawtooth waveform is comparatively lower than other waveforms, it is the contribution of non-linear C_L response that results in a surge in the total lift amplitude.

In summary, the effects of harmonics contribute significantly to the overall unsteady lift amplitude for both the trapezoidal and the reverse sawtooth waveforms. The trapezoidal and reverse sawtooth are both associated with the highest pitch-up rates. Most of the lift

enhancement generated by these two waveforms is attributable to the harmonics and are pronounced with increasing AoA. Additionally, the ratio of first and second harmonic peaks relative to the fundamental peak at the driving frequency increases at higher angles of attack, and represent evidence of non-linearity.

Computational work by Eldredge et al. [51] confirms the presence of residual effects in the vorticity fields as a result of leading and trailing edge vortex shedding. These physical attributes can have a significant impact on force generation as well as on the time history responses of the aerodynamic loads. As such, non-linearity in the flow arise from these lift and drag force residuals in the flow measurements.

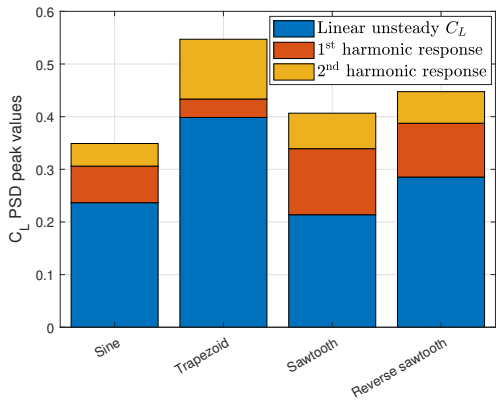

(a) $\alpha_0 = 3.5°$, $k = 0.02$

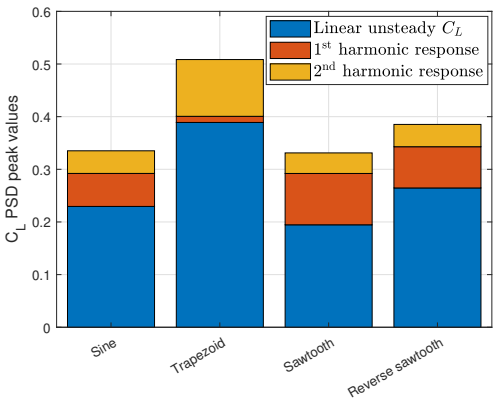

(b) $\alpha_0 = 3.5°$, $k = 0.05$

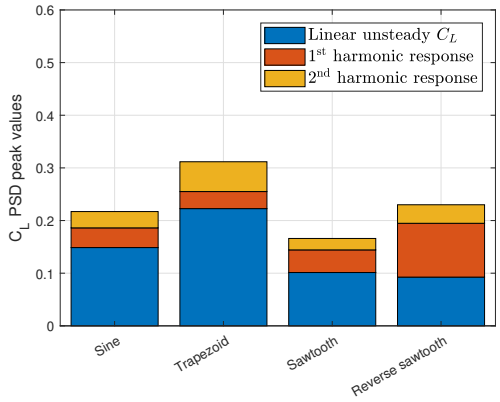

(c) $\alpha_0 = 7°$, $k = 0.02$

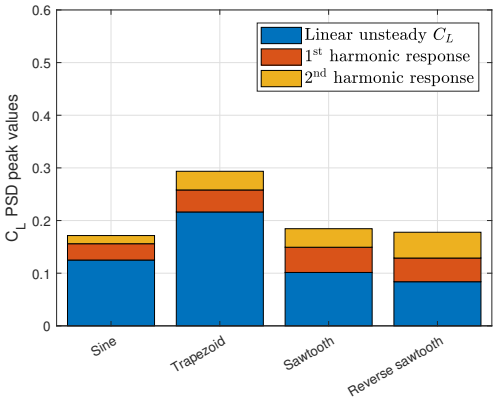

(d) $\alpha_0 = 7°$, $k = 0.05$

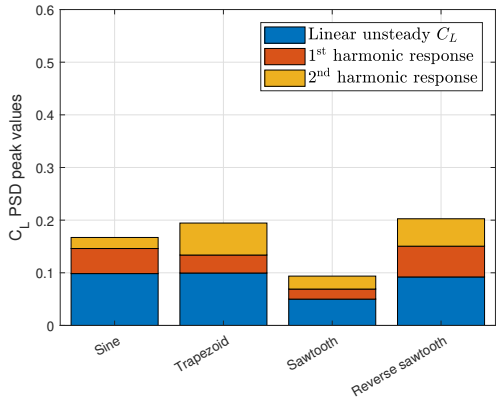

(e) $\alpha_0 = 12°$, $k = 0.02$

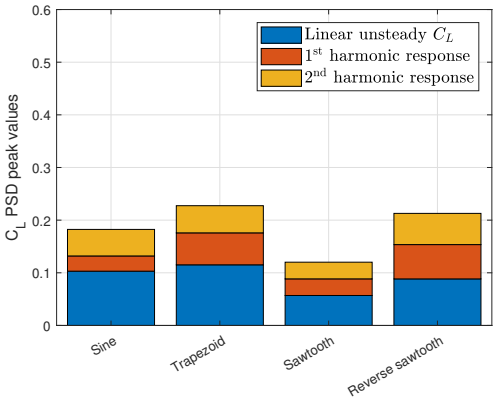

(f) $\alpha_0 = 12°$, $k = 0.05$

Figure 3.17: Primary, 1st, and 2nd harmonic responses summarized.

Validation with the unsteady state-space model

A state-space representation developed by Taha (2014) [117] is used to compare and validate the unsteady aerodynamic lift responses obtained experimentally. The state-space model is a physics-based model that is represented by ordinary differential equations and is able to capture certain physical aspects associated with the aerodynamics of arbitrary wing motion. Such physical aspects include translation and rotational lift, added mass forces, and dominant LEV contribution if there are any.

Two parameters determined from the experiments are incorporated into the state-space formulation. The first parameter is the slope of the static lift curve. The second parameter is the experimental α obtained from the potentiometer readings for each waveform as well as their derivatives, $\dot{\alpha}$, and $\ddot{\alpha}$. With these two experimentally determined parameters, the quasi-steady circulation is obtained. The quasi-steady circulation is used as the aerodynamic forcing input rather than the prescribed angle of attack. Using the measured angle of attack, the state-space model can provide predictions of the lift circulation as the sum of rotating circulation (as a function of $\dot{\alpha}$ using potential flow formulation), and translation circulation as determined by the expression $2\pi\alpha_{\text{eff}}$ where 2π is the slope of the static lift coefficient curve, and α_{eff} is the effective angle of attack. The first and second-time derivatives of the measured angle of attack are obtained using the first and second-order central finite approximation with Δt= 0.01. In addition to the state-space model, a classical unsteady aerodynamic model (Theodorsen's model [3]) is also used for comparison and validation of the sinusoidal waveform. The current form of Theodorsen's model does not apply to arbitrary pitching motion as it analytically predicts lift in the frequency domain. Theodorsen's model is also tailored to accommodate the lift curve slope into its formulation but uses the prescribed waveform instead of the measured angle of attack. Both Theodorsen's and state-space formulations utilized in the validation analysis are presented in Appendix A.

Figures 5.17(c), 5.15(c), and 3.18(e) compare results from Theodorsen's model and state-space with experimental data for the sinusoidal waveform at $\alpha_0 = 3.5°$ and reduced frequencies of $k = 0.02$, 0.05 and 0.09. At low reduced frequency, the lift response predicted by Thoedorsen's and state-space models agrees well with the lift response from experimental measurements. At higher reduced frequencies, both state-space and Theodersen's models overpredict the measured forces. The disparity between the experiment and both models may be due to viscous and transition effects for low Reynolds number flow that cannot be predicted. The ability to incorporate the experimental angle of attack readings makes the state-space model slightly more rigorous than Theodorsen's model in terms of predicting the lift amplitudes.

Figures 5.17(b), 5.15(d), and 3.18(f) show the unsteady effects captured by the state-space models for the trapezoidal pitching at $\alpha_0 = 3.5°$ and reduced frequencies of $k = 0.02$, 0.05 and 0.09. Comparisons between the state-space model and experimental results reveal the under-prediction of the lift force by the state-space model. As observed in Figure 5.17(b), there is a slight under-prediction in the absolute lift value. The reason for this lies in the assumption of using the lift curve slope to compute the quasi-steady circulation. During the impulse pitch-up motion in the trapezoidal waveform, a lift build-up in conjunction with the high regions of motion acceleration appears to be dictated by added mass effect. Despite the flow being at low Reynolds number, viscous effects do not even have enough time to contribute to the overall force production. Large instantaneous added mass forces due to high acceleration rates are responsible for the surge in lift transient at the end of the pitch-up motion, which are already accounted in the potential flow theory formulation of added mass in the state-space model. As such, the state-space model can predict the trend of the lift response generated by the trapezoidal waveform reasonably well.

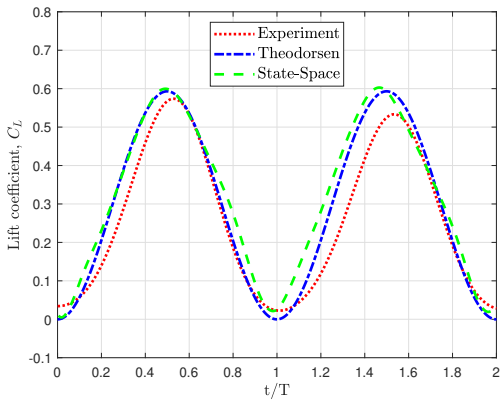

(a) k =0.02, Sine

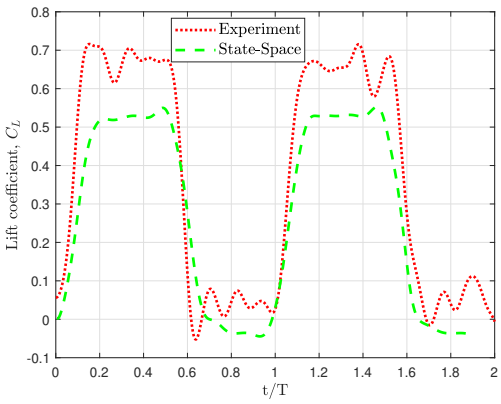

(b) k =0.02, trapezoidal

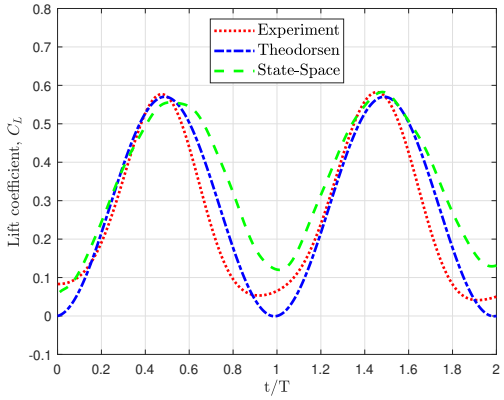

(c) k =0.05, Sine

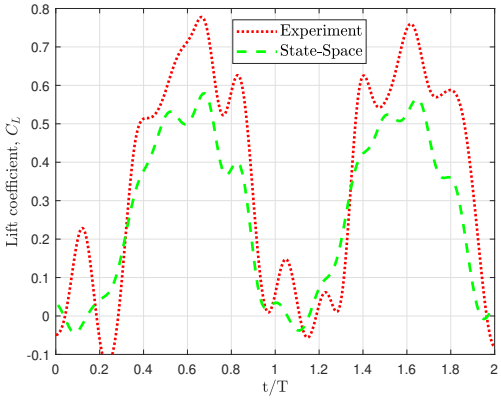

(d) k =0.05, trapezoidal

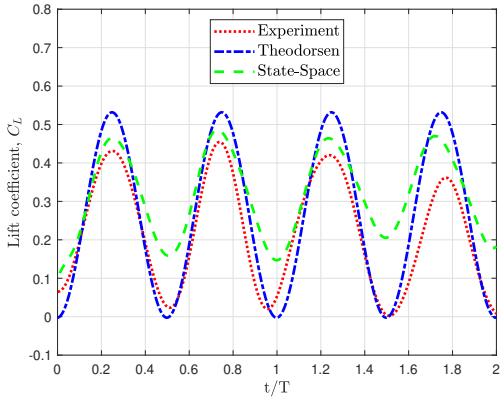

(e) k =0.09, Sine

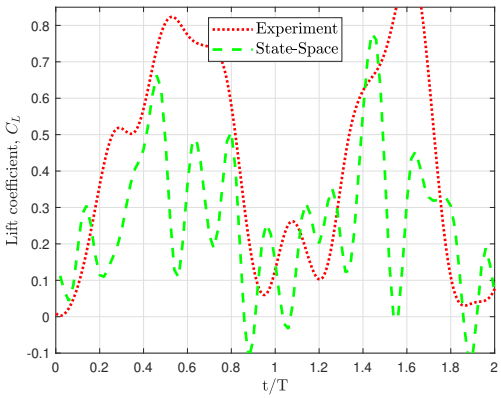

(f) k =0.09, trapezoidal

Figure 3.18: Sine vs trapezoidal at $\alpha_0 = 3.5°$

Figure 3.19 shows the unsteady effects captured by the state-space models for both the saw-

tooth and reverse sawtooth pitching at $\alpha_0 = 3.5^\circ$ and reduced frequencies of $k = 0.02$, 0.05 and 0.09. The state-space captures general trends in the lift response accurately when compared directly to the experimental results for nearly all frequencies. Only minor discrepancies are presented at instances with high acceleration rates.

In summary comparison made between experimental results and the model reported inconsistent transient lift response during high angle of attack rates. Overall, the lift amplitudes are well captured using the quasi-steady circulation assumption, and the state-space model predicts general trends in the lift response generated by all waveforms in an attached flow very well.

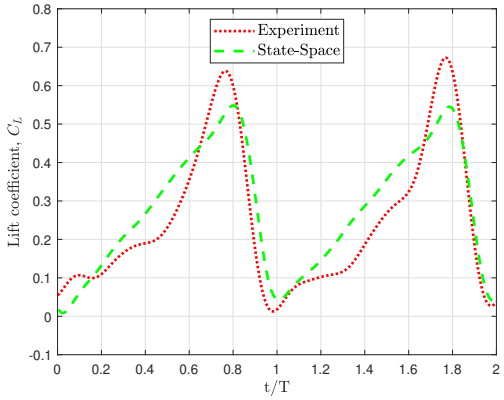

(a) k =0.02, Sawtooth

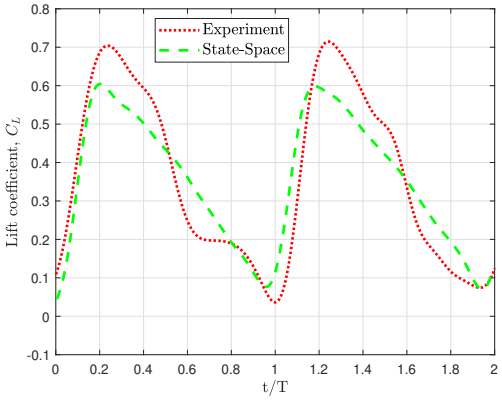

(b) k =0.02, Reverse Sawtooth

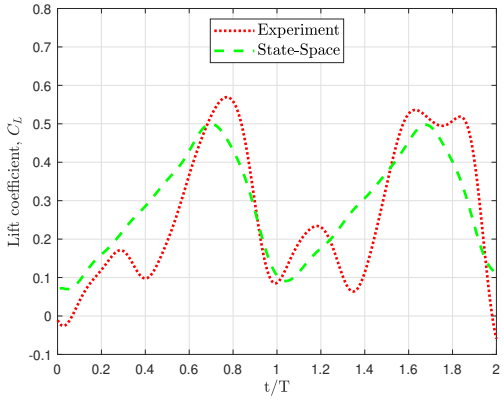

(c) k =0.05, Sawtooth

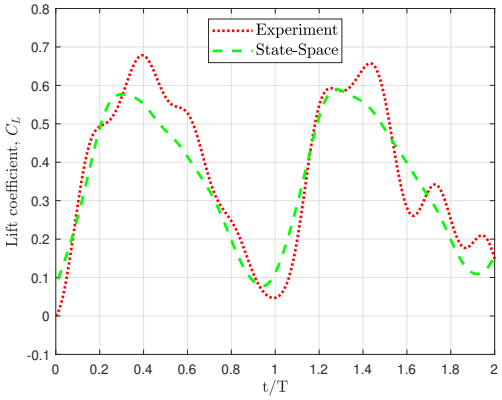

(d) k =0.05, Reverse Sawtooth

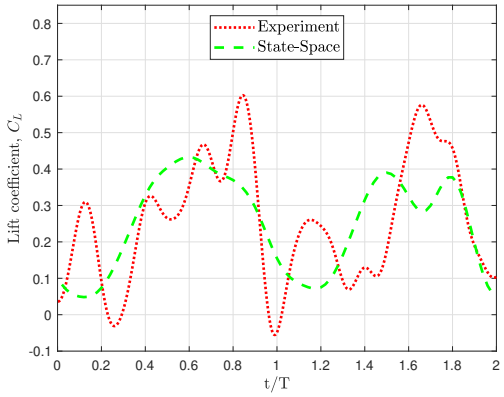

(e) k =0.09, Sawtooth

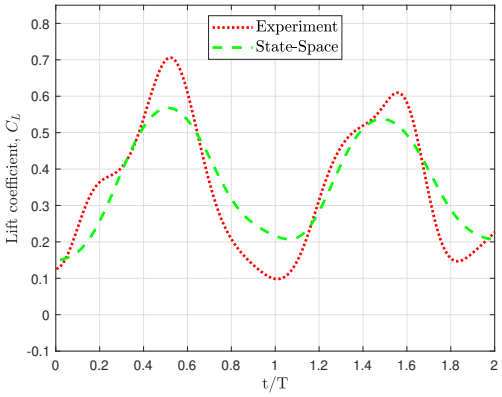

(f) k =0.09, Reverse Sawtooth

Figure 3.19: Sawtooth vs reverse sawtooth at $\alpha_0 = 3.5°$

The state-space model can be applicable for unsteady motions at higher angles of attack.

Figure 3.20 shows the response of the four waveforms pitching about $\alpha_0 = 7°$. The state-space model provides a reliable approach to predict the modulation in lift response due to both sinusoidal and non-sinusoidal motion. The results provided by the state-space model justify the importance of utilizing the state-space model to capture unsteady effects at high angles of attack for waveforms other than sinusoidal.

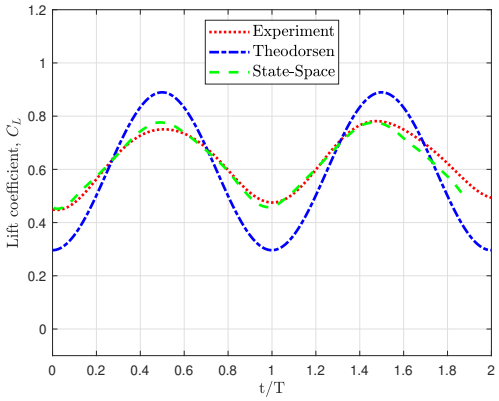

(a) k =0.02, sinusoidal (Includes results from Theodorsen's model)

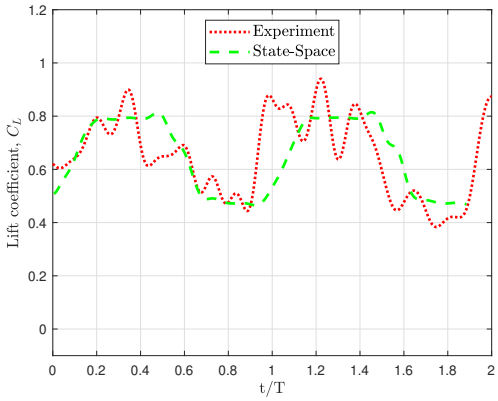

(b) k =0.02, trapezoidal

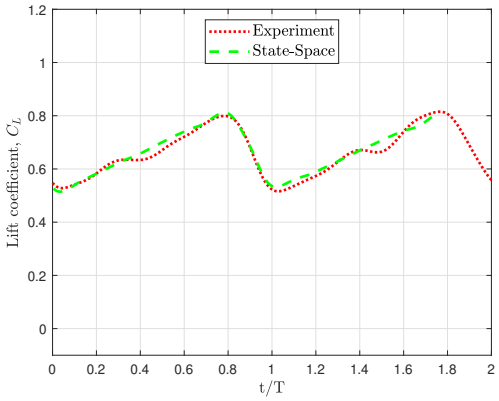

(c) k =0.02, sawtooth

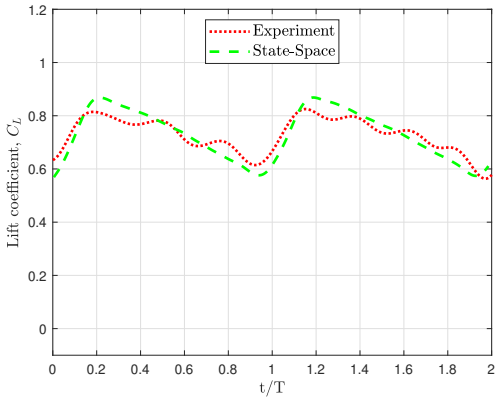

(d) k =0.02, reverse sawtooth

Figure 3.20: Experimental versus lift results from the state-space model at $\alpha_0 = 7°$

3.3 Summary of Contributions

In this study, we explore the force production as a result of sinusoidal and non-sinusoidal pitching motions of a NACA-0012. The periodic frequency and mean angles of attack were varied systematically to assess the lift and drag responses in a nominally attached flow, incipient stalled flow, and incipient post-stalled flow conditions. The unsteady aerodynamic responses are assessed at reduced frequencies between 0.02 to 0.14, at mean angles of attack of $3.5°, 7°$ and $12°$, and a pitching amplitude of $3.5°$. The kinematics considered are the sinusoidal, trapezoidal, sawtooth, and reverse sawtooth waveforms. The discontinuities in acceleration in the trapeoidal, sawtooth and reverse sawtooth waveform generated lift and drag responses with significant departure from the responses generated by the sinusoidal pitching motion.

Lift and drag responses

In a fully attached flow at mean AoA of $3.5°$, the results show that the trapezoidal followed by the reverse sawtooth waveforms achieve the largest lift amplitude relative to the sinusoidal and sawtooth. Both the trapezoidal and the reverse sawtooth are associated with higher pitch-up motion rates, which are responsible for generating lift on the suction side of the airfoil. Impulse pitch-up motions produced lift transients that exceed the quasi-steady value. Both sawtooth and the sinusoidal waveforms provided peak lifts that are deficient from the quasi-steady value. Lift enhancement in the generated mean lift was observed for all waveforms except for the sinusoidal and sawtooth waveforms at lower reduced frequencies where the flow can be categorized as quasi-steady. At mean AoA of $7°$, the lift time histories show that lift responses during pitch-up motion generated lift. Drag time histories in cases for sawtooth and sine wave showed excessive drag generation during a gradual pitch-down

motion. Impulse pitch-down motion by the trapezoidal and the sawtooth generated instances of negative drag (thrust) but for a short period. All waveforms generated a net positive mean lift but also produced a net positive drag force. The dynamic lift-to-drag ratios are the largest at this mean angle of attack when compared with lift-to-drag ratios at 3.5° and 12°. Only the reverse sawtooth waveform generated lift-to-drag ratio values beyond the quasi-steady lift-to-drag ratio. At mean AoA of 12°, An impulse upstroke motion of the airfoil generated a transient lift response that compliments a large lift force amplitude where most of the LEV's strength is created. Drag time histories show, for some cases, excess drag production during slow pitch-down motions. All four waveforms observed lift enhancement in both the lift amplitude and the generated mean lift. Additionally, all waveforms did generate larger lift-to-drag ratios beyond the quasi-steady lift-to-drag ratio. The most significant increase in the lift-to-drag ratio relative to its quasi-steady counterpart was observed by the sinusoidal waveform at k=0.05. During a gradual pitch-up motion, the lift and drag both steadily increase. During the reciprocating gradual pitch-down motion, a slow rate generates lower lift and drag, but sustained both lift and drag relative to the quasi-steady lift and drag for a given angle of attack. Only airfoil pitching about 12° provided excessive drag during the gradual pitch-down motion. An impulse pitch-up motion, which is associated with a high angle of attack rates, generate a lift transient response that surges beyond quasi-steady value mainly because of significant added mass effects. In contrast, an impulse pitch-down rates incurred by the airfoil during the trapezoidal and the sawtooth waveforms generates a lower lift, but also lower drag. In some instances, negative drag (thrust) is produced for an impulse pitch-down motion but is not sustained throughout the periodic motion.

Power spectra Analysis

Power spectra analysis shows that the non-linearity in the lift response plays a significant role in lift production. The trapezoidal and the reverse sawtooth consistently generated large unsteady lift amplitudes across all angles of attack, which is strongly supported by the double vortex formation from Ol et al. [49]. Non-linear effects are the most dominant at 12° AoA, and the contributions of first and second harmonics reached up to 52% of the total lift generated for the reverse sawtooth waveform at 12° AoA.

Measured lift vs state-space model

Experimental measurements are also compared with Theodorsen's model and a state-space representation in a fully attached flow. The results show that Theodorsen's model captures the unsteady lift well in fully attached flow, but slightly over-predicts the lift amplitude at a higher reduced frequency of $k = 0.09$. This disparity may be possibly due to the significant presence of viscous effects at low Reynolds number. General trends of the lift force from the state-space model for the trapezoidal waveform compares well with the experiment, but over-predicts general lift amplitudes of the trapezoidal waveform due to the formation of lift-transients during high acceleration rates within the periodic motion. Responses for sawtooth and reverse sawtooth are in good agreement with the responses from the state-space model with only minor discrepancies at large angle of attack rates. Overall, the state-space model is a reasonable tool to capture the unsteady effects of an arbitrary pitching motion other than sinusoidal.

3.4 Summary of Major Findings

- For low reduced frequencies, in attached and semi-attached flow, a reverse sawtooth waveform generates the greatest mean lift.
- In a separated flow, a sine waveform produces the most substantial lift-to-drag ratio.
- The C_L responses due to harmonics provide evidence of a lift enhancement mechanism at post-stall angles of attack.
- The state-space model is reliable to predict general trends in the unsteady lift for arbitrary pitching motion.

Chapter 4

Effects of Flexible Propulsors on Hydrodynamic Forces

The contents of this chapter are based on the preliminary results of the following article: *Shehata, H. M., Hajj, M. R., Woolsey, C. A., Ragab, S. (2019). Effects of Flexible Propulsors on Hydrodynamic Forces. IFAC-PapersOnLine, 52(21), 14-20 [126].*

The use of oscillatory actuation of a deformable hydrofoil trailing edge for rigid and flexible bodies as a potential mechanism for improved thrust performance of swimming vehicles was investigated by performing force measurements in a water towing tank. This chapter provides detailed measurements of the thrust forces and servo torques and determines the effect of tail flexibility, actuation frequencies, amplitudes and forward swimming forces on overall propulsive performance.

4.1 Experimental Setup

4.1.1 Test facility

Measurements were obtained by towing the device from an instrumented towing carriage within the Virginia Tech Towing Basin. The basin is 30 m long, 1.8 m wide and 1.2 m deep. The carriage is driven by a 400 VDC motor and is capable of reaching towing speeds up to

3 m/s. The carriage speed, as indicated by a tachometer, is logged by the data acquisition system along with force and moment components from the 6DOF force balance and various signals of interest within the prototype. Elements of the test facility are shown in Figure 4.1.

Figure 4.1: From left to right: Towing carriage and control panel unit, and towing tank

4.1.2 Test Article

The physical device used for the experimentation is shown in figure 4.2. The forebody and the tail piece were 3-D printed using Abs-M30 material. The forebody of the swimming prototype (light blue part in figures 4.2 (b) and 4.2 (c)) has the shape of a NACA-0024 airfoil truncated at 75% of its chord length. The rest of the body consists of an attached tailpiece (the purple and circular swiveling bracket in Figure 4.2) that is connected to the back end of the forebody by a hinge that allows for smooth rotation. From the top view, the tailpiece itself is semi-elliptical in shape that extends into a rectangular planform with two side drill holes and a cavity to which the tail panels of any shape, length, and material are attached to. The total length of the forebody from its leading edge is 45 cm with the tailpiece

and 41 cm without the tailpiece. The height of the prototype, i.e., the span, is 10 cm. The sting onboard the carriage that holds the prototype in place was set at full extension making the distance between the top surface of the prototype roughly 0.31 m under the surface of the water, and 0.76 m away from the end walls.

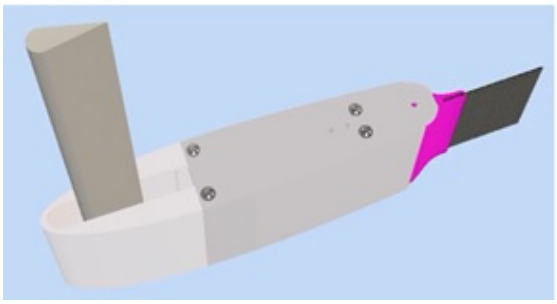

(a) CAD drawing of the model

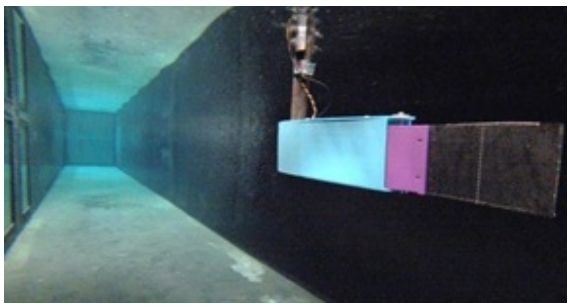

(b) Swimming model

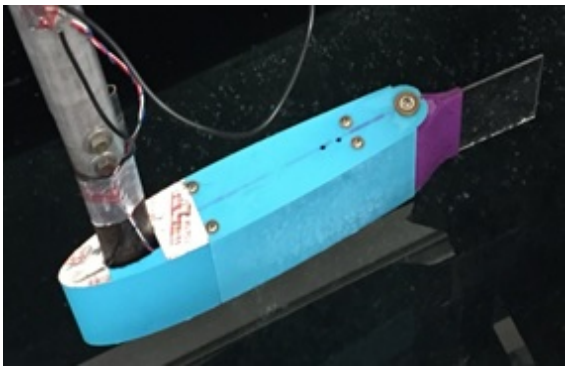

(c) Assembled model

Figure 4.2: Physical Device used for experimentation

The forebody compartment contains the waterproof L-shaped sting balance with wires running from the strain gauge up to the onboard box converter. The aft compartment (tailpiece) contains the servo motor. The tail joint was actuated using a waterproof Hitec WPHS-55 high torque high voltage servo to provide the oscillatory motion with a range of $\pm 20^{\circ}$ relative to the hinge point. Figure 4.3 shows a detaied and transparent view of the swimming device.

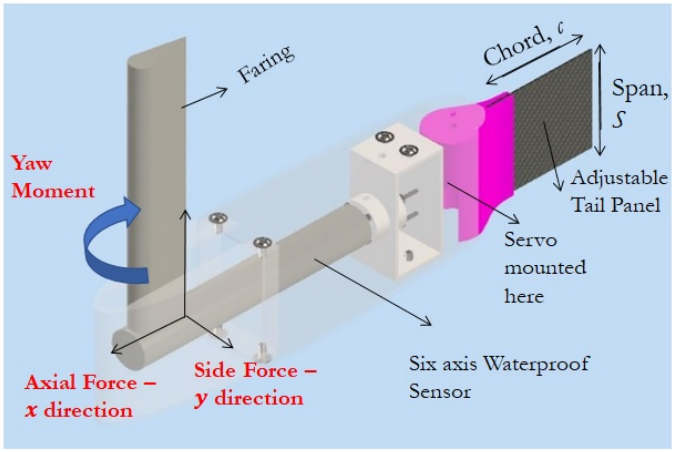

Figure 4.3: CAD model - transparent view

4.1.3 Data Acquisition System

The load cell used is a sting balance SB-100 model from Modern Machine & Tool Co. Inc. as shown in figure 4.4. The load cell has load limits of 445 N in the axial direction (direction of the flow, x), and 90 N in the normal and lateral (y and z) directions. The load cell is connected to a box converter (Figure 4.4) that converts the strain gauge voltages to axial, normal and side forces, and yaw, roll and pitch moments. The strain signals are then fed to a Vishay Micro-Measurements 2310 signal conditioning amplifier. All signals are conditioned using analog electronics and logged using LabVIEW. Data are acquired at 1000 Hz from a National Instruments (NI) myDAQ, and a LABVIEW interface was used to display and record the time histories of forces and torques.

The measurements for servo torque are based on the properties of the servo used. As with motor systems, the output torque for the servo was approximated by correlating the input current with the output torque. To find this relationship, calibrations were performed using a microcontroller, PWM driver, test servo, torque measuring circuit, C++ program, and a MATLAB script to sample and log real-time servo current draw at different applied torques.

Figure 4.4: 6DOF Sting Balance SB-100 model (left), strain gauge box converter (right)

The microcontroller used for control and acquisition is a Teensy 3.5 microcontroller. The PWM driver is a PCA965 and is used to control the servo using I2C commands from the Teensy directly. The torque circuit consisted of an analog current sensor (ACS712), bias remover, single pole RC filter, and external 16-bit analog to digital converter (ADS1115). The output torque measurements for the prototype experiments were found by converting the analog voltage output of the torque measuring circuit to servo output torque in N-m using servo torque calibration tests.

4.1.4 Uncertainty Analysis

To estimate the uncertainty in signal measurements obtained from the strain gauges, and servo torque current sensors, a method similar to the one employed in Alam et al. [103] is used. The load cell signal was captured for 10 seconds for three trials, corresponding to 1,500 samples of data, and the distribution of the sample averages was obtained. The corresponding standard deviation (σ) was approximately 3.9% of the mean value. The 2σ value of $\pm 7.8\%$ indicates the F_x strain gauge measurement uncertainty at the 95% confidence level. The same technique are applied to estimate the sensor uncertainties in F_y, M_z and the servo torque, and the servo angles; these are $\pm 3.6\%$, $\pm 8.4\%$, and $\pm 1.4\%$ respectively.

Each servo's angular position is acquired from the wiper voltage of the servoactuator's potentiometer, sampled at 50 Hz. The analog voltage is converted to angular position (in degrees) using a previously calibrated curve fit. A time delay is set by the microcontroller's clock input which commands a signal to drive the servo at a given frequency, producing an uncertainty in frequency inputs of ±0.005 Hz. The frequency input to each servo is verified by examining the Fourier transform of the potentiometer measurements.

4.1.5 Experimental Test Matrix

The input waveform to the flap had the form $\theta(t) = \theta_A \sin(\omega t)$ with both forebody and tail panel's mean angle of attack set to zero degrees. Here θ_A is the leading edge amplitude (the rotation angle at the leading edge) of the oscillating tail with respect to the x direction and $\omega = 2\pi f$ where f is the forcing oscillatory frequency. Three tail panels were used for the current experiment. Their dimensions and material properties are listed in Table 4.1. The dimensions for each panel are expressed as chord length, c by tail Span, S by thickness, h.

Table 4.1: The tail panels used for testing on the fish prototype. * Values for β are computed with U_{ref} of 0.35 m/s.

Panel	Relative thickness h/c	Dimensions (cm)	Flexural Rigidity β^*	Mass ratio, μ
a	22.2 $\times 10^{-3}$	9 × 9 × 0.2	8.7	0.026
b	1.7 $\times 10^{-3}$	9 × 9 × 0.015	2.8	0.004
c	0.8 $\times 10^{-3}$	18 × 9 × 0.015	0.3	0.002

The flexural rigidity, β, is a non-dimensional term that represents the tail stiffness:

$$\beta = \frac{Eh^3}{12(1-\nu)\rho_{\text{f}} U_{\text{ref}}^2 c^3} \tag{4.1}$$

where U_{ref} is the reference flow velocity relative to the forebody, f is the tail oscillating

frequency, c is the chord (panel) length of the tail, h is the thickness of the tail panel, ρ_{f} is fluid density, and E and ν are the Young's modulus and Poisson ratio of the tail's material respectively. The values of β for the tested panels at freestream velocity of 0.35 m/s are also presented in Table 4.1. Based on these values, tail 'a' is termed as the most rigid and tail 'c' is termed as the most flexible.

The non-dimensional mass ratio μ [127, 128, 129] is defined as:

$$\mu = \frac{\rho_{\mathrm{s}} h}{\rho_{\mathrm{f}} c} \tag{4.2}$$

Here, ρ_{s} and ρ_{f} are the material's and fluid densities respectively. This ratio is the product of the specific gravity $\rho_{\mathrm{s}} \,/\, \rho_{\mathrm{f}}$ and effective thickness h/c. The materials used were acrylic for tail 'a' with a density of $1,190$ kg/m^3 and a Young's Modulus of 3.2 GPa, and a carbon fiber for tail panels 'b' and 'c' with a density of $2,276$ kg/m^3 and Young's Modulus of 29 GPa. The tail panel's aspect ratio is the ratio of the panel's span to its chord length, $AR = S/c$. The aspect ratios for panels 'a', 'b' and 'c' are 1, 1 and 0.5 respectively.

The axial force and torque measurements were obtained for two test cases. In case A, the forward speed was set to zero, and all forces and torques generated were influenced primarily by the fluid's added mass effects. Case B included tests performed at a forward speed of 0.35 m/s where all forces and torques are generated by added mass effects, circulation and vorticity effects.

4.2 Results and Discussion

Because in case A, the mean swimming velocity $\bar{U}$ cannot be predetermined, an appropriate scaling parameter for velocity would be the tail peak velocity defined by $U_{\mathrm{p}} = 2\pi f A_{\mathrm{p}}$,

where A_p is the maximum amplitude of the tip of the tail panel [85, 130, 131]. The tail's peak to peak amplitude of the motion generated by the trailing edge of the panels is a function of system response and is dependent on inertial, elastic and hydrodynamic forces. Peak amplitudes were determined by observing the trailing edge of the panels during the oscillations using a position tracker Matlab script applied to video imagery acquired by a GoPro Hero5 at 120 frames per second and 1080p resolution. Instant image shots of the deforming panels can be found in Appendix B.

4.2.1 Case A: Measurements Without Towing Speed

Table 4.2 shows the range of parameters used for testing at zero forward speed. For all results presented in Figures 4.5, 4.6 and 4.7, the thrust forces and servo torques increase monotonically with amplitude and frequency with a tendency to flatten at higher forcing frequencies for the less flexible tails. Tails 'a' and 'b' both generate larger thrusts at higher frequency of oscillations and amplitudes. Figure 4.7 shows that over the range of tested frequencies, thrust peaks were observed at around 0.7 and 0.8 Hz for all amplitudes for panel 'c'. Thrust peaks occur at lower frequencies for panels with lower flexural rigidity (more flexible). The results may indicate that operating at frequencies close to structural resonance can increase peak thrust.

Table 4.2: Range of operating conditions without towing speed

Parameter	**Range**
Free stream velocity, U_∞ (m/s)	0
Frequency of excitation, f (Hz)	$0.5 - 3.0$
Leading edge amplitude, θ_A	6°, 8°, 10°, 12° and 15°
Mean angle of attack, θ_0	0°

Figure 4.8 shows the relative peak amplitudes A_p for panels 'a', 'b' and 'c' obtained as a result of the tail's fluid-elastic response. The peaks were obtained for four successive half strokes,

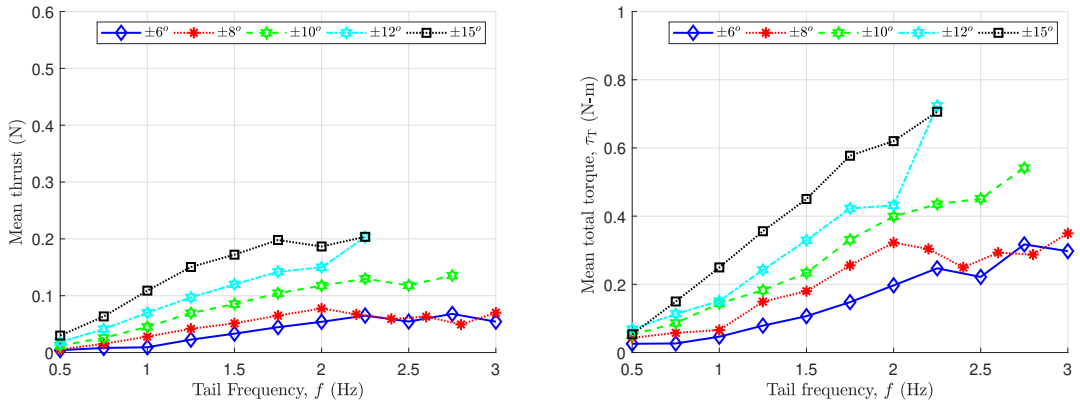

Figure 4.5: Thrust (N) and total torque, τ_{T} (N-m) measurements at various leading edge amplitudes and frequencies for tail panel 'a' (most rigid).

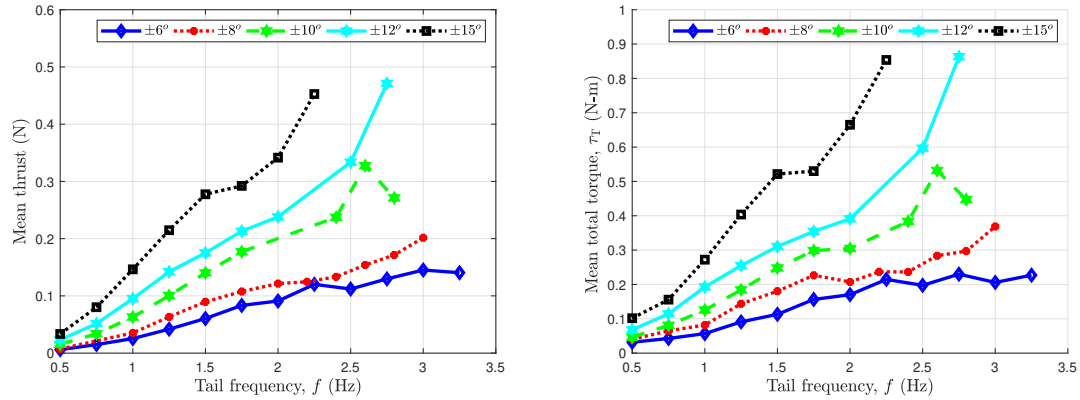

Figure 4.6: Thrust (N) and total torque, τ_{T} (N-m) measurements at various leading edge amplitudes and frequencies for tail panel 'b'

where three trials of A_{p} measurements were taken for every half a stroke and averaged. A maximum peak amplitude typically occurs around the panel's first bending mode. Panel 'b' shows an increase in peak amplitudes of approximately 5 to 40% relative to the rigid panel, panel 'a', whereas panel 'c' shows an increase in peak amplitudes of approximately 40 to 240 % relative to panel 'a' but only for a selected range of input frequencies between 0.5 Hz and 1.5 Hz. Beyond that range of frequencies, the structural response of panel 'c' yields peak amplitudes lower than panel 'a', which suggests that the beam may be exhibiting another

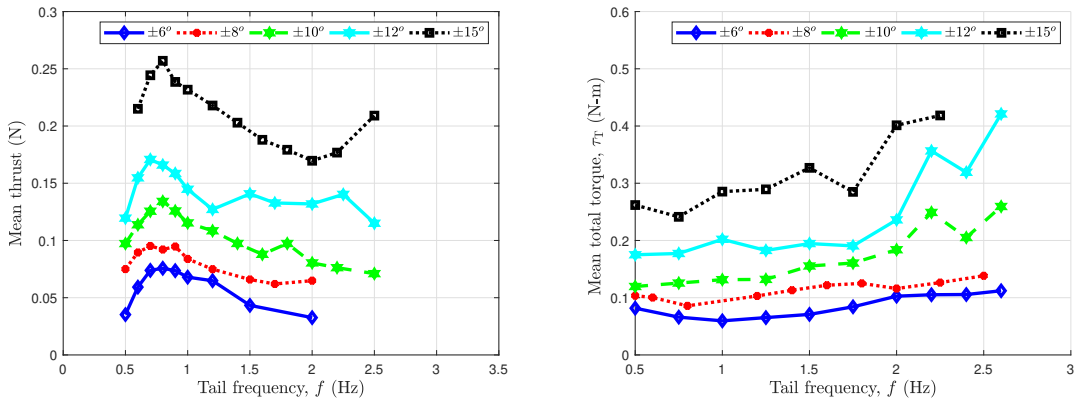

Figure 4.7: Thrust (N) and total torque, τ_{T} (N-m) measurements at various leading edge amplitudes and frequencies for tail panel 'c' (most flexible).

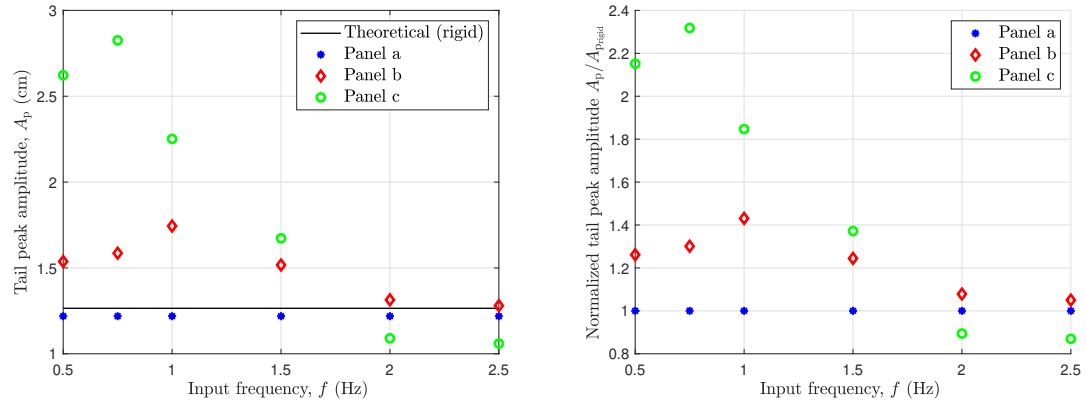

Figure 4.8: Dimensional peak amplitude (left) and normalized peak amplitudes (right)

mode of bending or a coupled mode between bending and torsion.

The relative peak amplitude, $A_{\mathrm{p}}/A_{\mathrm{p_{rigid}}}$, is strongly dependent on input frequency. The maximum deflections are observed for panel 'b' at 1 Hz and for panel 'c' at 0.75 Hz. Comparing these values with the theoretical natural frequencies computed using the Euler-Bernoulli's beam theory in vacuum suggests that added mass effects, and potentially viscous and vorticity effects, can lower the structure's first natural frequency. One analytical effort to determine the effect of water damping on the free vibration response of a rectangular cantilever beam

was described by Kramer et al. [132]. The study found that the added mass generated as a result of the fluid-structure interaction caused the natural frequencies of their composite plate to drop by 50% to 70% in water compared to in air. The water acts as a source of damping on the panel, thus the natural frequency is reduced. The natural frequency changes significantly with material density (specific density) and geometric ratio (h/c). As the density of the fluid increases, the natural frequency reduces. Consequently, the added mass effects are larger for materials with lower density. For example, the added mass effects for a composite material would be larger than for steel because the density of the composite is approximately 3-4 times lower than the density of steel.

An analytical estimate to determine the natural frequency of an immersed cantilever beam is expressed as (Kramer et al. [132]):

$$\frac{\omega_{\text{fluid}}}{\omega_{\text{air}}} = \sqrt{\frac{m_{\text{s}}}{m_{\text{s}} + m_{\text{a}}}} = \frac{1}{\sqrt{1 + \frac{\pi}{4}\frac{c}{h}\frac{\rho_{\text{f}}}{\rho_{\text{s}}}}} \tag{4.3}$$

where, m_{a} and m_{s} are the added mass of the fluid displaced and the mass of the material, respectively, and ω_{air} and ω_{fluid} are the material's natural frequency in air and water, respectively. We assume here that the discrepancy between the natural frequency in air and vacuum is negligible. Equation 4.3 can be re-written in terms of the non-dimensional mass ratio μ:

$$\frac{\omega_{\text{fluid}}}{\omega_{\text{air}}} = \left[1 + \frac{\pi}{4\mu}\right]^{-1/2} \tag{4.4}$$

Note that this expression is derived from two-dimensional potential flow theory [133]. The approximate analytical solution accounts for the added mass of the fluid that is displaced by the deforming beam. However, the solution does not account for viscous effects, and

therefore, an overestimate (or underestimate) of the added mass is expected. Despite these limitations, the solution still provides a reasonable estimate of the frequency ratios given that there is no coupling between the bending and twisting modes (i.e., no warping). An analytical estimate for the first natural frequency of panels 'b' and 'c' is presented in Table 4.3 alongside the first natural frequency determined by the Euler-Bernoulli beam theory and by qualitative experimental observation. The analytical estimate shows that water reduces the natural frequency by about 93% and 95% for panels 'b' and 'c', respectively, whereas observation from the experiment shows that the natural frequency in water reduces by approximately 97% and 91% for panels 'b' and 'c', respectively.

Table 4.3: Theoretical vs experimentally obtained first mode natural frequencies.

Panel	Natural frequency: Vacuum (Euler-Bernoulli)	Natural frequency: Water (Experiment)	Natural frequency: Water (Analytical [132])
a	49 Hz	N/A	N/A
b	35 Hz	1 Hz $\pm$ 0.25 Hz	2.42 Hz
c	8.7 Hz	0.75 Hz $\pm$ 0.125 Hz	0.43 Hz

In Figure 4.9, we plot the thrust force generated as a function of the tail peak amplitudes. Tail panel 'a' assumes a constant peak amplitude as expected since its rigidity properties restrict any large tip deformations. The thrust generation for panel 'a' under the stated test conditions is independent of the peak amplitude. No direct correlation between tail peak amplitude and the maximum thrust force is observed for tail panel 'b' since the most significant thrust production does not correspond to the largest tail peak amplitude. For panel 'c', a strong correlation between thrust production and tail peak amplitudes is observed. The larger the tail peak amplitude, the higher the thrust production. The results shown in Figure 4.9 demonstrates that oscillating panel 'c' near structural resonance can enhance the effect on the coupled elastic, inertia and fluid forces generated by the tail. This behavior is not observed for panel 'b'.

Figure 4.10 shows the thrust-force time histories for all tail panels. The responses were

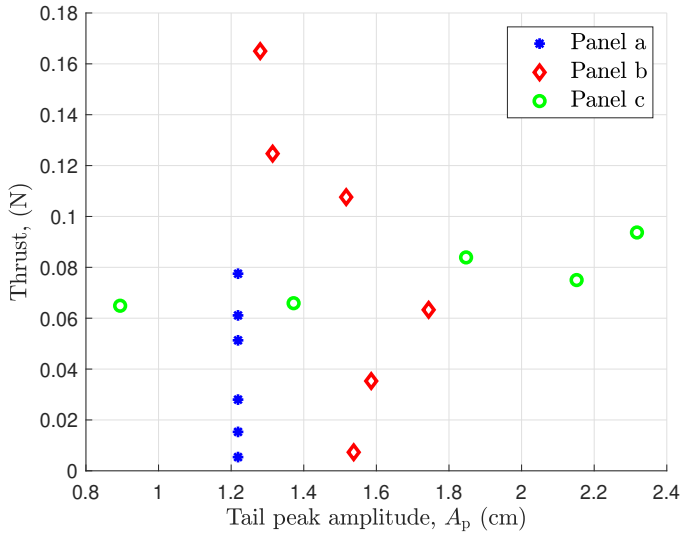

Figure 4.9: Thurst versus peak amplitudes

generated for the same leading edge amplitude input of $\theta_A =$ 8° at oscillatory frequencies of 0.5 Hz, 0.75 Hz and 1 Hz. Panel 'c', which is the most flexible panel, generates at least five times the instantaneous thrust force (absolute value) in comparison to panels 'a' and 'b' at 0.5 Hz. Panels 'a' and 'b', with the same aspect ratio, generate similar responses in thrust force at the tested frequencies. Likewise, the thrust peak values for panel 'c' are approximately three times the thrust peak values of panels 'a' and 'b' at 0.75 Hz, and two times the thrust peak values of panels 'a' and 'b' at 1 Hz. The absolute thrust values for panel 'c' relative to panels 'a' and 'b' start to drop with increased frequency of oscillations. Additionally, both panels 'a' and 'b' begin to generate larger thrust forces at higher frequencies of oscillation as previously portrayed in Figures 4.5 and 4.6.

The value of the thrust peaks at 0.5 Hz for every half a stroke of flapping motion are identical in absolute value. This behavior is dependent on the initial conditions of the flapping motion. Referring to the conventional notation of an inertial coordinate system (see Figure 4.3), the initial execution of the flap motion goes from zero angle of incidence to +8°, which in

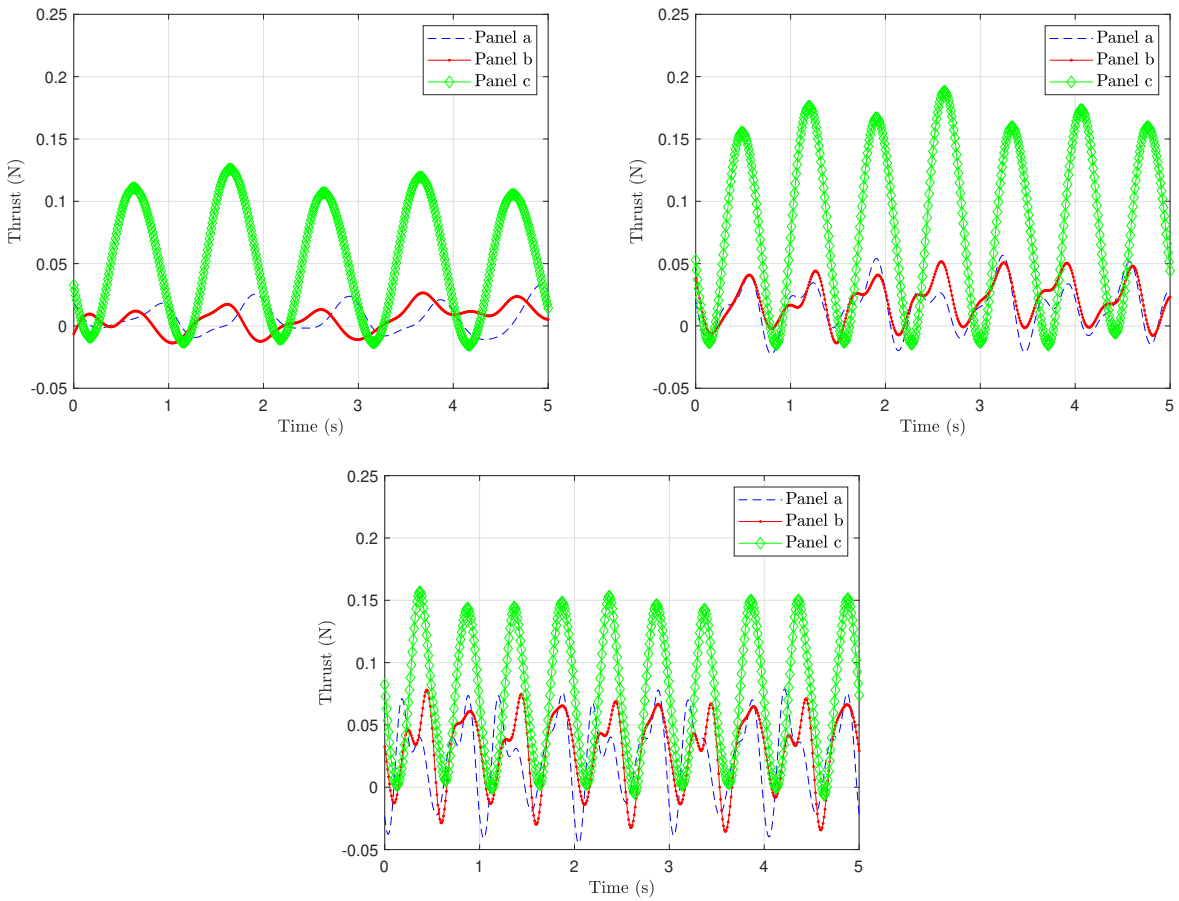

Figure 4.10: Time series for instantaneous thrust force for frequency of oscillation of 0.5 Hz (top left) , 0.75 Hz (top right), and 1 Hz (bottom). Panel 'a': blue dashed, panel 'b': solid red, panel 'c': green diamond.

turn, can generate vorticity effects that would register on the load cell as a higher (or lower) magnitude relative to its consecutive peak. If you reverse the initial execution of the flapping motion (i.e., from zero angle of incidence to $-8°$), the peaks for each consecutive half a stroke of flapping motion will reverse. This explains why the thrust-time history for panel 'c' at 0.5 Hz produces identical absolute values at every other peak. The thrust-time history for panel 'c' might reveal that panel 'c' is generating substantially large scale vortices at the first half stroke of the flapping due to a strong non-linear coupling of the fluid-elastic response. This behavior in thrust-time history is not observed for the other two panels. We also notice

from the thrust-time histories that the relative height of the alternating peaks at higher frequencies is attenuated at 0.75 Hz and almost disappears at 1 Hz. At lower frequencies, we can claim that vorticity effects from potential shed vortices have enough time to significantly contribute to the global flow field around the tail. In contrast, at higher flapping rates, any vortex being formed does not have enough time to self-sustain between every full flapping motion.

Figure 4.11 shows a comparison of the propulsive efficiency for all panels at zero freestream velocity. The propulsive efficiency is expressed as the Froude efficiency defined by:

$$\eta_{\text{prop}} = \frac{C_{\mathcal{T}}}{C_{\mathcal{P}}} = \frac{\mathcal{T} U_{\text{ref}}}{\mathcal{P}} \tag{4.5}$$

where $C_{\mathcal{T}}$ and $C_{\mathcal{P}}$ are respectively the thrust and power coefficients and expressed as:

$$C_{\mathcal{T}} = \frac{\mathcal{T}}{\frac{1}{2}\rho U_{\text{ref}}^2 Sc} \qquad C_{\mathcal{P}} = \frac{\mathcal{P}}{\frac{1}{2}\rho U_{\text{ref}}^3 Sc} \tag{4.6}$$

where $\mathcal{T}$ is the mean of the measured thrust (axial force) and $\mathcal{P}$ is the mean power input required by the servo to oscillate the panels from the leading edge. The mean power is computed as the mean of the product of the instantaneous hydrodynamic torque, τ_{H} and the tail's prescribed angular velocity ω.

$$\mathcal{P} = \overline{\tau_H \omega} \tag{4.7}$$

The hydrodynamic torque, τ_{H} is obtained by subtracting the panel-free torque τ_{PF} from the total servo torque τ_{T}. The panel-free torque τ_{PF} is the torque required to move the tailpiece only (without a panel) in the water at all frequency points. In specific, the mechanical torque

is the total of mechanical friction and hydrodynamic torque required to move the tailpiece only. The total servo torque is the torque measured at all frequency points in the presence of a tail panel. In equation 4.7, ω is the angular velocity obtained from the first time derivative of the prescribed simple harmonic motion of the tail panels.

The velocity U_{ref} that can be used for this set of results is U_{p}, which can be obtained using the peak amplitudes presented in Figure 4.8 to compute the propulsive efficiency. Although the scaling approach used here is an appropriate one, it does not apply to a device that is not moving and is not necessarily directly comparable with the propulsive efficiencies obtained for the case with freestream flow; i.e., case B. Instead of using the conventional definition of propulsive efficiency at zero freestream velocity, another way to measure performance is to use a thrust-to-power-input ratio [131]. The results in Figure 4.11 reveal that the thrust-power input ratio is greater for the flexible panels than for the rigid panel.

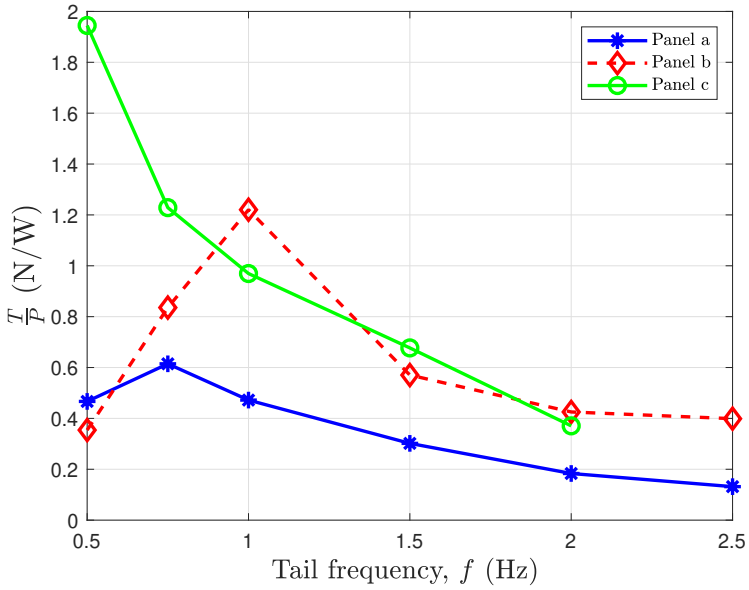

Figure 4.11: Thrust-to-power ratio for all three panels at zero freestream flow. Panel 'a': blue star panel 'b': red diamond, panel 'c': green circle,

4.2.2 Case B: Measurements With Towing Speed

In this subsection, forces and torques were measured and recorded when the prototype was towed at a speed of 0.35 m/s. Table 4.4 shows the range of input parameters used for this test condition. In the case of forward speed, the net thrust force is the force generated due to the addition of flow circulation, and viscous body drag. The thrust force, $\mathcal{T}$ generated due to these effects was determined by taring the static body drag measured when the prototype was towed unactuated, D_{body}, from the net thrust force obtained from direct force measurements when actuated and towed, $\mathcal{T}_{\text{net}}$. The fish prototype is forced to swim at the speed of the towing carriage to represent a steady current of speed U_∞.

Table 4.4: Range of operating conditions with towing speed

Parameter	**Range**
Free stream velocity, U_∞ (m/s)	0.35
Frequency of excitation, f (Hz)	$0.5 - 3$
Leading edge amplitude, θ_A	8°
Tail's mean angle of attack, θ_0	0°

$$\mathcal{T} = \mathcal{T}_{\text{net}} - D_{\text{body}} \tag{4.8}$$

Figure 4.12 shows the true body drag values generated by towing the prototype (unactuated and with a detached panel) at speeds of 0.35 m/s, 0.51 m/s and 0.68 m/s. The corresponding Reynolds numbers are 1.6×10^5, 2.5×10^5 and 3.3×10^5. The drag forces have a quadratic relationship with flow velocity, and are directly proportional to the velocity squared, a behavior typically expected. The drag coefficients of the forebody at the three non-zero speeds are 0.062, 0.059 and 0.063 respectively. The averaged drag coefficient over the three speeds is 0.061. The results from drag measurements are in relative agreement with results from Sogukpinar [134] for a three-dimensional NACA-0024 with a drag coefficient value of 0.057

at zero angle of attack and $Re = 6 \times 10^6$. Body drag force is possible because of the creation of three-dimensional tip vortices coming off both ends of the prototype.

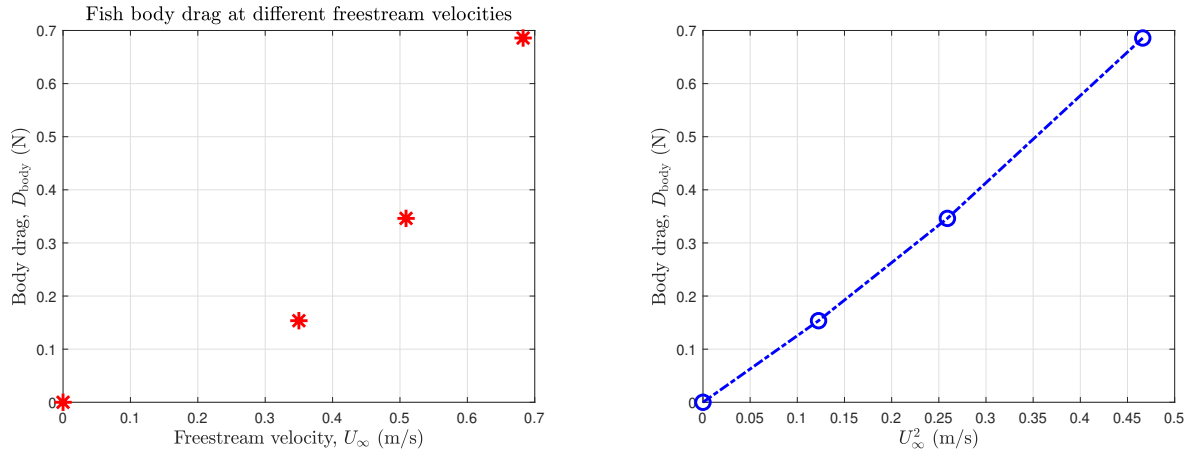

(a) Body drag force vs freestream velocity

(b) Body drag force vs freestream velocity squared

Figure 4.12: Body drag force vs freestream velocity and freestream velocity squared

Two additional non-dimensional frequency parameters are introduced. These are the reduced frequency, k, and Strouhal number St :

$$k = \frac{2\pi f c}{U_{\text{ref}}} \quad \text{and} \quad St = \frac{f A_{\text{p}}}{U_{\text{ref}}} \tag{4.9}$$

where, A_{p} is the peak amplitude which is the recommended scaling parameter extensively used in literature. Since the peak amplitude varies as a function of the experimental parameters, the Strouhal number is a measured output, rather than a prescribed parameter. Measurements are therefore presented as a function of the reduced frequency, which is an experimental input parameter.

The coupling effect between aspect ratio and stiffness on propulsive performance can be isolated in this set of results. Panels 'a' and 'b' have the same aspect ratio and only vary in material type and hence flexibility, whereas panels 'b' and 'c' are the same material, but

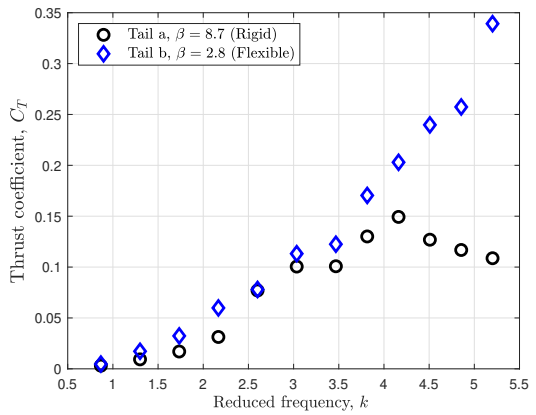

(a) Thrust coefficient vs reduced frequency

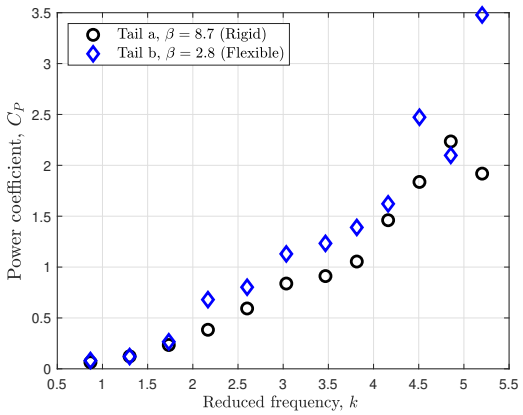

(b) Power coefficient vs reduced frequency

Figure 4.13: Thrust and power coefficients for tail panels 'a' and 'b'

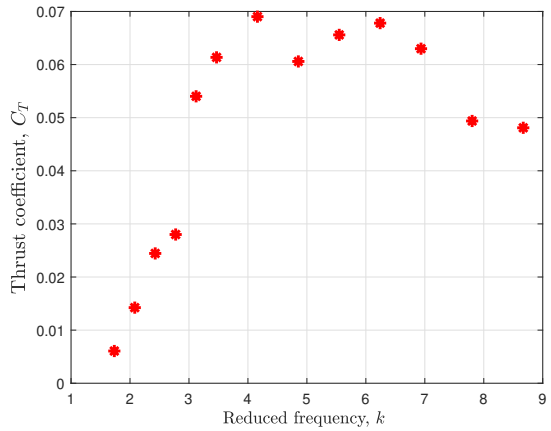

(a) Thrust coefficient vs reduced frequency

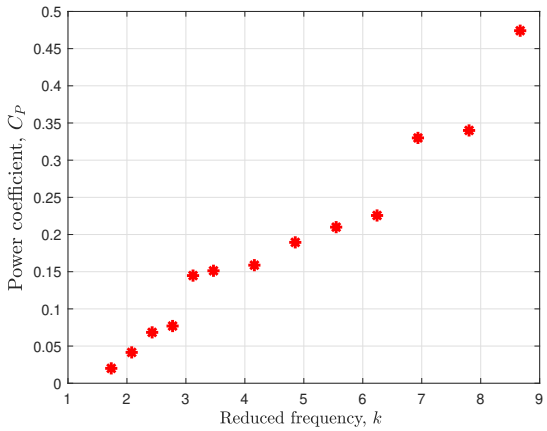

(b) Power coefficient vs reduced frequency

Figure 4.14: Thrust and power coefficients for tail panel C

vary in aspect ratio. Figures 4.13 and 4.14 show that at higher reduced frequencies, tail panels 'a' and 'b' generates higher thrust coefficient values than panel 'c'. However, for the range of reduced frequency between k =3.5 and k =5, panel 'c' generates higher dimensional thrust forces prior to converting the results to non-dimensional form. Out of the three tail panels, panel 'c' also requires the least amount of power input into the fluid to generate the

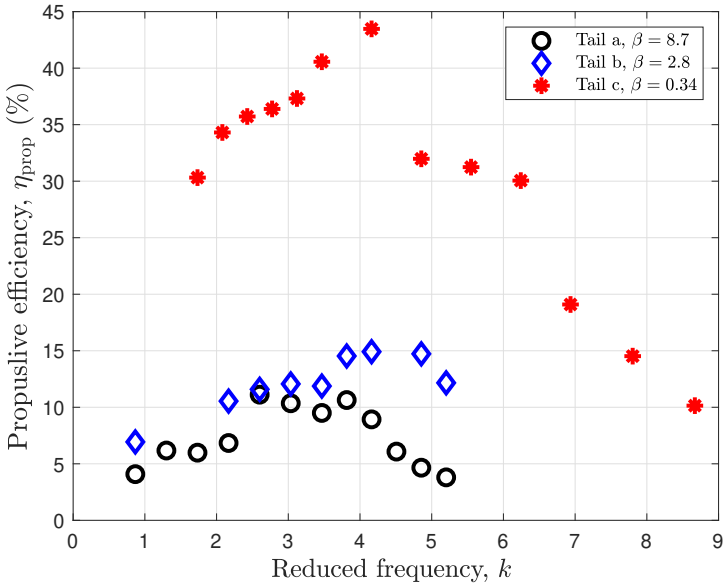

Figure 4.15: Full comparison of propulsive efficiencies

flapping motion.

When directly comparing tail panels 'a' and 'b', panel 'b' generates higher thrust forces for nearly the same servo torque requirements. At reduced frequencies beyond $k = 4$, it is clear that some degree of the fluid-elastic response exhibited by panel 'b' enhances thrust production.

Optimal propulsive performance is generally expected over a band of frequency where the flow exhibits favorable vortex behavior to the benefit of thrust production. Figure 4.15 compares the propulsive efficiency curves for all three tail panels. Tail panel 'c' shows propulsive efficiencies up to 45%, nearly three times that of panel 'b'. Panel 'b' is nearly eight times the flexural rigidity of panel 'c', and panel 'a' is nearly three times the flexural rigidity of panel 'b'. While panels 'a' and 'b' maintain the same aspect ratio and only differ in material property, tail 'b' was able to generate about a 35% increase in propulsive efficiency. The results show that flexibility enhances propulsive efficiency, although both geometric and material

properties tend to have different effects at different operating frequencies. Figure 4.15 also shows that the maximum peaks were observed at a range reduced frequency somewhere between $k = 4$ and $k = 5$ for tail panels 'b' and 'c', and at lower reduced frequency of $k = 3.8$ for tail panel 'a'. The propulsive efficiency peaks presented by Dewey et al. [85] are observed at around $k = 6$ to 7 for their panels P_4 and P_5 with flexural rigidity values close to our panel 'b'. The difference in results is due to several factors; the dominant one of them is that Dewey et al. [85] presented their results at a Reynolds number of Re=7,200. Reynolds number can have drastic effects on skin friction and pressure drag acting on the panel which as a result can alter thrust generation and power input to the fluid by the panels.

Effects of varying swimming speed (Reynolds number)

In this subsection, we briefly examine the effects of towing speed on the thrust forces generated by panel 'b' as a sample case study on the effects of Reynolds number on the force production of a flexible beam. For rigid foils, larger forward forces can be achieved at higher Reynolds number [135]. However, these forces are strongly dependent on both geometric and material properties. Ashraf et al. [136] determined in their study that the thickness of the airfoil plays a significant role in the propulsive performance for a rigid pitching airfoil at different Reynolds number. At higher Reynolds number, thick airfoils with small pitching amplitudes outperform thin airfoils. In contrast, at lower Reynolds numbers, thin airfoils can achieve substantially better propulsive performance.

Figure 4.16 shows the mean thrust force and the total torque required by panel 'b' at different actuation frequencies and pitching amplitudes of $\theta_A = 4°$ and $8°$. The forces presented in this section are the total axial force minus the steady drag force incurred by the forebody with the tail centered. In addition to a flow speed of 0.35 m/s, the resultant thrust forces are determined for two forward towing speeds: 0.51 m/s, and 0.68 m/s. With a forebody chord

of 45 cm and a tail panel chord of 9 cm, the corresponding Reynolds numbers at 0.35 m/s, 0.51 m/s and 0.68 m/s are Re=1.9 $\times$ 10^5, Re=3.0 $\times$ 10^5 and Re=4.0 $\times$ 10^5, respectively. We observe from the plots that across both pitching amplitudes, the most substantial thrust forces were generated at Re=1.9 $\times$ 10^5, which is the lowest Re among the three Reynolds numbers. Similarly, the torque requirements to oscillate the tail at any given frequency are the lowest for Re=1.9 $\times$ 10^5 across both pitching amplitudes. Despite the body force at each corresponding flow speed being tared from the dynamic results, the three-dimensional effects are likely to produce an additional source of drag at higher swimming speeds.

The results imply that thrust forces are more significant at lower Reynolds numbers and higher pitching amplitudes. Despite running the experiment at three different Reynolds numbers, the range of the selected Reynolds numbers is not spread out such that the dynamics of the flow alters significantly. This means that there is no extreme flow state change from laminar to turbulent flow. The selected Reynolds numbers are a dominantly turbulent flow regime since flow transition usually takes place around the range Re = 10^4. For this reason, it is believed that the swimming speed alone is a significant underlying factor in changing how thrust forces are generated. This observation is consistent with the findings of (Quinn et al. [86]) that a varying flow speed produces a significant change in forces on a flexible flapping panel. Also, with the tail panel taking the shape of a rectangle with a relatively low thickness to chord length ratio, the conclusion by Ashraf et al. [136] agrees with the results here.

The flapping of the tail in freestream flow can not only generate added mass forces but can also incur large scale vortex shedding that generates wake energy to overcome drag and develop thrust [137]. The concept of deformable bodies and wake energy can be related to the findings of Beal et al. [137], where if the panel resonates at some harmonic or sub-harmonic of the shedding frequency of a bluff body, thrust production can be enhanced as a result

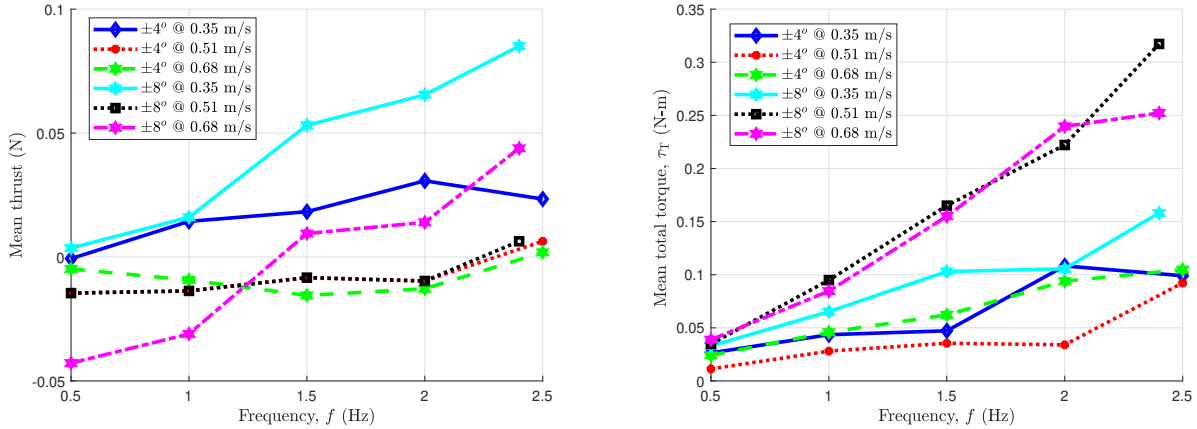

(a) Thrust force vs Reynolds number

(b) Torque vs Reynolds number

Figure 4.16: Effect of swimming speed on mean thrust forces and torques.

of an energy extraction mechanism. One way of physically interpreting our experimental results is to revisit the underlying mechanism that generates thrust for flapping foils. That is, the flapping of a fish-tail can generate a reverse Von-Kármán vortex street, which in turn, induces a jet in the direction of the swimming. Triantafyllou et al. [89] additionally reveals that the strength of the reverse Von-Kármán vortices generated by the flapping fish-tail is substantial when the flapping occurs within the suction region (low pressure region) of the flow downstream of its forebody. The strength of these vortices is an essential source of forward propulsion. Nevertheless, the larger the flow speed, the quicker these vortices dissipate further downstream of the flow, leaving behind a flow field with a weak resultant net jet force in the direction of the swimming, and a large flow momentum deficit (drag).

4.2.3 Comparing Case A and Case B

Figures 4.17, 4.18, and 4.19 directly compare the thrust generated in zero flow speed (case A) and 0.35 m/s flow speed (case B) for the three panels with a tail pitching amplitude of 8°. The comparison is made for all three panels. We reiterate that the thrust forces presented in

these plots for case B are determined by the difference between the net axial force recorded and the drag of the forebody measured (un-actuated with the panel detached). The results are consistent across all panels, showing the thrust generated in zero freestream are generally larger than the thrust generated in freestream flow. However, the advantage illustrated by case B over case A is that the servo in case B acquires less torque to actuate the tail panels at any given input frequency. In zero freestream, we argue that the flow around the flapping tail may incur vorticity effects in addition to added mass effects. With freestream flow, the combination of added mass, vorticity, viscosity, and circulation (both rotational and translational) can contribute to the overall resultant thrust force.

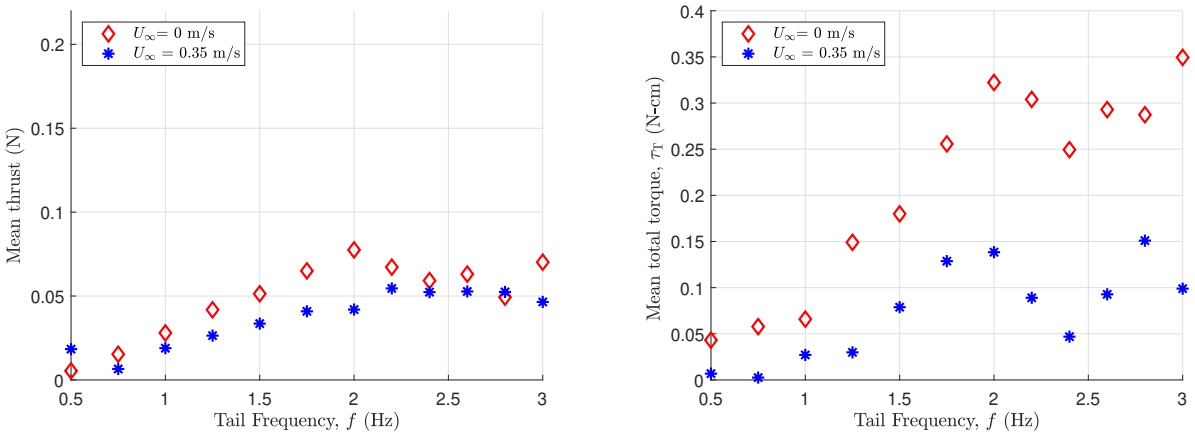

(a) Thrust vs frequency

(b) Servo Torque vs frequency

Figure 4.17: Panel 'a' : Thrust and servo torque comparisons between 0 m/s (case A) and 0.35 m/s (case B) flow speeds.

One other source of the force that is generated in freestream flow is the hydrodynamic lift induced thrust. This force mainly occurs because of the net circulation generated by large pressure differentials in the flow. Large pressure differentials are responsible for the fomration of vortices. The role of vorticity energizes the flow around the swimming body that allows the generation of thrust due to circulation. The results from Figures 4.17, 4.18, and 4.19 show that thrust generated due to circulation does not contribute significantly to the resultant

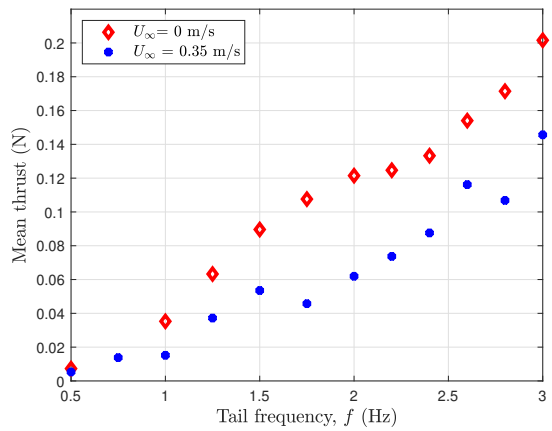

(a) Thrust vs frequency

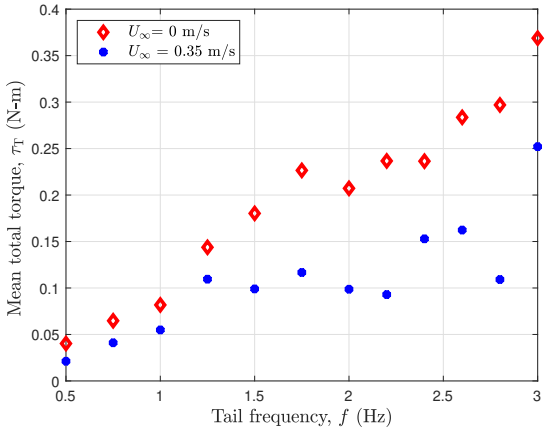

(b) Servo Torque vs frequency

Figure 4.18: Panel 'b' : Thrust and servo torque comparisons between 0 m/s (case A) and 0.35 m/s (case B) flow speeds.

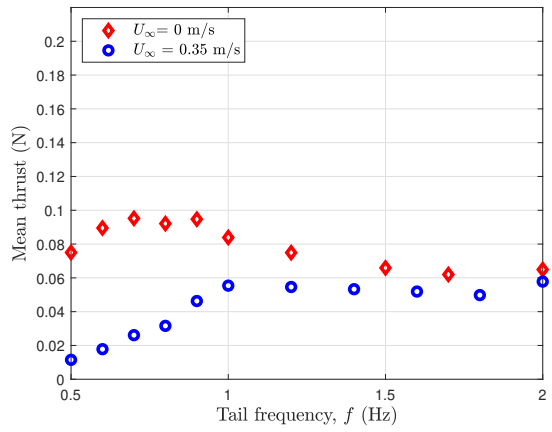

(a) Thrust vs frequency

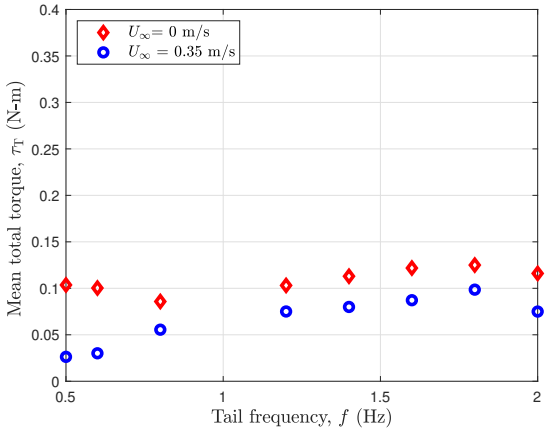

(b) Servo Torque vs frequency

Figure 4.19: Panel 'c' : Thrust and servo torque comparisons between 0 m/s (case A) and 0.35 m/s (case B) flow speeds.

thrust as it does not overcome the excess drag produced while towing the prototype. The additional source of drag could also come from circulatory effects from the flapping motion (Patil [138]).

We note in figure 4.19(a) a shift in peak thrust from 0.7 Hz, when panel 'c' flaps in zero freestream flow, to 1 Hz, when panel 'c' flaps in 0.35 m/s freestream flow. We also know

from this study that the peak amplitude in zero freestream corresponds with the maximum thrust peak value for panel 'c'. The results indicate that the effect of freestream flow (an inertial dominated flow regime) plays a role in raising the first natural frequency of panel 'c' in water by approximately 25%. As such, added mass effects in freestream flow are lower than in a zero freestream flow. In the same plot, we observe the same inflection point around 2 Hz for both zero freestream and non-zero freestream flow. Although we could not observe the peak amplitude and determine the second mode natural frequency of panel 'c' in water, the second natural frequency using the Euler-Bernoulli beam theory is 54 Hz. If we assume that the frequency ratio between water and air for panel 'c' persists at 91% as determined in Table 4.3, the second natural frequency of panel 'c' would be approximately 4.9 Hz. The inflection point we see at 2 Hz could very well be within a range of the second natural frequency of panel 'c' in water. Non-linear structural effect caused by large deformations of long tail panels is the dominant mechanism in driving the coupled structural and fluid non-linear responses. In specific, the resultant aeroelastic behavior is caused by changes in the frequencies and mode shapes of the system Patil and Hodges [139]).

4.3 Summary of Contributions

A single link swimming device has been designed, fabricated and tested in a towing basin. The results show that for the same oscillatory amplitudes and flow speed, an increase in frequency of oscillations results in a monotonic increase in thrust coefficients up to a peak frequency. This behavior is the same regardless of tail material flexibility.

At zero forward speed, thrust-to-power ratio peaks showed significant differences between three panels. Panel 'c' produced approximately 68% higher maximum thrust-to-power ratio value than panel 'b' (varying aspect ratio). Panel 'b' produced nearly 100% higher maximum

thrust-to-power ratio value than panel ‘a’ (varying material property).

At a speed of 0.35 m/s, the propulsive efficiency is more affected by changes in geometric properties (aspect ratio) rather than material properties. The results show that by incorporating three times the flexibility on rigid tail, panel ‘a’, the propulsive efficiency was enhanced by 35%. In addition, incorporating eight times the flexibility on panel ‘b’ resulted in panel ‘c’ generating nearly three times the propuslive efficiency. Increasing the material’s flexibility tends to shift the propulsive peaks to higher reduced frequencies. Isolating the effects of aspect ratio, lowering the aspect ratio for the same material generated larger differences in propulsive efficiency peaks, but produced no notable shift in efficiency peaks to a different frequency. Finally, it is determined that the overall flexibility of a material provides better peak propulsive efficiency values.

Structural resonance plays an active role in thrust enhancement for panel ‘c’ but not for panel ‘b’ despite exhibiting similar material properties. We also conclude that flapping the tails in water reduces the theoretical (Euler-Bernoulli theory) first natural frequency of panels ’b’ and ‘c’ by 97% and 93% due to large added mass and damping effects. These comparisons are in statistical agreement with an analytical model obtained from the literature. Additionally, a sample case study on the effects of swimming speeds on panel ‘b’ suggests that larger thrust forces are produced at lower swimming speed and larger pitching amplitudes. Finally, zero freestream flow generates more thrust forces, but requires more power input to oscillate the panels at any given frequency and amplitude compared to a non-zero freestream flow. By observing the peak thrusts for panel ‘c’, we also claim that the first natural frequency of panel ‘c’ increased by 25% while flapping the tail in a freestream flow.

4.4 Summary of Major Findings

- All panels produce larger thrust forces at lower towing speeds, but also require substantial torque for the same input parameters.
- The effects of material property have a considerable impact on propulsive performance (thrust-to-power ratio) in zero freestream flow.
- The effect of aspect ratio is substantial on propulsive efficiency in a non-zero freestream flow.
- The natural frequency in water is reduced substantially relative to the natural frequency in the air due to large added mass effects
- Resonance plays a significant role in the thrust peaks generated for panel 'c,' the most flexible panel among the tested panels.

Chapter 5

Hydrodynamic Performance of an Articulating Body: The Modular Biolocomotion Emulator (MBE)

The contents of this chapter are based on the preliminary results of the following article: *Shehata, H.M., Woolsey, C.A. and Hajj, M.R., 2019. Hydrodynamic Performance of a Modular Biolocomotion Emulator. IFAC-PapersOnLine, 52(21), pp.1-7 [140].*

This chapter presents experimental measurements of the internal and external forces and moments generated during forced oscillation of a *modular biolocomotion emulator (MBE)*. The *MBE* was towed at three different steady towing speeds (in addition to zero speed) while executing four distinct tail kinematics at various waveform frequencies. The MBE geometry and tail kinematics can be varied further to test a broader range of morphologies and "gaits". The tested tail kinematics considered were (a) sine wave, (b) leading edge pitching, (c) 1^{st} mode bending, and (d) 2^{nd} mode bending. The purpose of the experimental program is to develop a database of hydrodynamic force measurements that can be used to validate low-order computational methods, such as the unsteady vortex lattice method, and to provide preliminary results on the hydrodynamic forces and torques as a result of different tail kinematics.

5.1 Experimental Setup

5.1.1 Test Facility

The towing basin and test facility used for the experimentation of the MBE prototype was previously described in section 4.1.1.

5.1.2 Test Article

The test apparatus used in this work is the *MBE* described by Beardsley et al. [141]. The *MBE* comprises a series of rigid components called modules. The device allows for the addition or removal of modules to represent various morphologies. In its simplest configuration, with a forebody and a single rigid fin, the *MBE* generates ostraciiform motion. With an additional link between the forebody and the fin, the *MBE* can generate a carangiform motion. The locomotion modality varies from oscillatory to undulatory as the number of modules grows, eventually approximating anguilliform locomotion. For the experiments described here, the *MBE* is configured to support experiments at the carangiform end of the locomotion spectrum. It comprises four modules: a forebody, two faired actuator modules, and a single rigid fin or tail.

The forebody of the *MBE*, which contains some of the *MBE* control electronics, is fixed to an immersible six degree-of-freedom (6DOF) balance suspended below a towing carriage. Each module contains a servo-actuator capable of applying a control moment to the subsequent module. Specifically, each module houses a waterproof SAVOX SW1210SG high torque servo, powered by a 7.4 VDC supply, to provide the oscillatory motion required of each module in order to effect a desired gait. These servos are capable of producing 800.0 N-cm of torque and slewing 60° in 0.13 seconds.

The fairings are 3-D printed using Abs-M30 material, and are designed to allow each module to rotate relative to its neighbors while preserving a nearly continuous external shape. The forebody geometry is the leading 70% of a NACA-0024 hydrofoil. The modules between the forebody and tail have a constant span of 10 cm. The tail fairing geometry is the trailing 30% of the NACA 0024 hydrofoil. A CAD model of the *MBE* can be seen in Figure 5.1 and a top view schematic of the *MBE* as configured for these experiments can be seen in Figure 5.2. Additionally, photos of the prototype anchored to the sting on the water carriage are presented in Figure 5.3. The force and moment components F_x, F_y and M_z are measured using the 6DOF balance. The angles θ_1, θ_2 and θ_3 represent relative orientations for each module, which are affected by the servo control torques τ_1, τ_2 and τ_3. For additional details concerning the design of the *MBE*, its electronic instrumentation, or data acquisition, see [141].

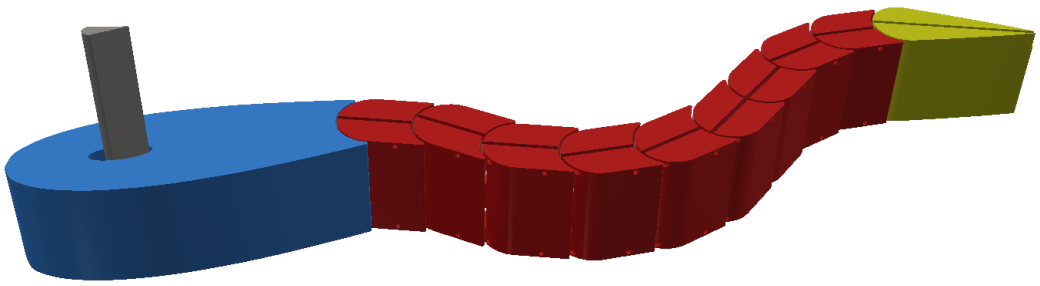

Figure 5.1: Rendering of the assembled, multi-link *MBE*.

5.1.3 Data Acquisition System

The load cell used is the 6DOF SB-100 sting balance manufactured by Modern Machine & Tool Co. as previously shown in section 4.1.3 (Figure 4.4). The sensor is connected to a box converter, also shown in Figure 4.4, which processes the strain gauge voltages to produce

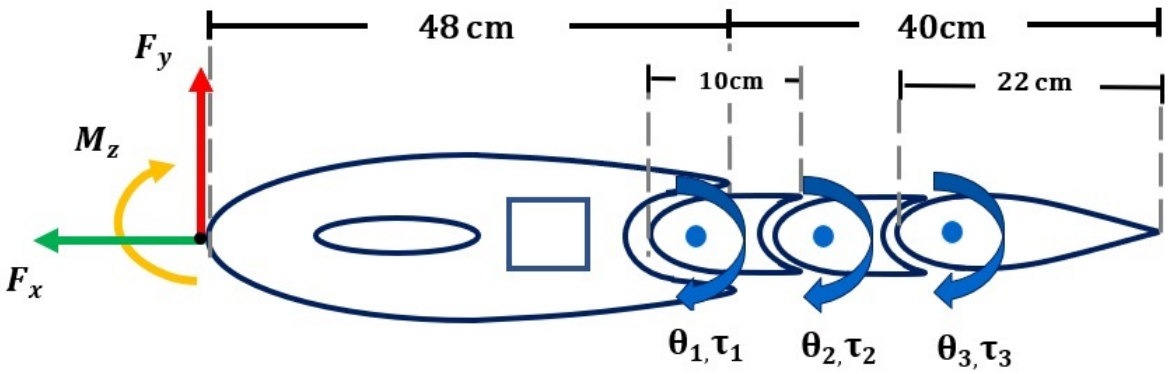

Figure 5.2: Schematic of the *MBE* as tested (top view).

measurements of axial, normal, and side forces and of yaw, roll, and pitch moments. Only the horizontal plane components are recorded in these experiments: axial and side force and yaw moment. The load cell's calibration limits are 445 N in the axial force direction (x), 90 N in the lateral force direction (y), and 4,500 N-cm in the yaw moment direction (about z).

The axial force F_x, lateral force F_y, and yaw moment M_z on the *MBE* forebody are obtained from the 6DOF balance. Strain signals are then fed to a Vishay Micro-Measurements 2310 signal conditioning amplifier. All signals are conditioned using analog electronics and logged using LabVIEW. Data are acquired at 50 Hz from two devices: a National Instruments (NI) myDAQ and a Teensy 3.2 microcontroller. The NI myDAQ acquires axial force, side force, and yaw moment data from the balance while the Teensy 3.2 acquires position and torque measurements from each of the servos. Each module on the *MBE* contains its own Teensy 3.2 microcontroller, programmed using the Arduino integrated development environment (IDE). The Teensy microcontroller delivers command signals to the servo and reads two analog voltages from it. The first analog voltage, measured at the wiper of the servo's feedback potentiometer, indicates the servo's angular position. The second analog voltage, obtained from an ACS712 current sensor connected in series with the servo, provides a measurement

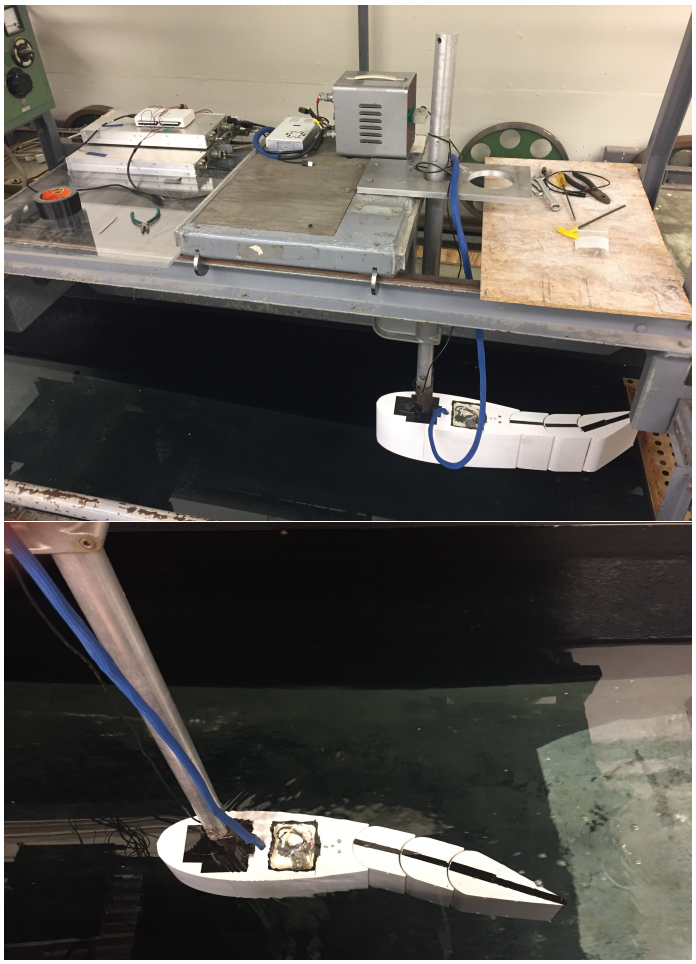

Figure 5.3: Photos of the *MBE* anchored and submerged in water.

of servo torque. Table 5.1 summarizes the input commands and output measurements for the experimental program.

Inputs	**Outputs**
Towing speed, U_∞ (m/s)	Axial and side forces, F_x and F_y
Tail frequency, f (Hz)	Yaw Moment M_z
Tail amplitude, A_P	Servo torques, $\tau_{1,\text{net}}, \tau_{2,\text{net}}, \tau_{3,\text{net}}$
Gaits, $\theta_1(t)$, $\theta_2(t)$, $\theta_3(t)$	Motion histories

Table 5.1: Experimental inputs and outputs

Within each module, the servo is powered directly from an 8.4 VDC bus while a voltage

regulator provides 5.0 VDC to power the microcontroller and current sensor. All Teensy 3.2 microcontrollers within the *MBE* share a single I2C communication bus, which requires only two serial communication lines (clock and data). The microcontroller in the forebody serves as a master on the communication bus. This device communicates separately via USB with a LabVIEW script running on a laptop computer aboard the towing carriage. All data acquired are smoothed using a digital fourth-order Butterworth low-pass filter to attenuate high frequency noise above a cut-off frequency that is 4 times the frequency of the kinematic waveform.

5.1.4 Uncertainty Analysis

The method to determine the uncertainty in force measurements from the sting balance was previously mentioned in section 4.1.4. The load cell signal was captured for 10 seconds for three trials, corresponding to 1500 samples of data, and the distribution of the sample averages was obtained. The corresponding standard deviation (σ) was approximately 3.9% of the mean value. The 2σ value of $\pm 7.8\%$ is the F_x strain gauge measurement uncertainty at the 95% confidence level. The same technique was applied to estimate the sensor uncertainties in F_y, M_z, the servo torques, and the servo angles; these were $\pm 3.6\%$, $\pm 8.4\%$, $\pm 0.9\%$ and $\pm 3.4\%$ respectively.

Each servo's angular position is acquired from the wiper voltage of the servoactuator's potentiometer. The analog voltage is converted to angular position (in degrees) using a previously calibrated curve fit. A time delay is set by the microcontroller's clock input which commands a signal to drive the servo at a given frequency, producing an uncertainty in frequency inputs of ± 0.005 Hz. The frequency input to each servo is verified by examining the Fourier transform of the potentiometer measurements.

5.1.5 Experimental Test Matrix

The particular motion exhibited by the device, as defined by the periodic waveforms that each of its actuators generates, is referred to as the "gait." The gait is defined by the fundamental waveform shape (sinusoidal, triangular, etc.), the frequency of oscillation of the modules, and the amplitude of oscillation of the *MBE*'s trailing edge.

To attain a desired gait, the servo-actuator within each module executes a prescribed motion history. Briefly, one determines the servo angle histories that best approximate the given gait for a given number of modules (three, in this case) by solving a system of nonlinear algebraic equations for the position of each servo. We consider four gaits: a sinusoidal wave, a "rigid pitching" gait, and two gaits which approximate a simple 1^{st} and 2^{nd} bending mode, respectively. For the sinusoidal wave, the angle input for each servo is determined by the amplitude of the sine function. For the rigid pitching gait, in which the modules all move in rigid unison, every servo outputs the same angle relative to the first module. As for the 1^{st} and 2^{nd} bending modes, the servo angles are determined by solving the Euler-Bernoulli beam equation. A schematic of these four gaits is shown in Figure 5.4. The prescribed servo angles (relative to the x-axis frame) for each waveform are presented in Figure 5.5.

Two test cases are considered:

- **Case A** - The MBE modules oscillate without forward motion ($U_{\text{ref}} = 0$). In this case, the measured forces and moment are purely those generated by the lateral accelerations of the components, that is, the apparent mass.
- **Case B** - The MBE modules oscillate while the apparatus moves forward in the x-direction at a steady speed ($U_{\text{ref}} = U_\infty > 0$).

The forces and moment for Case A are direct measurements. For Case B, the force F_y and

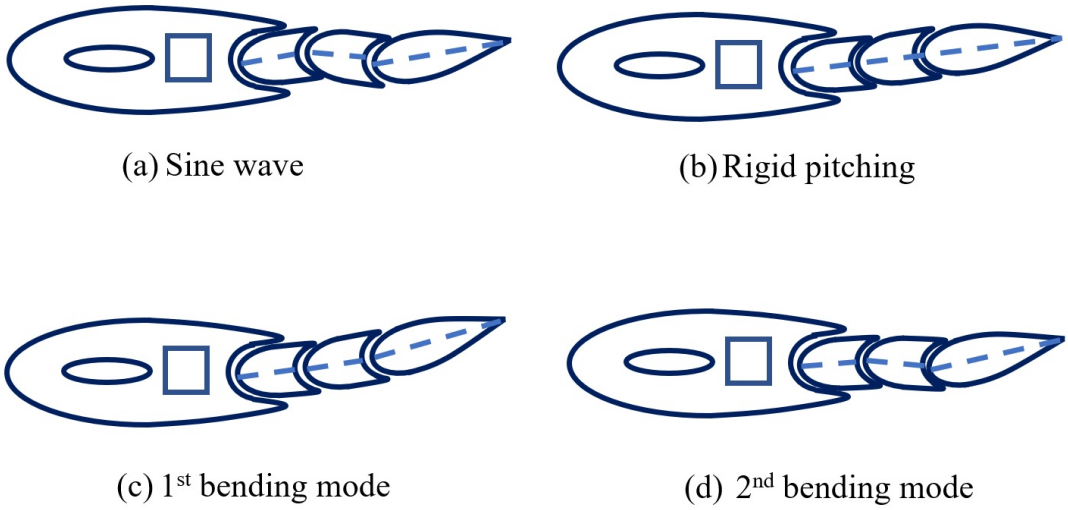

Figure 5.4: Schematic representation of the four swimming gaits for MBE testing.

moment M_z are also direct measurements, but the axial force F_x is the computed *difference* between the measured axial force $F_{x,\text{net}}$ and the drag force D_{body} for the unactuated device at the given steady towing speed:

$$F_x = F_{x,\text{net}} - D_{\text{body}} \tag{5.1}$$

The two intermediate modules and tail, together with the forebody, yield an overall body length of 88 cm. The vertical tail amplitude A_p is measured from the tip of the tail's maximum stroke position relative the centerline of the forebody; A_p is predetermined by measuring the tail peak amplitude against gait inputs provided by LabVIEW. The tail peak amplitudes for all four gaits are tuned so that they measure 4 cm. A summary of the various *MBE* configurations and dynamic operations is given in Table 5.2.

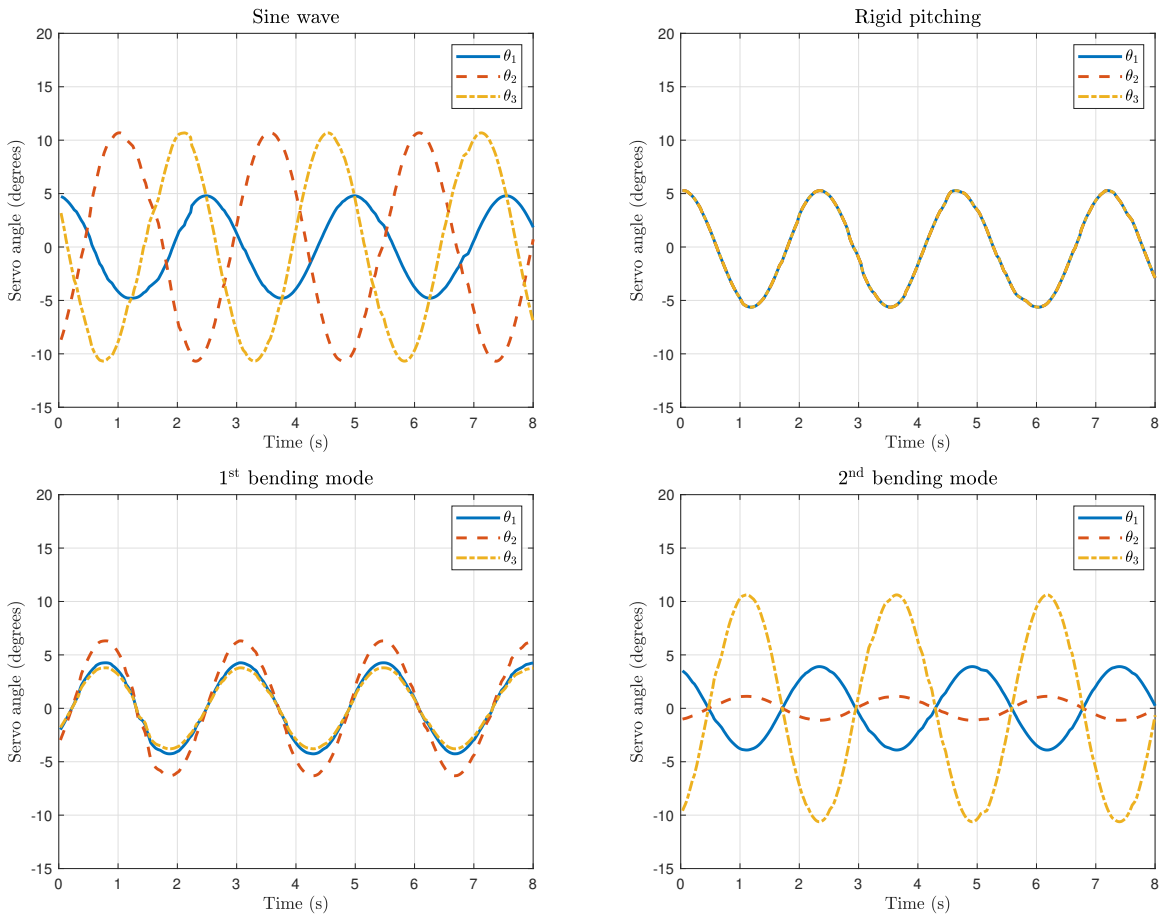

Figure 5.5: Servo angle inputs for sine wave (top left), rigid pitching (top right), 1st bending mode (bottom left) and 2nd bending mode (bottom right). θ_1: solid blue, θ_2: red dashed, θ_3: orange dashed-dot.

Parameter	**Value(s)**
Towing speed, U_∞ (m/s)	$0.13, 0.23$
Reynolds No, Re ($\times 10^5$)	$1.40, 2.33$
Reduced Frequency k	$5.2, 7.7, 10.2$
Frequency, f (Hz)	0.25, 0.38, 0.42, 0.5, 0.63, 0.83
Tail peak amplitude, A_P	≈ 4.0 cm $\pm 1.25\%$
Waveforms (gaits)	sine wave, rigid pitching 1st and 2nd bending modes

Table 5.2: Experiment conditions for testing

5.2 Results and Discussion

The experiments outlined in Table 5.2 were performed in April 2019, yielding data sets for three distinct trials. While it would be impractical to present a comprehensive review of the experimental results, this section provides (1) a discussion of the data associated with representative subsets of test conditions and (2) summary plots of axial force data for all test conditions. All experimental data have been archived and are publicly accessible.[1]

5.2.1 Static Force Measurements

Figure 5.6 shows the body drag force generated when towing the unactuated *MBE* at three different towing speeds. When actuated, the device produces a net axial force that is the thrust minus the body drag. It is difficult or impossible to separate these two components, in practice. Regardless, it is most appropriate to compare the *net* thrust that is generated by the oscillating *MBE* with the unactuated drag force, as the latter is the *least* resistance that would be encountered when propelling the device by more conventional means.

5.2.2 Dynamic Force Measurements - Cases A and B

The selected test conditions that are plotted in Figures 5.7, 5.8 and 5.9 correspond to an *MBE* waveform frequency of 0.42 Hz and three Reynolds numbers: 0, 1.4×10^5, and 2.3×10^5. Figure 5.7 shows the time histories of axial force, side force, and yaw moment for Case A. Recall that there is no forward motion, in this case; the results show the force and moment components generated primarily by the added mass of the displaced fluid around the oscillating members. Figures 5.8 and 5.9 show the time histories of axial force, side

[1] https://sites.google.com/a/vt.edu/biomimetic-locomotion/

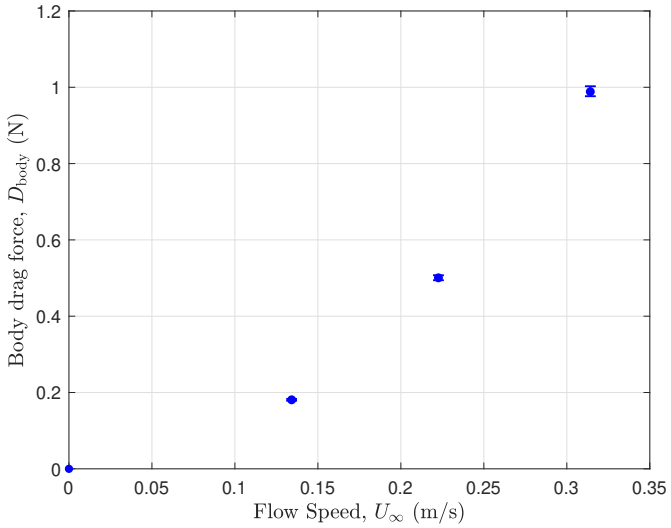

Figure 5.6: Body drag force vs freestream velocity

force, and yaw moment for Case B. In this case, the freestream velocities are $U_\infty = 0.13$ m/s and $U_\infty = 0.23$ m/s. The resultant force and moment components in freestream flow are generated by added mass, and can also include the effects of vorticity and circulation. For all Reynolds numbers, the sine wave gait generates force and moment components with the lowest force amplitude. The rigid pitching gait produces the most significant force amplitude, which is consistent for all test conditions. Between the 1st and 2nd bending mode kinematics, the amplitudes of the responses show little difference in Case A. Still, larger response amplitudes were noted for the 2nd bending mode kinematics in Case B. All gaits at $Re = 2.3 \times 10^5$ result in instantaneous force responses larger than those at $Re = 0$ and Re 1.4×10^5, except for the 1st bending mode. The amplitude response for the 1st bending mode appears to be the largest at $Re = 0$. Since the flow dynamics in Case B involve a combination of added mass, circulation, rotation and three-dimensional effects, the time histories in Case B exhibit stronger non-linear fluctuations. When the flow becomes unsteady, moderate changes of flow velocity around the articulating MBE with respect to time at a

given point give rise to (temporal) flow acceleration. In the case where there are sudden changes in flow velocity, a non-linear characteristic known as convective acceleration builds up. In theory, the convective acceleration is non-linear as the velocity becomes associated with spatial gradients in the flow field. Non-linear fluctuations in the force response are large when the spatial velocity gradients are significant.Besides, at the tested Reynolds numbers, disorderly perturbations in the turbulent flow are superimposed on the force responses, which induce more substantial non-linearity in the flowstream. For those reasons, we notice more significant non-linear force responses in freestream flow than at zero freestream.

In this study, we define the non-dimensional *reduced frequency*

$$k = \frac{\pi f c}{U_{\text{ref}}} \tag{5.2}$$

where U_{ref} is a reference speed (the tail tip velocity U_{tip} for Case A, and the free stream velocity U_∞ for Case B), f is the tail oscillating frequency, and c is a characteristic length, the overall length of the *MBE* (88 cm).

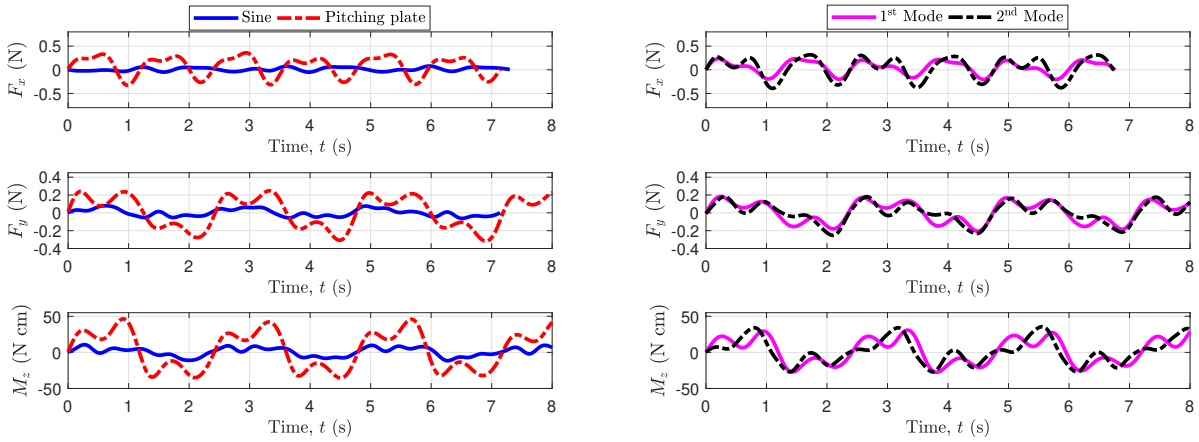

Figure 5.7: Force response for four gaits at flapping frequency f=0.42 Hz. Case A: Reynolds number, $Re = 0$

In the left of Figure 5.10, where the towing speed is zero, note that the mean thrust mono-

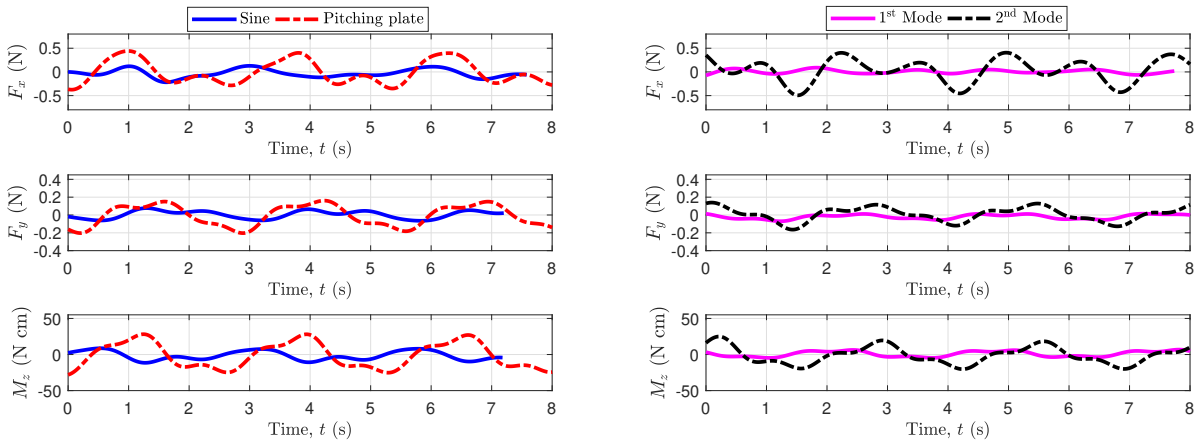

Figure 5.8: Force response for four gaits at flapping frequency f=0.38 Hz. Case B: Reynolds number, $Re = 1.4 \times 10^5$ (left)

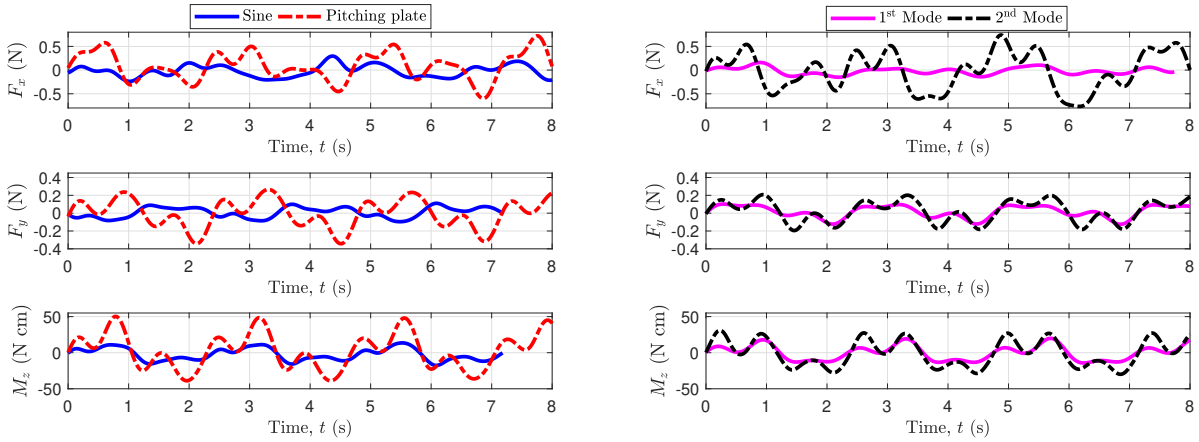

Figure 5.9: Force response for four gaits at flapping frequency f=0.42 Hz. Case B: Reynolds number, $Re = 2.3 \times 10^5$ (left)

tonically increases with increased forcing frequency for the sine wave and the 2nd bending mode kinematics over the range of frequencies tested. For the rigid pitching and 1st bending mode gaits, however, the thrust appears to peak within the range of excitation frequencies. In the right of Figure 5.10, the mean thrust is determined for three frequency inputs at each freestream speed (0.13 m/s and 0.23 m/s). The 1st and 2nd bending mode kinematics generate lower mean thrust forces at higher Reynolds numbers and lower frequencies. In general, at lower frequencies for Case B (nonzero mean flow), the 1st and 2nd bending modes

produce negative thrust. A negative thrust indicates another source of drag in addition to the drag created by the forebody itself. The circulatory effects due to the characteristic of the flapping motion are one reason for the additional source of drag Patil [138]). The excess drag may also be due to wake drag created by large lateral excursions of *MBE* modules for particular gait parameters. The rigid pitching gait should also yield low thrust forces for Case B compared with Case A, as this gait creates the most extensive lateral excursions. However, this gait also produces added mass forces sufficient to overcome the additional drag created in freestream flow. Additionally, regions around the bluff body (faired modules) are susceptible to flow separation due to adverse pressure gradient flow in cases where the faired modules pitch at large amplitudes. Despite the variations between cases A and B, for any given waveform, tail oscillations in zero freestream produce higher mean thrust than in freestream flow.

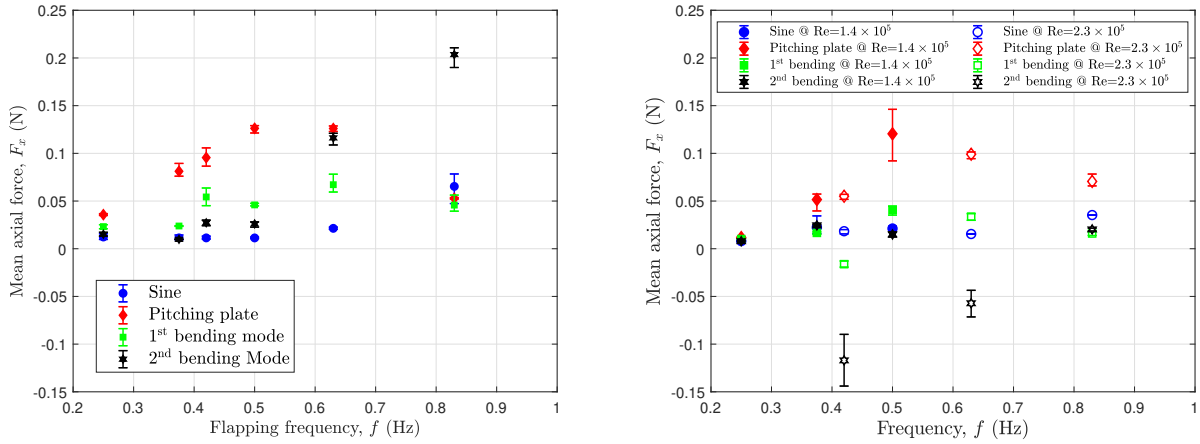

Figure 5.10: Mean axial forces for all test conditions. Case A: Reynolds number, $Re = 0$ (left) and Case B: Both nonzero Reynolds numbers (right). In the right figure, the solid markers represent the results at $Re = 1.4 \times 10^5$ while the hollow markers represent the results at $Re = 2.3 \times 10^5$.

As discussed earlier in chapters 1 and 4, the shedding of a vortex by an oscillating hydrofoil, within a particular range of reduced frequencies, reverses the rotational direction of the

Von-Kármán vortices and induces a jet-like flow in the direction of the free stream. This mechanism is one of the primary sources of forward propulsion. Thrust production by a fish also depends on its morphology and swimming movements. The trailing edge vortices created by the flapping tail during swimming are usually accompanied by a leading-edge vortex of some strength to generate a unique vortex pattern in the wake of the fish. The leading-edge vortex is typically created when the forebody of the fish is at high angles of attack. Since the forebody of the *MBE* is fixed at a zero angle of attack, it is unlikely to generate a leading edge vortex.

However, for particular gait parameters, the leading edge of the faired module can reach up to 10° relative to freestream flow while executing a waveform. A 10° leading edge amplitude is sufficient to produce leading edge vortices at low Strouhal numbers (frequencies) [88]. Furthermore, some of the gait parameters execute a motion where the relative angle between two adjacent faired modules reaches beyond 10°. An example of this gait would be the sine wave, where the relative angle between servos 2 and 3 can reach up to 18° (see Figure 5.5). Also, larger angles between adjacent modules can result in sudden changes in local freestream velocity, which may cause substantial pressure differentials over the faired module that may suggest the formation of body vortices [142].

For this reason, the lateral excursions of the faired modules downstream of the forebody may yield additional shed vortices which serve a similar role to a leading edge vortex in helping to generate forward thrust. The strength of the flow momentum created by the jet produced by a flapping hydrofoil also depends on the incoming flow speed and the strength of the vortices. The incoming flow speed significantly affects the flow-induced force on an object [86]. The effects of the vortices are determined by the proximity of shed vortices to the aft body of the flapping device. The higher the flow speed is, the quicker these vortices advect downstream, resulting in a weaker jet and a lower propulsive reaction force. Nevertheless,

that mechanism is primarily applicable in the presence of freestream flow (Case B).

For the case where a freestream flow is absent, the generation of vorticity is usually the result of viscosity. Vorticity formation is also be dependent on the kinematics of the oscillating members and waveform frequency inputs. As such, the articulating motion of the faired modules can be enough on its own to generate propulsive forces with no freestream [137, 143]. The *MBE* utilizes viscous induced vorticities and is capable of extracting energy from the fluid passively [142].

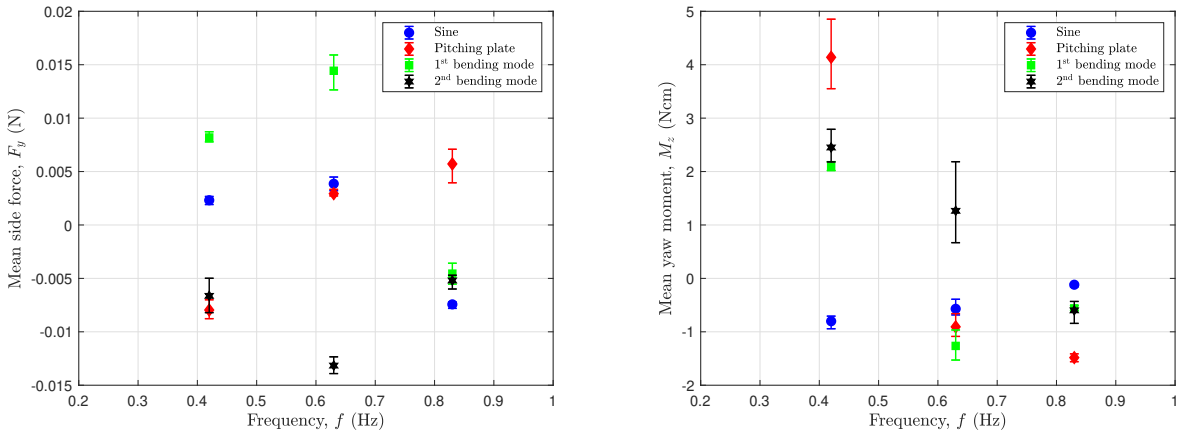

Figure 5.11: Mean side forces (left) and yaw moments (right) for Case A test conditions. Sine wave: blue circle; rigid pitching: red diamond; 1st bending mode: green square; 2nd bending mode: black star.

Figures 5.11, 5.12 and 5.13 present the mean values for the measured side force and yaw moment generated by the *MBE* at Reynolds numbers of 0, 1.4×10^5 and 2.3×10^5, respectively. We can conclude from Figure 5.12 that the side forces monotonically increase with increased frequency, and that the yaw moment monotonically decreases with increased frequency. However, for the most part, the resultant mean side forces and yaw moments for the tested cases in Figures 5.11, 5.12, and 5.13 are relatively close to zero, which is expected when all the gaits are performing symmetric oscillation around a zero mean angle of incidence.

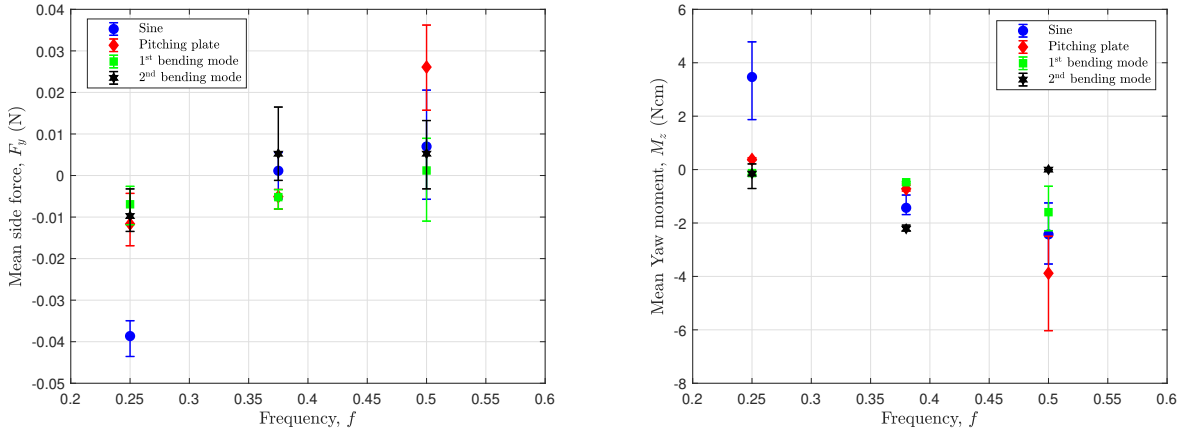

Figure 5.12: Mean side forces and yaw moments for Case B test condition at $Re = 1.4 \times 10^5$. Sine wave: blue circle; rigid pitching: red diamond; 1st bending mode: green square; 2nd bending mode: black star.

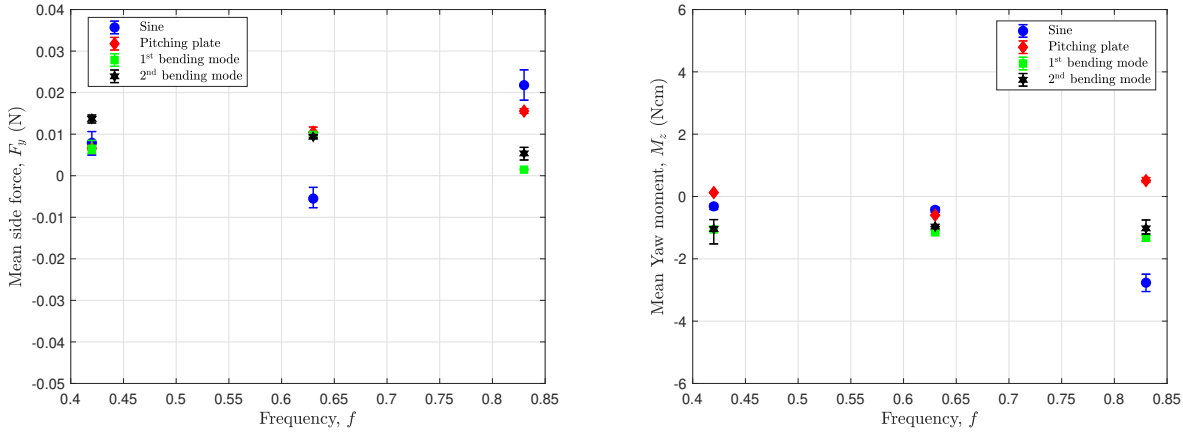

Figure 5.13: Mean side forces and yaw moments for Case B test condition at $Re = 2.3 \times 10^5$. Sine wave: blue circle; rigid pitching: red diamond; 1st bending mode: green square; 2nd bending mode: black star.

Although the results show non-zero forces, we can compute the coefficient forms of side and yaw moments to understand better if the registered non-zero mean forces are physical or based on asymmetrical imperfections.

Figure 5.14 reveals a linear relationship between thrust coefficients and reduced frequency

for both speed of Case B. The effect of waveform frequency input is the most substantial for the 2nd mode bending even when the gait initially produces drag at lower frequencies. Still, the thrust generated increases drastically to overcome the excess drag at higher frequencies. It is important to note that the coefficient of thrust is generated purely by the tail kinematics in freestream flow after taring the body drag. The body drag coefficients noticed at U_∞= 0.13 m/s and U_∞= 0.23 m/s are 0.26 and 0.21, respectively. Statistically, comparisons between the mean thrust and the body drag coefficient reveal that none of the waveforms produce enough thrust to overcome the body drag if the prototype was to swim freely in a flow current of U_∞. I.e., the net axial force is negative.

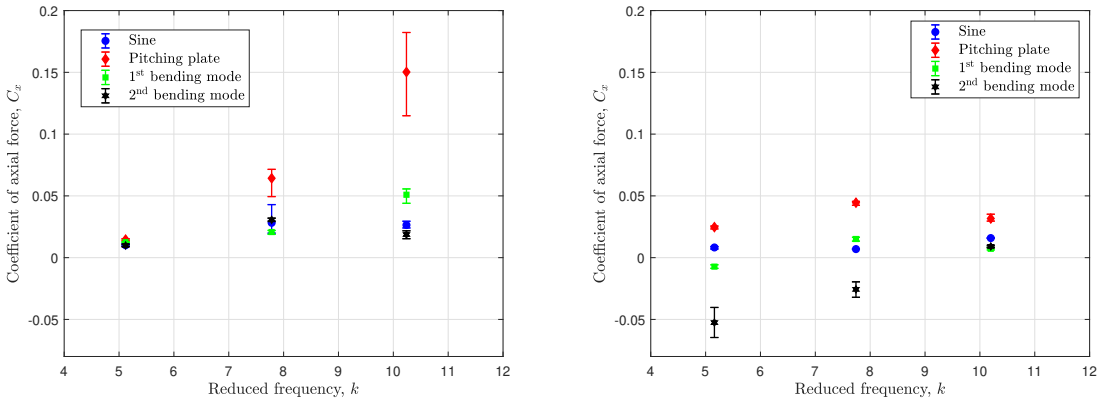

Figure 5.14: Coefficient of axial forces vs reduced frequency for Case B at $Re = 1.4 \times 10^5$ and $Re = 2.3 \times 10^5$.

Figure 5.15 presents the side forces, as well as the yaw moments in coefficient form against reduced frequency for case B only. We can conclude from these sub-figures that there are minute variations in the mean side force and mean yaw moments at $Re = 2.3 \times 10^5$ as nearly all data points display negligible coefficient values. The results at $Re = 1.4 \times 10^5$ show mean side forces larger than the ones produced at $Re = 2.3 \times 10^5$, but they too are statistically small in coefficient value. Theoretically, we do not expect any substantial shift in mean side forces. But even the slightest deviation from the center point will force the flow on one side,

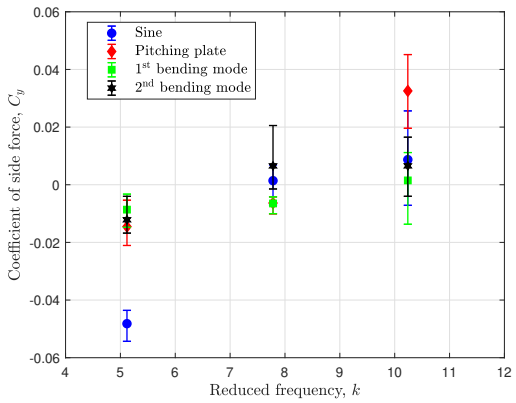

(a) C_y at $Re = 1.4 \times 10^5$.

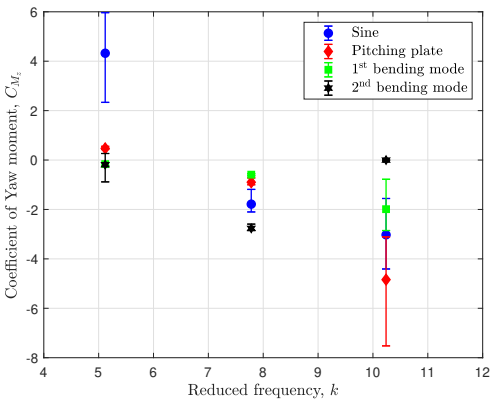

(b) C_{M_z} at $Re = 1.4 \times 10^5$

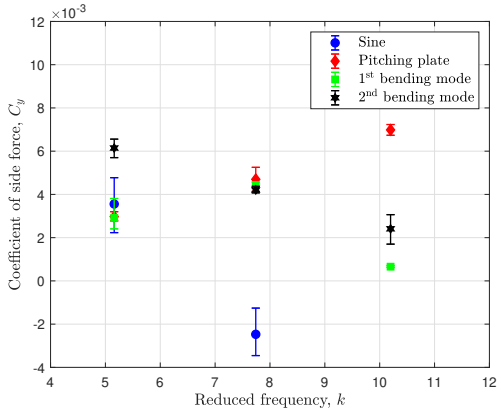

(c) C_y at $Re = 2.3 \times 10^5$

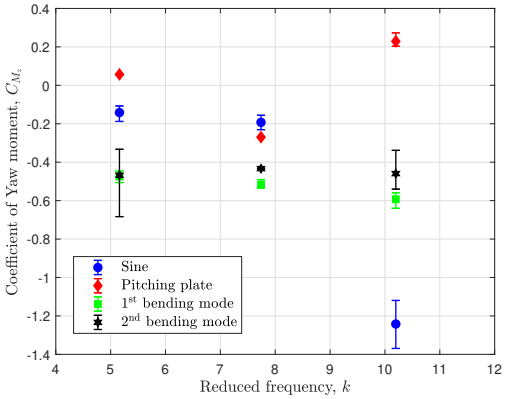

(d) C_{M_z} at $Re = 2.3 \times 10^5$.

Figure 5.15: Coefficient of side forces and yaw moments vs reduced frequency for Case B at $Re = 1.4 \times 10^5$ and $Re = 2.3 \times 10^5$.

resulting in a suction peak (low pressure region).

On the other hand, the presence of relatively sizeable non-zero coefficient mean values can also provide some insight concerning the resultant motion of a freely swimming biological or biomimetic agent. The results also suggest that non-zero coefficients may be a result of a physical flow phenomenon. Even though the device flaps symmetrically in the "upstroke" and "downstroke," some gaits may exhibit significant asymmetric force response. Over a range of frequencies, the vortex street generated can deviate away from the centerline of

the forebody [50, 88], resulting in non-zero side forces and yaw moments. An asymmetric flow response is also possible as the initial conditions of the point of execution may result in uneven body-fluid force interactions between the "upstroke" and "downstroke motions" even if the response reaches steady-state. As a result, a net positive (or negative) side force is possible. The same principle applies to the generated yaw moment.

We further examine the *RMS* values for a few test cases. Figure 5.16 quantifies the *RMS* amplitudes of the forced response generated by all gaits with varying freestream flow. All waveforms produce larger thrust amplitudes with increasing Reynolds number. The results show that the largest thrust amplitudes are caused by the 2^{nd} bending mode and the rigid pitching gaits at $Re = 2.3 \times 10^5$. The results contradict the results for the mean thrust, where a higher mean thrust was observed at lower freestream speeds.

Similarly, the rigid pitching gait generates the highest side force amplitude. Although the rigid pitching and 2^{nd} bending mode produce large force amplitudes, they provide significantly large yaw moments too. In contrast, both 1^{st} mode bending and the sine gaits produce the least yaw moment magnitude at $Re = 2.3 \times 10^5$. For all gaits, a substantial mean yaw moment arises for $Re = 2.3 \times 10^5$ Reynolds numbers. With regards to yaw vehicle stability, the consequence of substantial yaw moments requires considerable autonomous vehicle dynamics and control strategies to deal with extreme out-of-plane maneuvers produced.

Figure 5.17 quantifies the *RMS* amplitudes of the forces and moment responses generated by all gaits with varying waveform frequencies for a given Reynolds number. Among the input frequencies, the rigid pitching produces the most considerable axial force magnitude at $f = 0.5\ Hz$, while the 2^{nd} bending mode provides the least axial force magnitude. When comparing between the 1^{st} and 2^{nd} bending modes, the 2^{nd} bending mode produces significantly larger amplitudes of axial force, but provides little differences in the side force and yaw moment with the 1^{st} bending mode except for at $f = 0.36$ Hz. The least substantial

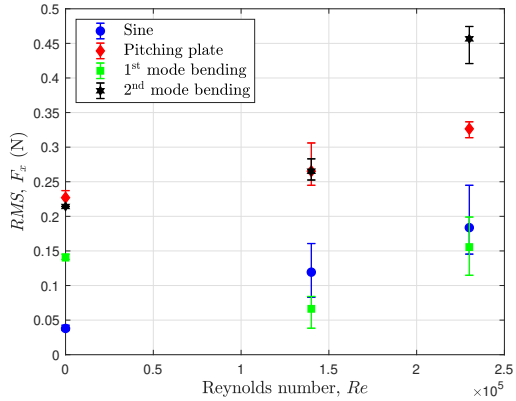

(a) *RMS* axial force

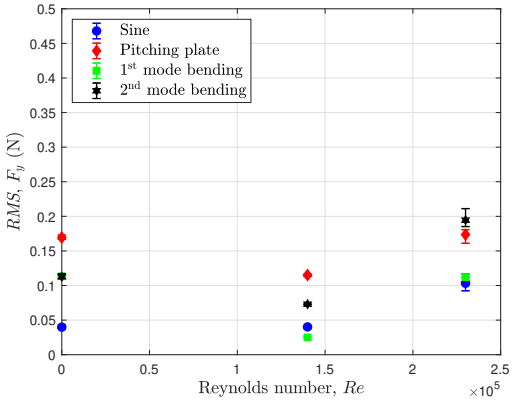

(b) *RMS* side force.

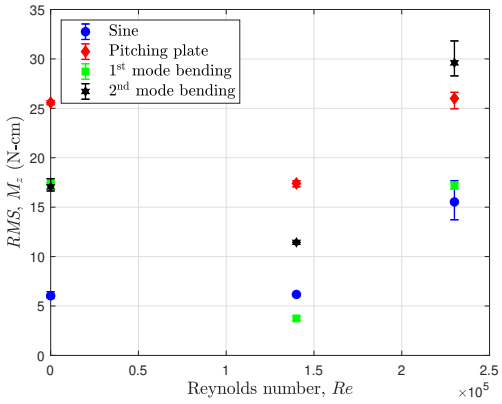

(c) *RMS* yaw moment.

Figure 5.16: Comparison of RMS F_x, F_y, and M_z at Reynolds numbers, $Re = 1.4 \times 10^5$ and $Re = 2.3 \times 10^5$ for the same frequency input (0.4 Hz)

yaw moment is consistently generated by the 1st bending mode at lower frequencies.

Figure 5.18 shows the total servo torque measurements for the three *MBE* modules aft of the forebody for all four gaits at an oscillation frequency of 0.42 Hz. These torque measurements are instantaneous and represent the net torque, $\tau_{i_{\text{net}}}$, required to move the module fairings against hydrodynamic resistance loads. The torques exerted by servos 1 and 2 are generally commensurate and larger than that exerted by servo 3. Rigid flapping is an exception, where servo 1 exerts a far larger control torque, consistent with intuition. When we examine the

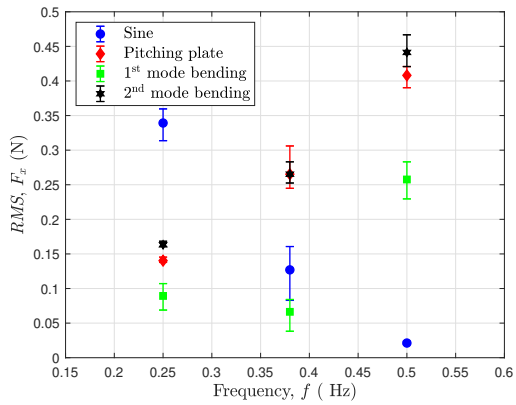

(a) *RMS* axial force

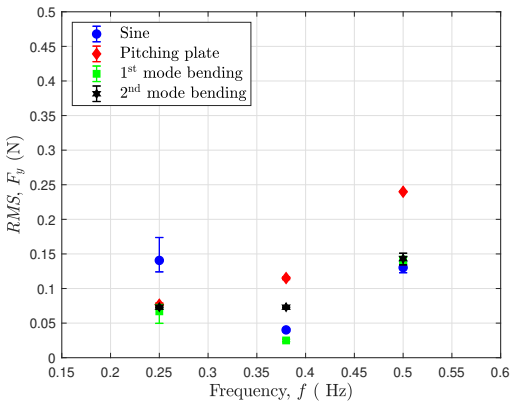

(b) *RMS* side force.

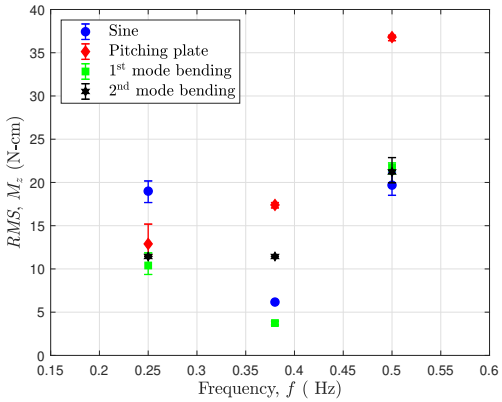

(c) *RMS* yaw moment.

Figure 5.17: Comparison of RMS F_x, F_y, and M_z with frequency of oscillation at Reynolds numbers, $Re = 1.4 \times 10^5$.

magnitudes of the torque responses closely, we notice that out of the four gaits, the sinusoidal gait acquires the lowest torque.

5.3 Summary of Contribution

This chapter provides initial preliminary results on the generated hydrodynamic forces of an articulating body. A modular biolocomotion emulator (*MBE*) designed to generate val-

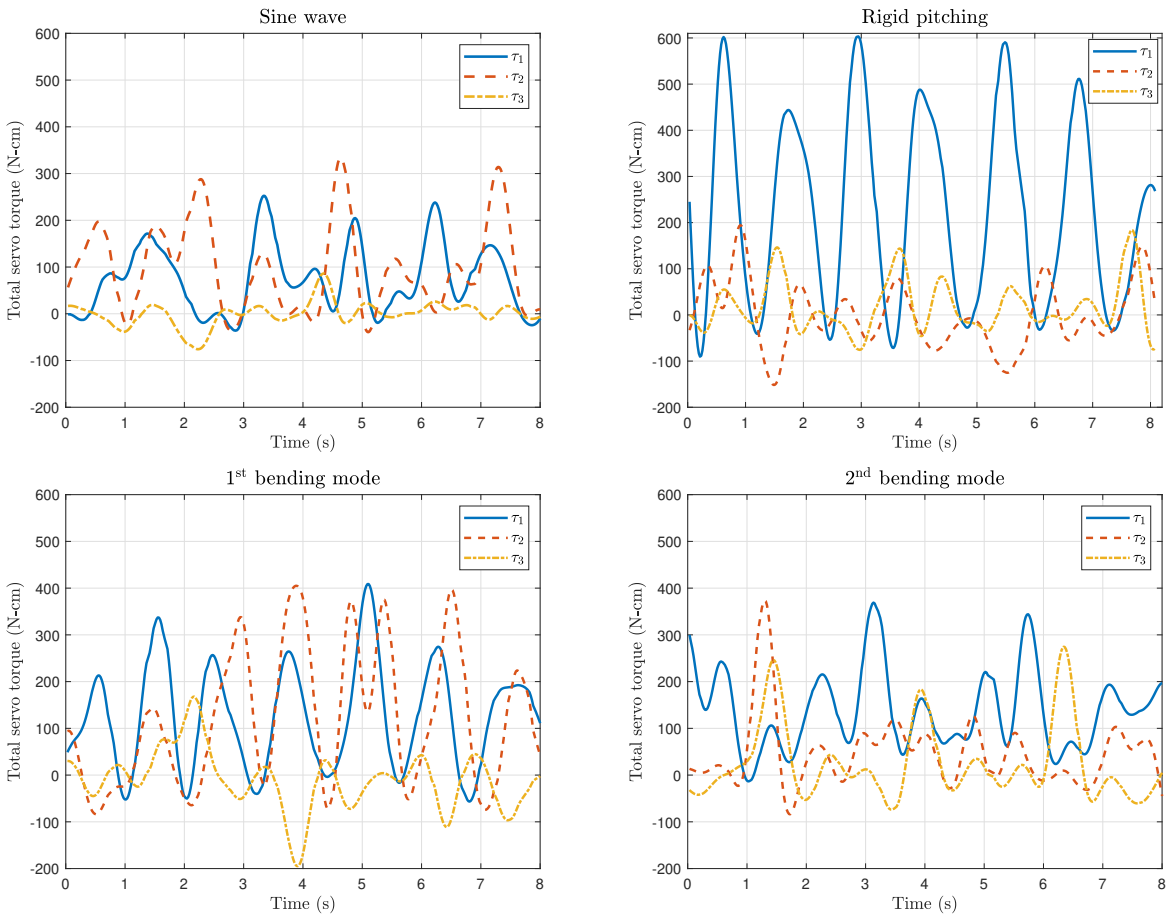

Figure 5.18: Servo torque outputs for sine wave (top left), rigid pitching (top right), 1st bending mode (bottom left) and 2nd bending mode (bottom right). τ_1: solid blue, τ_2: red dashed, τ_3: orange dashed-dot. Test case: U_∞=0 m/s, f=0.42 Hz.

idation data for reduced order computational models of unsteady hydrodynamic forces and moments in biological and biomimetic swimmers has been tested in the Virginia Tech Towing Basin. The experimental program provides quantitative information about the hydrodynamic forces and moments generated as a result of particular waveforms (gaits) and Reynolds numbers over a range of steady towing speeds.

Beyond simply collecting and archiving data for future use, these experiments also provide some insight concerning the hydrodynamic force and moment response of a biomimetic device

to different gaits, with implications for the design analysis of multibody underwater robots.

We isolate the effects of the tail kinematics by taring the body drag from the net axial force measured by the load cell. We found that the gaits without the forebody produce a considerable amount of thrust force. However, these thrust forces were not enough to overcome the body drag. To create a positive net thrust, one would consider scaling down the size of the prototype, forebody, apply more power to achieve higher frequencies or tow at higher speeds.

There are substantial differences between the results presented in zero and non-zero freestream. With no freestream flow, the oscillating tail does not generate the same pattern of shed vortices that would be observed in a steady, non-zero freestream. The rigid pitching gait produces the largest thrust force and peaks within the range of test frequencies. The behavior of axial thrust against frequency is nearly quadratic for the 1^{st} and 2^{nd} bending modes. The thrust force is substantial for the 2^{nd} bending mode at higher frequencies. With freestream flow, between $Re = 1.4 \times 10^5$ and $Re = 2.3 \times 10^5$, the 2^{nd} bending mode gait is the most susceptible to excessive drag production while executing its motion. Higher mean thrust values are achieved at $Re = 1.4 \times 10^5$ flow for a given gait and frequency input. However, large magnitudes of thrust force response is achieved at $Re = 2.3 \times 10^5$.

Since the rigid pitching gait produces the most significant axial force, it is also associated with large instantaneous yaw moment, and large *RMS*. In terms of energy expenditure, the sine wave appears to offer considerably lower torque requirements and provide the least yaw instability. From the *RMS* plots, the sine wave behaves inversely to the increasing frequency at $Re = 2.3 \times 10^5$, which means that a considerable amount of thrust can be achieved at lower frequencies. The large thrust and side forces accompany significant yaw moments. Finally, at higher Reynolds number, the waveform produces substantial magnitudes of yaw moment.

Dye visualization or particle image velocimetry (PIV) results would be a great supplement to the efforts of the current study. To illustrate the applicability of the results in an engineering context, an optimized waveform can be achieved by compromising power requirements, thrust production, and yaw stability control. Understanding the trade-off between the forces and moment components generated can help inform the design and control of autonomous underwater vehicles. The experimental program also offers an exploratory set of results to guide the development of low-order physics-based models for the design of devices and model-based control and estimation algorithms.

5.4 Summary of Major Findings

- The highest generated mean thrust is produced at lower towing speeds, whereas the greatest *RMS* thrust is produced at higher towing speeds.
- Significant mean thrust production can sustain forward swimming operations. In contrast, significant instantaneous thrust production over short time intervals can be utilized for operations that require agility and extreme maneuvering.
- The most substantial mean thrust is generated by the rigid pitching gait at zero freestream flow.
- Both rigid pitching and 2^{nd} bending mode gaits produce the most significant thrust amplitude at large non-zero freestream flow.
- The most significant yaw moment amplitudes are generated by the rigid pitching and 2^{nd} bending mode gaits.

Chapter 6

Conclusion and Future work

6.1 Conclusion

This dissertation presents a parametric repository of experimental data (force and motion time histories) from direct force measurements on single and multi-element airfoils/hydrofoils undergoing unsteady motion. The motive in all chapters is to investigate non-conventional mechanisms that can produce sufficient aerodynamic/hydrodynamic forces for flying and swimming vehicles to perform efficiently at low-to-moderate Reynolds number flow regimes. From chapter 2, we observed enhancement in the generated mean lift and the lift amplitude for trailing-edge flap oscillations about the airfoil's stall angle of attack. In chapter 3, we assessed the aerodynamic forces for sinusoidal and non-sinusoidal angle of attack oscillations of an airfoil. We showed that the 'trapezoidal' pitching generates the largest *RMS* lift coefficient amplitude, and the 'sinusoidal' pitching produced the most substantial increase in the lift to drag ratios. We determined from our third focus in chapter 4 that the effects of tail flexibility on a bio-inspired swimming prototype enhance thrust generation and propulsive efficiencies. The work also briefly investigated the impact of structural resonance on localized propulsive performance and showed that the peak of the thrust force is associated with maximum tail peak amplitude for a flexible tail with a lower aspect ratio (Tail 'c'). We examined in chapter 5 the effects of different tail kinematics (gaits) on hydrodynamic forces and moments generated by an undulating three-link bio-inspired prototype called *Modular*

Biolocomotion Emulator (MBE). We conclude that mean and *RMS* forces and moments respond differently at different towing speeds.

In the first part of chapter 2, we assessed the frequency response on the lift and drag performance of a simple harmonic motion of a trailing edge-flap. A quasi-steady formulation derived from Leishman's model [144] was used to validate the force-time history response from experimental data. Lift predictions from the quasi-steady model agree well with the experimental data for low pitching amplitudes and low reduced frequencies in a fully attached flow. The results revealed that the lift enhancement was observed in two ways: (1) higher generation of mean lift, and (2) improved lift amplitude with increasing frequency. Both events of lift enhancement occurred for TEF oscillations about a nominally stalled 10° mean AoA. Additionally, the lift-to-drag ratios for a dynamic TEF exceeds the quasi-steady lift-to-drag ratio for larger pitching amplitudes at reduced frequencies beyond $k = 0.09$. The frequency response revealed that although higher pitching amplitudes generate the most significant circulatory lift amplitude at higher frequencies, the circulatory lift gain (the dynamic lift amplitude normalized by the quasi-steady lift) is the highest for smaller pitching amplitudes. Hysteresis effects also show no signs of flow separation with TEF pitching around the 10° mean AoA.

Results from chapter 3 determined that an impulse pitch-up airfoil motion of the trapezoidal waveform generates the largest unsteady lift amplitude, and also exceeds the quasi-steady lift value. For the reciprocating motion, an impulse pitch-down airfoil motion produces instantaneous negative drag for short time intervals but does not sustain the negative drag to produce net (mean) drag lower than the quasi-steady value. The enhanced mean lift was observed for all waveforms and is pronounced at higher mean AoAs. An increase in the mean lift was also accompanied by significant jump in the dynamic mean drag relative to the quasi-steady value. The main observation from this research effort is that the trapezoidal

pitching waveform consistently generates the most substantial *RMS* lift amplitude across all mean AoAs, whereas the sinusoidal waveform produces the most significant increase (83%) in the dynamic lift-to-drag ratio relative to the quasi-steady lift-to-drag ratio. This is achieved at post-stall oscillation at 12° mean AoA. Finally, power spectra analysis shows that non-linearity in the lift response contributes significantly to the total lift generated and is a source of lift enhancement at high AoAs. Non-linear fluctuations in the lift response are pronounced for airfoil pitching at 12° mean AoA. The largest contributions of lift from the first and second harmonics are noticed for the reverse sawtooth waveform, which constitute 52% of the total measured lift.

We presented in chapter 4 hydrodynamic forces and torques generated by the tail with varying flexibility on a one-link swimming prototype. The tail executed various frequency inputs and angular leading edge oscillations in zero and non-zero freestream flow. Force and servo torque measurements show that the overall flexibility of the tail enhances the propulsive efficiency. Isolating the effects of aspect ratio and material stiffness, changes in aspect ratio show substantial variation in propulsive efficiencies and the thrust-to-power ratio in zero freestream flow. In contrast, changes in the tail's material stiffness produces a significant effect in propulsive efficiency in non-zero freestream flow. More flexible tails produces thrust peaks at a relatively lower frequency of oscillation whereas a more rigid panel produces greater thrust values at higher frequency inputs. The tail's tip peak amplitudes were observed for panels 'b' and 'c' using video imagery and a motion tracker script. The maximum tail peak amplitude, which is representative of the 1^{st} bending mode, was reported at frequencies of approximately 90% lower than the natural frequency reported by the Euler-Bernoulli beam theory. Finally, the design and instrumentation process of the one-link swimming prototype was aimed to guide the design process of the modular swimming prototype, the (*MBE*).

Chapter 5 presents hydrodynamic forces as well as external and internal moments of the

MBE prototype towed at three different towing speeds, including zero. In addition to the forebody, the three-link modular prototype currently approximates a carrangiform swimmer by executing different tail gaits motion (waveforms) and oscillatory parameters. We concluded that the generated mean thrust is the greatest at lower towing speeds, whereas the *RMS* thrust is the greatest at higher towing speeds for a given gait parameter. Overall, the rigid pitching gait creates the largest mean and RMS thrust forces. Because added mass forces dominate the dynamics of the fluid flow at the currently tested towing speeds, intuitively, the kinematics of rigid pitching gait generates the largest added mass force relative to the other kinematics. The results from this chapter present sufficient preliminary data to understand the hydrodynamic principles of pisciform locomotion. The experimental effort collected over 1,200 data of forces and torque measurements. All data are archived and are publicly accessible through the following link: *https://sites.google.com/a/vt.edu/biomimetic-locomotion/* .

There are two ways to utilize the result from this dissertation. The first is by extending quasi-steady models to obtain accurate and reliable empirical models to predict unsteady forces and moments that can aid the design process of flying or swimming vehicles. The second is to utilize control strategies from frequency response data to design linear and non-linear closed feedback control systems. Flow visualization techniques and computational efforts are welcomed to further support the contributions and the interpretations of the results.

6.2 Future Work

The limitation of the quasi-steady model used for validation in chapter 2 does not incorporate the dynamically varying mean lift and lift amplitude at stalled mean AoAs. As such, a state-space model that captures the changes in the dynamic mean lift is one proposed area

of development. Along with a frequency response that was constructed, a system identified model can also be developed, and a lift deficiency function can be determined to accurately predict the variations in lift amplitude and phase angles between the quasi-steady and unsteady lift responses. Examples of state-space approaches that can incorporate the dynamic flow quantities for unsteady airfoil motion are provided by Leishman and Nguyen [144], and Brunton et al. [145]. The improvement of these methods are essential to support the continuing efforts of low fidelity empirical modeling of unsteady aerodynamics for flapped airfoils at low Reynolds numbers.

There are two mainstreams for future work on the efforts discussed in chapter 3. The first is waveform optimization. By combining more than one waveform into the pitching mechanism, we can utilize the benefits of pitch-up and pitch-down rates during a pitching cycle to achieve improved lift and drag performances. The second is the utilization of averaging theorems on non-sinusoidal lift responses as employed by Bullo and Lewis [146] and Tahmasian et al. [58]. One could explore the use of high-order averaging theory to capture full non-linearities of the unsteady aerodynamic response to determine optimum mean lift to drag coefficient ratios accurately [147].

Results from chapter 4 along with the findings made by Gursul et al. [114] and Wang et al. [148] confirmed that a material's structural resonance plays an important role on thrust enhancement. Other researchers concluded that the resonant frequency of a rectangular panel has no strong implication on thrust production for a given material stiffness and aspect ratio [85]. This hypothesis appears to be interchangeable for different oscillatory parameters, material types and flow regimes. There is no clear conclusion on how the role of structural resonance contributes to the overall thrust production. The disparity in the findings gives rise to another area of future work: to further investigate the effects of structural resonance on the propulsive performance of flexible hydrofoils for a wide spectrum of frequency inputs,

aspect ratios, material stiffness and Reynolds numbers.

There are several potential avenues for future work on the efforts demonstrated in chapter 5. For example, the *MBE* can be extended to include more modules, enabling the simulation of gaits at the anguilliform end of the locomotion spectrum. Also, using feedback control of the internal torques within the *MBE*, one can artificially produce various hydroelastic properties, so that the device can support the study of flexibility effects and hydroelastic tailoring. One can further utilize geometric control theory to improve closed-loop feedback stabilization systems for underwater vehicles. Geometric control and averaging theory can be used to study time-invariant approximations that capture the controlled system's motion over time scales longer than the period of oscillation [149].

An experimentally identified and validated state-space model for unsteady fluid dynamic forces and moments can be determined by first, expressing the 3-D equations of motion for a four-body system (three independently actuated modules/links and the forebody). Secondly, one can accommodate experimental hydrodynamic forces and moments as state variable inputs. Finally, the equation of motions and unsteady hydrodynamic model can be incorporated into a geometric control framework. Geometric control theory that uses open-loop controls for motion generation and closed-loop feedback stabilization can be applied to the final model to determine the control authority of the system.

One can use the experimental data to develop an unsteady hydrodynamic model and examine the control authority of the *MBE*. Explicitly, we can write the equation of motion as:

$$M\big(q\big)\ddot{q} + C\big(q,\dot{q}\big)\dot{q} = Q_{\mathrm{H}} + Q_{\mathrm{C}} \tag{6.1}$$

where q is a system of generalized coordinates in uniform flow, M is the mass matrix that includes translation and rotation rigid body, and added mass inertia, and C matrix represents

the Coriolis and centripetal effects. The generalized external forces include the control inputs, Q_{C}, and the hydrodynamic force responses Q_{H} that are determined from experimental results. The reader is referred to Appendix C for more details.

Raw data from the experiments were made accessible to the public for continued research activity in the areas of hydrodynamic modeling and control. The experiments were recommendation made by prior efforts on gait morphology (Allen [150]), and geometric control of underwater autonomous vehicle (Kelasidi et al. [67] and Morgansen et al. [80]). Detailed hydrodynamic analysis and validation of unsteady vortex lattice method (UVLM) are continuing research efforts. Currently, a second version of the *MBE* is under design and construction at the Non-linear System (NSL) Laboratory in Virginia Tech and anticipates testing at the Davidson Laboratory's towing tank facility in Stevens Institute of Technology around Spring 2020 to accommodate for higher swimming speeds and improved fidelity of system actuation.

Bibliography

[1] H. Wagner. Uber die entstehung des dynamischen auftriebes von traflgugeln. *Zeitschrift fur Angewandte Mathematic und Mechanik*, 35:17, 1925.

[2] O. K. G. Tietjens and L. Prandtl. *Applied hydro-and aeromechanics: based on lectures of L. Prandtl*. Courier Dover Publications, 1957.

[3] Theodore Theodorsen and WH Mutchler. General theory of aerodynamic instability and the mechanism of flutter. 1935.

[4] I. E. Garrick. On some reciprocal relations in the theory of nonstationary flows. Technical Report 629, NACA, 1938.

[5] Haithem E Taha, Muhammad R Hajj, and Philip S Beran. State-space representation of the unsteady aerodynamics of flapping flight. *Aerospace Science and Technology*, 34:1–11, 2014.

[6] Haithem Taha and Amir S Rezaei. Viscous extension of potential-flow unsteady aerodynamics: the lift frequency response problem. *Journal of Fluid Mechanics*, 868:141–175, 2019.

[7] S. L. Brunton and C. W. Rowley. Empirical state-space representations for theodorsen's lift model. *Journal of Fluids and Structures*, 38:174–186, 2013.

[8] J Gordon Leishman. Unsteady lift of a flapped airfoil by indicial concepts. *Journal of Aircraft*, 31(2):288–297, 1994.

[9] Balusu M Rao, Brian Maskew, and FA Dvorak. Theoretical prediction of dynamic stall on oscillating airfoils. *American Helicopter Society Paper*, 78:62, 1978.

[10] K. Ramesh, A. Gopalarathnam, J. R. Edwards, M. V. Ol, and K. Granlund. An unsteady airfoil theory applied to pitching motions validated against experiment and computation. *Theoretical and Computational Fluid Dynamics*, pages 1–22, 2013.

[11] David Rival and Cam Tropea. Characteristics of pitching and plunging airfoils under dynamic-stall conditions. *Journal of Aircraft*, 47(1):80–86, 2010.

[12] David James Cleaver, Z Wang, and I Gursul. Bifurcating flows of plunging aerofoils at high strouhal numbers. *Journal of Fluid Mechanics*, 708:349–376, 2012.

[13] MY Zakaria, HE Taha, and MR Hajj. Measurement and modeling of lift enhancement on plunging airfoils: A frequency response approach. *Journal of Fluids and Structures*, 69:187–208, 2017.

[14] Mohamed Y Zakaria, Haithem E Taha, Muhammad R Hajj, and Ahmed A Hussein. Experimental-based unified unsteady nonlinear aerodynamic modeling for two-dimensional airfoils. In *33rd AIAA Applied Aerodynamics Conference*, page 3167, 2015.

[15] Mohamed Y Zakaria, Haithem E Taha, and Muhammad R Hajj. Experimental investigations of the lift frequency response at high angles of attack. In *53rd AIAA Aerospace Sciences Meeting*, page 1503, 2015.

[16] Yeon Sik Baik, Jonathan Rausch, Luis P Bernal, Wei Shyy, and Michael V Ol. Experimental study of governing parameters in pitching and plunging airfoil at low reynolds number. In *48th AIAA aerospace sciences meeting including the new horizons forum and aerospace exposition*, pages 2010–388, 2010.

[17] Martiqua L Post and Thomas C Corke. Separation control using plasma actuators: dynamic stall vortex control on oscillating airfoil. *AIAA journal*, 44(12):3125–3135, 2006.

[18] Lars E Ericsson and J Peter Reding. Dynamic stall analysis in light of recent numerical and experimental results. *Journal of Aircraft*, 13(4):248–255, 1976.

[19] Z. Wang. Vortex shedding and frequency selection in flapping flight. *Journal of Fluid Mechanics*, 410:323–341, 2000.

[20] Dong-Ha Kim and Jo-Won Chang. Unsteady boundary layer for a pitching airfoil at low reynolds numbers. *Journal of mechanical science and technology*, 24(1):429–440, 2010.

[21] Miguel R Visbal. High-fidelity simulation of transitional flows past a plunging airfoil. *AIAA journal*, 47(11):2685–2697, 2009.

[22] AP Broeren and MB Bragg. Flowfield measurements over an airfoil during natural low-frequency oscillations near stall. *AIAA Journal*, 37(1):130–132, 1999.

[23] YW Jung and SO Park. Vortex-shedding characteristics in the wake of an oscillating airfoil at low reynolds number. *Journal of Fluids and Structures*, 20(3):451–464, 2005.

[24] Mohamed Y Zakaria, Farid Jafari, and Muhammad R Hajj. Piv measurements of a plunging airfoil at high angles of attack. In *32nd AIAA Aerodynamic Measurement Technology and Ground Testing Conference*, page 3401, 2016.

[25] Kenneth W McAlister, Lawrence W Carr, and William J McCroskey. Dynamic stall experiments on the naca 0012 airfoil. 1978.

[26] WJ McCroskey. The phenomenon of dynamic stall. Technical report, DTIC Document, 1981.

[27] JG Leishman and TS Beddoes. A semi-empirical model for dynamic stall. *Journal of the American Helicopter society*, 34(3):3–17, 1989.

[28] CW Pitt Ford and Holger Babinsky. Lift and the leading-edge vortex. *Journal of Fluid Mechanics*, 720:280–313, 2013.

[29] David James Cleaver, Zhijin Wang, Ismet Gursul, and MR Visbal. Lift enhancement by means of small-amplitude airfoil oscillations at low reynolds numbers. *AIAA journal*, 49(9):2018–2033, 2011.

[30] Edward C Polhamus. *A concept of the vortex lift of sharp-edge delta wings based on a leading-edge-suction analogy*. National Aeronautics and Space Administration, 1966.

[31] John E Lamar. Extension of leading-edge-suction analogy to wings with separated flow around the side edges at subsonic speeds. 1974.

[32] Angelo Iollo and Luca Zannetti. Optimal control of a vortex trapped by an airfoil with a cavity. *Flow, turbulence and combustion*, 65(3-4):417–430, 2000.

[33] Shengxian Shi, TH New, and Yingzheng Liu. On the flow behaviour of a vortex-trapping cavity naca0020 aerofoil at ultra-low reynolds number.

[34] RM Rennie and Eric J Jumper. Experimental measurements of dynamic control surface effectiveness. *Journal of aircraft*, 33(5):880–887, 1996.

[35] Daniel Feszty, Eric A Gillies, and Marco Vezza. Alleviation of airfoil dynamic stall moments via trailing-edge flap flow control. *AIAA journal*, 42(1):17–25, 2004.

[36] R Åke Norberg. Swallow tail streamer is a mechanical device for self-deflection of tail leading edge, enhancing aerodynamic efficiency and flight manoeuvrability. *Proc. R. Soc. Lond. B*, 257(1350):227–233, 1994.

[37] Avi Seifert, David Greenblatt, and Israel J Wygnanski. Active separation control: an overview of reynolds and mach numbers effects. *Aerospace Science and Technology*, 8 (7):569–582, 2004.

[38] R Kawamura and Y Aihara. *Fluid dynamics of high angle of attack*. Springer-Verlag, 1993.

[39] Chengyu Li, Haibo Dong, and Geng Liu. Effects of a dynamic trailing-edge flap on the aerodynamic performance and flow structures in hovering flight. *Journal of Fluids and Structures*, 58:49–65, 2015.

[40] T. Y. Wu. A nonlinear theory for a flexible unsteady wing. *Journal of Engineering Mathematics*, 58:279–287, 2007.

[41] Albert Medina and Maziar Hemati. Separated flow response to rapid flap deflection. In *2018 AIAA Aerospace Sciences Meeting*, page 0574, 2018.

[42] Min Xu, Mingjun Wei, Chengyu Li, and Haibo Dong. Adjoint-based optimization of flapping plates hinged with a trailing-edge flap. *Theoretical and Applied Mechanics Letters*, 5(1):1–4, 2015.

[43] Samuel Greenhalgh. Oscillating flap lift enhancement device, March 23 1999. US Patent 5,884,872.

[44] Samuel Greenhalgh. Lift enhancement due to unsteady aerodynamics. In *11th Applied Aerodynamics Conference*, page 3538.

[45] Tim Lee and Panayiote Gerontakos. Dynamic stall flow control via a trailing-edge flap. *AIAA journal*, 44(3):469–480, 2006.

[46] P Gerontakos and T Lee. Piv study of flow around unsteady airfoil with dynamic trailing-edge flap deflection. *Experiments in fluids*, 45(6):955–972, 2008.

[47] Tim Lee. Effect of flap motion on unsteady aerodynamic loads. *Journal of aircraft*, 44 (1):333–337, 2007.

[48] Albert Medina and Matthew Rockwood. On the response of leading-edge phenomena and near-wake formations to trailing-edge flap actuation. In *10th International Micro Air Vehicle Competition and Conference*, pages 07–10, 2018.

[49] Michael Ol, Haibo Dong, and Charles Webb. Motion kinematics vs. angle of attack effects in high-frequency airfoil pitch/plunge. In *38th Fluid Dynamics Conference and Exhibit*, page 3822, 2008.

[50] Manoochehr M Koochesfahani. Vortical patterns in the wake of an oscillating airfoil. *AIAA journal*, 27(9):1200–1205, 1989.

[51] Jeff Eldredge, Chengjie Wang, and Michael Ol. A computational study of a canonical pitch-up, pitch-down wing maneuver. In *39th AIAA fluid dynamics conference*, page 3687, 2009.

[52] Rakib I Zaman, Joseph Lai, John Young, and Muhammad Ashraf. Comparison study of non sinusoidal pitch over sinusoidal pitch at higher angle of attack. In *32nd AIAA Applied Aerodynamics Conference*, page 2016, 2014.

[53] Qing Xiao and Wei Liao. Numerical study of asymmetric effect on a pitching foil. *International Journal of Modern Physics C*, 20(10):1663–1680, 2009.

[54] D. Zhang K. Lu, Y.H. Xie. Numerical investigations into the nonsinusoidal motion effects on aerodynamics of a pitching airfoil. The 6th International Conference on Applied Energy – ICAE2014, 2014.

[55] D. Zhang K. Lu, Y.H. Xie. Numerical study of large amplitude, non-sinusoidal motion and camber effects on pitching airfoil propulsion. *Journal of Fluid and Structures*, 36: 184–1945, 2013.

[56] Hongyin Zhao Liming Chao Yonghui Cao, Junnan Meng. Study of motion pattern effects on pitching flappingfoil hydrodynamic. 2016 International Conference on Advanced Robotics and Mechatronics (ICARM), 2016.

[57] Frank M Bos, David Lentink, BW Van Oudheusden, and Hester Bijl. Influence of wing kinematics on aerodynamic performance in hovering insect flight. *Journal of fluid mechanics*, 594:341–368, 2008.

[58] Sevak Tahmasian, David W Allen, and Craig A Woolsey. On averaging and input optimization of high-frequency mechanical control systems. *Journal of Vibration and Control*, 24(5):937–955, 2018.

[59] Paul W Webb. Hydrodynamics and energetics of fish propulsion. *Bulletin of the fisheries research board of Canada*, 190:1–159, 1975.

[60] Daniel Weihs. Design features and mechanics of axial locomotion in fish. *American Zoologist*, 29(1):151–160, 1989.

[61] Paul W Webb. The biology of fish swimming. *Mechanics and Physiology of Animal Swimming*, 4562, 1994.

[62] Michael Sfakiotakis, David M Lane, and J Bruce C Davies. Review of fish swimming modes for aquatic locomotion. *IEEE Journal of oceanic engineering*, 24(2):237–252, 1999.

[63] Eva Kanso, Jerrold E Marsden, Clarence W Rowley, and Juan B Melli-Huber. Locomotion of articulated bodies in a perfect fluid. *Journal of Nonlinear Science*, 15(4): 255–289, 2005.

[64] Kristi A Morgansen, Benjamin I Triplett, and Daniel J Klein. Geometric methods

for modeling and control of free-swimming fin-actuated underwater vehicles. *IEEE Transactions on Robotics*, 23(6):1184–1199, 2007.

[65] Richard Mason and Joel W Burdick. Experiments in carangiform robotic fish locomotion. In *Robotics and Automation, 2000. Proceedings. ICRA'00. IEEE International Conference on*, volume 1, pages 428–435. IEEE, 2000.

[66] Pål Liljebäck, Kristin Ytterstad Pettersen, Øyvind Stavdahl, and Jan Tommy Gravdahl. *Snake robots: modelling, mechatronics, and control*. Springer Science & Business Media, 2012.

[67] Eleni Kelasidi, Kristin Ytterstad Pettersen, Jan Tommy Gravdahl, and Pål Liljebäck. Modeling of underwater snake robots. In *2014 IEEE International Conference on Robotics and Automation (ICRA)*, pages 4540–4547. IEEE, 2014.

[68] Anna M Kohl, Kristin Ytterstad Pettersen, Eleni Kelasidi, and Jan Tommy Gravdahl. Planar path following of underwater snake robots in the presence of ocean currents. *IEEE Robotics and Automation Letters*, 1(1):383–390, 2016.

[69] Paul W Webb and Daniel Weihs. Functional locomotor morphology of early life history stages of fishes. *Transactions of the American Fisheries Society*, 115(1):115–127, 1986.

[70] Christophe Eloy. Optimal strouhal number for swimming animals. *Journal of Fluids and Structures*, 30:205–218, 2012.

[71] J Katz and D Weihs. Behavior of vortex wakes from oscillating airfoils. *Journal of Aircraft*, 15(12):861–863, 1978.

[72] Meliha Bozkurttas, Haibo Dong, Rajat Mittal, Peter Madden, and George Lauder. Hydrodynamic performance of deformable fish fins and flapping foils. In *44th AIAA Aerospace Sciences Meeting and Exhibit*, page 1392, 2006.

[73] DS Barrett, MS Triantafyllou, DKP Yue, MA Grosenbaugh, and MJ Wolfgang. Drag reduction in fish-like locomotion. *Journal of Fluid Mechanics*, 392:183–212, 1999.

[74] Eric D Tytell and George V Lauder. The hydrodynamics of eel swimming: I. wake structure. *Journal of Experimental Biology*, 207(11):1825–1841, 2004.

[75] Michael S Triantafyllou, GS Triantafyllou, and DKP Yue. Hydrodynamics of fishlike swimming. *Annual Review of Fluid Mechanics*, 32(1):33–53, 2000.

[76] Eliot G Drucker and George V Lauder. A hydrodynamic analysis of fish swimming speed: wake structure and locomotor force in slow and fast labriform swimmers. *Journal of Experimental Biology*, 203(16):2379–2393, 2000.

[77] Ulrike K Müller, Joris Smit, Eize J Stamhuis, and John J Videler. How the body contributes to the wake in undulatory fish swimming: flow fields of a swimming eel (anguilla anguilla). *Journal of Experimental Biology*, 204(16):2751–2762, 2001.

[78] William W Schultz and Paul W Webb. Power requirements of swimming: Do new methods resolve old questions? *Integrative and Comparative Biology*, 42(5):1018–1025, 2002.

[79] Scott D Kelly, Richard J Mason, Carl T Anhalt, Richard M Murray, and Joel W Burdick. Modelling and experimental investigation of carangiform locomotion for control. In *American Control Conference, 1998. Proceedings of the 1998*, volume 2, pages 1271–1276. IEEE, 1998.

[80] Kristi A Morgansen, V Duidam, Richard J Mason, Joel W Burdick, and Richard M Murray. Nonlinear control methods for planar carangiform robot fish locomotion. In *Robotics and Automation, 2001. Proceedings 2001 ICRA. IEEE International Conference on*, volume 1, pages 427–434. IEEE, 2001.

[81] P. A. Vela, K. A. Morgansen, and J. W. Burdick. Underwater locomotion from oscillatory shape deformations. In *Proc. IEEE Conference on Decision and Control*, volume 2, pages 2074–2080, Las Vegas, NV, December 2002.

[82] Patricio A Vela, Kristi A Morgansen, and Joel W Burdick. Second order averaging methods for oscillatory control of underactuated mechanical systems. In *American Control Conference, 2002. Proceedings of the 2002*, volume 6, pages 4672–4677. IEEE, 2002.

[83] F. Bullo. Averaging and vibrational control of mechanical systems. *SIAM Journal on Control and Optimization*, 41(2):542–562, 2002.

[84] Wei Shyy, Peter Ifju, and Dragos Viieru. Membrane wing-based micro air vehicles. *Applied mechanics reviews*, 58(4):283–301, 2005.

[85] Peter A Dewey, Birgitt M Boschitsch, Keith W Moored, Howard A Stone, and Alexander J Smits. Scaling laws for the thrust production of flexible pitching panels. *Journal of Fluid Mechanics*, 732:29–46, 2013.

[86] Daniel B Quinn, George V Lauder, and Alexander J Smits. Scaling the propulsive performance of heaving flexible panels. *Journal of fluid mechanics*, 738:250–267, 2014.

[87] Mehdi Ghommem, Muhammad R Hajj, Philip S Beran, and Ishwar K Puri. Role of wing morphing in thrust generation. *Theoretical and Applied Mechanics Letters*, 4(3): 032003, 2014.

[88] JM Anderson, K Streitlien, DS Barrett, and MS Triantafyllou. Oscillating foils of high propulsive efficiency. *Journal of Fluid Mechanics*, 360:41–72, 1998.

[89] GS Triantafyllou, MS Triantafyllou, and MA Grosenbaugh. Optimal thrust develop-

ment in oscillating foils with application to fish propulsion. *Journal of Fluids and Structures*, 7(2):205–224, 1993.

[90] George V Lauder and Peter GA Madden. Fish locomotion: kinematics and hydrodynamics of flexible foil-like fins. *Experiments in Fluids*, 43(5):641–653, 2007.

[91] P Prempraneerach, FS Hover, and Michael S Triantafyllou. The effect of chordwise flexibility on the thrust and efficiency of a flapping foil. In *Proc. 13th Int. Symp. on Unmanned Untethered Submersible Technology: special session on bioengineering research related to autonomous underwater vehicles, New Hampshire*, volume 152, pages 152–170, 2003.

[92] C-K Kang, Hikaru Aono, Carlos ES Cesnik, and Wei Shyy. Effects of flexibility on the aerodynamic performance of flapping wings. *Journal of fluid mechanics*, 689:32–74, 2011.

[93] Sam Heathcote and Ismet Gursul. Flexible flapping airfoil propulsion at low reynolds numbers. *AIAA journal*, 45(5):1066–1079, 2007.

[94] Peter Ifju, Martin Waszak, and Luther Jenkins. Stability and control properties of an aeroelastic fixed wing micro aerial vehicle. In *AIAA atmospheric flight mechanics conference and exhibit*, page 4005, 2001.

[95] Wei Shyy, Richard Smith, Wei Shyy, and Richard Smith. A study of flexible airfoil aerodynamics with application to micro aerial vehicles. In *28th Fluid Dynamics Conference*, page 1933, 1997.

[96] Pinunta Rojratsirikul, Zhijin Wang, and Ismet Gursul. Unsteady aerodynamics of membrane airfoils. In *46th AIAA Aerospace Sciences Meeting and Exhibit*, page 613, 2008.

[97] LE Ericsson and JP Reding. Fluid mechanics of dynamic stall part i. unsteady flow concepts. *Journal of fluids and structures*, 2(1):1–33, 1988.

[98] Amir S Rezaei and Haitham E Taha. Computational study of lift frequency responses of pitching airfoils at low reynolds numbers. In *55th AIAA Aerospace Sciences Meeting*, page 0716, 2017.

[99] Hisham Shehata, Mohamed Zakaria, Ahmed Hussein, and Muhammad R Hajj. Aerodynamic analysis of flapped airfoil at high angles of attack. In *2018 AIAA Aerospace Sciences Meeting*, page 0037, 2018.

[100] Alan Pope and John J Harper. Low speed wind tunnel testing. *New York*, 1966.

[101] Hugh W Coleman and W Glenn Steele. *Experimentation, Validation, and Uncertainty Analysis for Engineers*. John Wiley & Sons, 2018.

[102] E.V Laitone. Wind tunnel tests of wings at reynolds numbers below 70000. *Experiments in Fluids*, 23:405–409, 1997.

[103] Md Mahbub Alam, Y Zhou, HX Yang, H Guo, and J Mi. The ultra-low reynolds number airfoil wake. *Experiments in Fluids*, 48(1):81–103, 2010.

[104] S Martínez-Aranda, AL García-González, L Parras, JF Velázquez-Navarro, and C Del Pino. Comparison of the aerodynamic characteristics of the naca0012 airfoil at low-to-moderate reynolds numbers for any aspect ratio. *International Journal of Aerospace Sciences*, 4(1):1–8, 2016.

[105] Hieu T Ngo and Lisa E Barlow. Lifting surface with active variable tip member and method for influencing lifting surface behavior therewith, May 28 2002. US Patent 6,394,397.

[106] Samantha Gildersleeve, Dan Clingman, and Michael Amitay. Separation control over a flapped naca 0012 model using an array of low aspect ratio cylindrical pins. In *8th AIAA Flow Control Conference*, page 4088, 2016.

[107] John William Strutt Baron Rayleigh. *The theory of sound*, volume 2. Macmillan, 1896.

[108] Mohamed Y. Zakaria. Low to medium fidelity models for unsteady pitching maneuvers at low reynolds number. 2018 AIAA Aerospace Sciences Meeting, 2019.

[109] EV Laitone. Wind tunnel tests of wings at reynolds numbers below 70 000. *Experiments in Fluids*, 23(5):405–409, 1997.

[110] R. L. Bisplinghoff, H. Ashley, and R. L. Halfman. *Aeroelasticity*. Dover Publications, New York, 1996.

[111] W. Shyy, Y. Lian, J. Tang, D. Viiero, and H. Liu. *Aerodynamics of Low Reynolds Number Flyers*. Cambridge University Press, 2008.

[112] D Poirel, Y Harris, and A Benaissa. Self-sustained aeroelastic oscillations of a naca0012 airfoil at low-to-moderate reynolds numbers. *Journal of Fluids and Structures*, 24(5): 700–719, 2008.

[113] Michael V Ol, Luis Bernal, Chang-Kwon Kang, and Wei Shyy. Shallow and deep dynamic stall for flapping low reynolds number airfoils. In *Animal Locomotion*, pages 321–339. Springer, 2010.

[114] I Gursul, DJ Cleaver, and Z Wang. Control of low reynolds number flows by means of fluid–structure interactions. *Progress in Aerospace Sciences*, 64:17–55, 2014.

[115] Leonardo Bergami, Vasilis A Riziotis, and Mac Gaunaa. Aerodynamic response of an airfoil section undergoing pitch motion and trailing edge flap deflection: a comparison of simulation methods. *Wind Energy*, 18(7):1273–1290, 2015.

[116] Hisham Shehata, Mohamed Y Zakaria, Muhammad R Hajj, and Craig A Woolsey. Aerodynamic response of a naca-0012 airfoil undergoing non-sinusoidal pitching waveforms. In *AIAA Scitech 2019 forum*, page 0303, 2019.

[117] Philip Beran Haithem Taha, Muhammad Hajj. State-space representation of the unsteady aerodynamics of flapping flight. *Aerospace Science and Technology*, 34:1–11, 2014.

[118] David Lentink, GertJan F Van Heijst, Florian T Muijres, and Johan L Van Leeuwen. Vortex interactions with flapping wings and fins can be unpredictable. *Biology Letters*, 2010. doi: 10.1098/rsbl.2009.0806.

[119] JM Martin, RW Empey, WJ McCroskey, and FX Caradonna. An experimental analysis of dynamic stall on an oscillating airfoil. *Journal of the American Helicopter Society*, 19(1):26–32, 1974.

[120] Jie-Zhi Wu, Xi-Yun Lu, Andrew G Denny, Meng Fan, and Jain-Ming Wu. Post-stall flow control on an airfoil by local unsteady forcing. *Journal of Fluid Mechanics*, 371: 21–58, 1998.

[121] Gustav Kirchhoff. Ueber die auflösung der gleichungen, auf welche man bei der untersuchung der linearen vertheilung galvanischer ströme geführt wird. *Annalen der Physik*, 148(12):497–508, 1847.

[122] A Choudhry, M Arjomandi, and R Kelso. Lift curve breakdown for airfoil undergoing dynamic stall. In *Proceedings of the 19th Australasian Fluid Mechanics Conference', Melbourne, Australia*, 2014.

[123] M Ol. High-frequency, high-amplitude pitch problem: Airfoils, plates, and wings. In *39th AIAA Fluid Dynamics Conference*, page 3686, 2009.

[124] Adrian S. Nastase Mastering Electronics Design. How to derive the rms value of a trapezoidal waveform, 2018. URL https://masteringelectronicsdesign.com/how-to-derive-the-rms-value-of-a-trapezoidal-waveform/.

[125] Mastering Electronics Design Adrian S. Nastase. How to derive the rms value of a triangle waveform, 2018. URL https://masteringelectronicsdesign.com/how-to-derive-the-rms-value-of-a-triangle-waveform/.

[126] Hisham M Shehata, Muhammad R Hajj, Craig A Woolsey, and Saad Ragab. Effects of flexible propulsors on hydrodynamic forces. *IFAC-PapersOnLine*, 52(21):14–20, 2019.

[127] Daegyoum Kim, Julia Cossé, Cecilia Huertas Cerdeira, and Morteza Gharib. Flapping dynamics of an inverted flag. *Journal of Fluid Mechanics*, 736, 2013.

[128] Benjamin SH Connell and Dick KP Yue. Flapping dynamics of a flag in a uniform stream. *Journal of fluid mechanics*, 581:33–67, 2007.

[129] Jamal S Alrowaijeh and Muhammad R Hajj. Piezoelectric energy harvesting from flexible delta wings. *Theoretical and Applied Mechanics Letters*, 8(4):267–271, 2018.

[130] Chang-Kwon Kang, Hikaru Aono, Carlos Cesnik, and Wei Shyy. A scaling parameter for the thrust generation of flapping flexible wings. In *49th AIAA Aerospace Sciences Meeting including the New Horizons Forum and Aerospace Exposition*, page 1313.

[131] S Heathcote, D Martin, and I Gursul. Flexible flapping airfoil propulsion at zero freestream velocity. *AIAA journal*, 42(11):2196–2204, 2004.

[132] Matthew R Kramer, Zhanke Liu, and Yin L Young. Free vibration of cantilevered composite plates in air and in water. *Composite Structures*, 95:254–263, 2013.

[133] CE Brennen. A review of added mass and fluid inertial forces. department of the navy. *Port Hueneme, CA, USA*, 1982.

[134] Haci Sogukpinar. Numerical simulation of 4-digit inclined naca 00xx airfoils to find optimum angle of attack for airplane wing. *Uludag University Journal of The Faculty of Engineering*, 22(1):169–178, 2017.

[135] Dong Zhang, Guang Pan, Liming Chao, and Ya Zhang. Effects of reynolds number and thickness on an undulatory self-propelled foil. *Physics of Fluids*, 30(7):071902, 2018.

[136] MA Ashraf, J Young, and JCS Lai. Reynolds number, thickness and camber effects on flapping airfoil propulsion. *Journal of Fluids and structures*, 27(2):145–160, 2011.

[137] DN Beal, FS Hover, MS Triantafyllou, JC Liao, and George V Lauder. Passive propulsion in vortex wakes. *Journal of Fluid Mechanics*, 549:385–402, 2006.

[138] Mayuresh J Patil. From fluttering wings to flapping flight: The energy connection. *Journal of Aircraft*, 40(2):270–276, 2003.

[139] Mayuresh J Patil and Dewey H Hodges. On the importance of aerodynamic and structural geometrical nonlinearities in aeroelastic behavior of high-aspect-ratio wings. *Journal of Fluids and Structures*, 19(7):905–915, 2004.

[140] Hisham M Shehata, Craig A Woolsey, and Muhammad R Hajj. Hydrodynamic performance of a modular biolocomotion emulator. *IFAC-PapersOnLine*, 52(21):1–7, 2019.

[141] Colton Beardsley, Luke Bergeron, Alex McLean, Khanh Nguyen, Minh Vu, Charles Watson, Ahmad Nayfeh, Hisham Shehata, Craig Woolsey, and Muhammad Hajj. A modular biolocomotion emulator for hydrodynamic testing in a towing tank. In *OCEANS 2018 MTS/IEEE Charleston*, pages 1–8. IEEE, 2018.

[142] Allen T Chwang and T Yao-Tsu Wu. Hydromechanics of low-reynolds-number flow.

part 1. rotation of axisymmetric prolate bodies. *Journal of Fluid Mechanics*, 63(3): 607–622, 1974.

[143] Eric Limacher, Chris Morton, and David Wood. Generalized derivation of the added-mass and circulatory forces for viscous flows. *Physical Review Fluids*, 3(1):014701, 2018.

[144] J. G. Leishman and k. Q. Nguyen. State-space representation of unsteady airfoil behavior. *AIAA Journal*, 28(5):836–844, 1990.

[145] Steven L Brunton, Clarence W Rowley, and David R Williams. Reduced-order unsteady aerodynamic models at low reynolds numbers. *Journal of Fluid Mechanics*, 724:203–233, 2013.

[146] F. Bullo and A. D. Lewis. *Geometric control of mechanical systems*. Applied Mathematics. Springer-Verlag, Berlin, Germany, 2004.

[147] Ahmed A Hussein, Muhammad R Hajj, Samir M Elkholy, and Gamal M ELbayoumi. Dynamic stability of hingeless rotor blade in hover using padé approximations. *AIAA Journal*, pages 1769–1777, 2016.

[148] Z Jane Wang, James M Birch, and Michael H Dickinson. Unsteady forces and flows in low reynolds number hovering flight: two-dimensional computations vs robotic wing experiments. *Journal of Experimental Biology*, 207(3):449–460, 2004.

[149] Ahmed M Hassan and Haithem E Taha. Differential-geometric-control formulation of flapping flight multi-body dynamics. *Journal of Nonlinear Science*, 29(4):1379–1417, 2019.

[150] David William Allen. *Gait and Morphology Optimization for Articulated Bodies in Fluids*. PhD thesis, Virginia Tech, 2016.

[151] Robert T Jones. *The Unsteady Lift Of A Wing Of Finite Aspect Ratio*. US Government Printing Office, 1940.

Appendices

Appendix A

Formulation of Theodorsen's and state-space models

Theodorsen's model [3]

The total unsteady lift (L) per unit span can be categorized as non-circulatory and circulatory forces:

$$L(t) = L_{\mathrm{NC}}(t) + L_{\mathrm{C}}(t) \tag{A.1}$$

where subscripts 'NC' and 'c' denote Non-circulatory and Circulatory forces respectively. The lift force can be written as:

$$L = \underbrace{\pi\rho b^2\left(\ddot{h} + U_\infty\dot{\alpha} - ba\ddot{\alpha}\right)}_{\text{Non-circulatory}} + \underbrace{2\pi\rho U_\infty b\left(\dot{h} + U_\infty\alpha + b(\frac{1}{2} - a)\dot{\alpha}\right)}_{\text{Quasi-steady}} C(k) \tag{A.2}$$

Using $C_L = L/\frac{1}{2}\rho U_\infty^2 c$, the non dimensional lift coefficient per unit span can be written as:

$$C_L = C_{L_{\mathrm{NC}}} + C_{L_{\mathrm{QS}}} C(k) \tag{A.3}$$

Here $C_{L_{\mathrm{QS}}}$ is the quasi-steady lift coefficient, and $C(k)$ is the Theordorsen's transfer function that accounts for the influence of the shed wake vorticity. The transfer function $C(k)$ is a

complex number that represents a deficiency (or enhancement) in magnitude and a phase shift as a result of vortex shedding that varies with a change in oscillatory frequency (reduced frequency k).

The prescribed motion $\alpha(t) = \alpha_0 + \alpha_{\mathrm{A}}\sin(\omega t)$ is used in Thodorsen's analytical expression for lift coefficient:

$$C_L = \underbrace{\frac{\pi b}{U_\infty^2}\left(\ddot{h} + U_\infty\dot{\alpha} - ba\ddot{\alpha}\right)}_{\mathrm{Non-circulatory}} + \underbrace{2\pi\left(\frac{\dot{h}}{U_\infty} + \alpha + b(\frac{1}{2} - a)\frac{\dot{\alpha}}{U_\infty}\right)C(k)}_{\mathrm{Circulatory}} \tag{A.4}$$

The first group of terms is the non-circulatory component that accounts for the inertia forces due to the unsteady motion of the wing in the fluid. These forces are a function of pitching rate and acceleration $\dot{\alpha}$ and $\ddot{\alpha}$, as well as plunging rate and acceleration $\dot{h}$ and $\ddot{h}$. The second group of terms is the circulatory forces generated due to the quasi-steady lift in addition to the lift generated by circulation around the airfoil, and these forces are a function of $\dot{\alpha}$, and α, or alternatively, the effective angle of attack, α_{eff}. For a pure pitching case and in the absence of plunge motion ($h = 0$), α_{eff} is expressed as:

$$\alpha_{\mathrm{eff}} = (\frac{\dot{h}}{U_\infty} + \alpha + b(\frac{1}{2} - a)\frac{\dot{\alpha}}{U_\infty}) \tag{A.5}$$

Eq. (A.4) can be written as :

$$C_L = \frac{\pi b}{U_\infty^2}\left(U_\infty\dot{\alpha} - ba\ddot{\alpha}\right) + 2\pi\left(\alpha + b(\frac{1}{2} - a)\frac{\dot{\alpha}}{U_\infty}\right)C(k) \tag{A.6}$$

In simpler form, the unsteady lift is:

$$C_L = C_{L_{\mathrm{NC}}} + 2\pi\alpha_{\mathrm{eff}} C(k) \tag{A.7}$$

where $C_{L_{\mathrm{NC}}}$ is the non-circulatory lift coefficient, and the the term $2\pi\alpha_{\mathrm{eff}} C(k)$ is the circulatory lift coefficient. The full expression in Eq. A.6 is modeled and compared with the experimental results. Instead of the $2\pi\alpha_{\mathrm{eff}}$ from potential flow theory, the slope of the experimental static lift curve was used to formulate the quasi-steady model. Secondly, the transfer function $C(k)$ in the circulatory lift term was implemented using the magnitude and the phase approximations from potential flow theory (Bisplinghoff et al. [110]). The non-circulatory component of lift remains was computed also with potential flow theory.

State-space model [5]

In addition to Theodorsen's model, building a state space-model for the given problem to predict the unsteady lift for an arbitrary motion can be formulated. The state-space formulation developed by Taha et al. [5] applies Duhamel's principle in linear unsteady flows for non-conventional lift curves to capture the transient effects, and predict the lift from unsteady airfoil motions.

The state-space model is applied using the measured positions, $\alpha(t)$, for each waveform determined by the potentiometer. With these measurements, a quasi-steady circulation is computed as a state variable input, and integrated with Wagner's step response to output the non-linear effects of LEV as a result of lift modulation due to the input of arbitrary motion. To obtain approximations for $\dot{\alpha}$ and $\ddot{\alpha}$, we applied the central difference scheme for the first and second-order time derivative with a time step of $= 0.01$, equal to the sampling frequency used in acquiring the potentiometer readings.

Duhamel's superposition principle is extended to accommodate an arbitrary static $C_{\mathrm{L}-\alpha}$

curve and free stream velocity $U(s)$. An integral written in s-domain (Laplace transform) is:

$$l(s) = \rho U(s)\big(\Gamma_{QS}(0)W(s) + \int_0^s \frac{d\Gamma_{QS}(\sigma)}{d\sigma} W(s-\sigma)d\sigma\big) \tag{A.8}$$

where $\Gamma_{QS} = \frac{1}{2}cU(s)C_L(s)$ represents the quasi-steady circulation , and $C_L(s)$ is the quasi-steady lift obtained from the experimental static lift curve at our operating flow regime of Re= 2.1x10^4.

For a constant free stream velocity, Eq. (A.8) can be written in state-space form. A finite-state approximation for Wagner's function, $W(s)$, as suggested by Jones [151] is:

$$W(s) = 1 - A_1 e^{-c_1 s} - A_2 e^{c_2 s} \tag{A.9}$$

where the constants in Eq. (A.9) are $A_1 = 0.0355$, $A_2 = 0.06$, $c_1 = 0.044$, $c_2 = 0.043$.

$$\dot{x}_i(t) = \frac{2b_i U(t)}{c}\big(- x_i(t) + A_i \Gamma_{QS}(t)\big) \quad \text{i} = 1{,}2 \tag{A.10}$$

The solution to the linear differential equation Eq. (A.10) is given by

$$x_i(t) = \int_0^t U(\tau) A_i \frac{2b_i}{c} U(\tau) e^{\frac{-2b_i}{c}\int_0^t U(\tau)d\tau} d\tau \tag{A.11}$$

The circulatory lift per unit span finally becomes:

$$l(t) = \rho U(t)\big[(1 - A_1 - A_2)\Gamma_{QS}(t) + x_1(t) + x_2(t)\big] \tag{A.12}$$

Appendix B

Snapshots Of Passive Tail Responses

In this section, we display top-view snapshots of the tail's deformation as a result of leading edge oscillations. The maximum tail tip amplitude for panel 'b' was observed at 1 Hz. The maximum tail tip amplitude for panel 'c' was observed at 0.75 Hz. You will also notice that panel 'c' responds beyond the first bending mode at frequency inputs above 1 Hz. Both panels are subjected to an 8° leading edge angular amplitude.

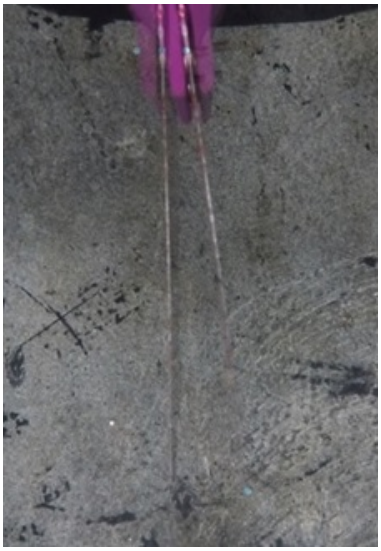

(a) 0.5 Hz

(b) 0.75 Hz

(c) 1 Hz

(d) 1.5 Hz

(e) 2 Hz

Figure B.1: Tail deformations generated by panel 'b' subjected to various frequency inputs.

(a) 0.5 Hz

(b) 0.75 Hz

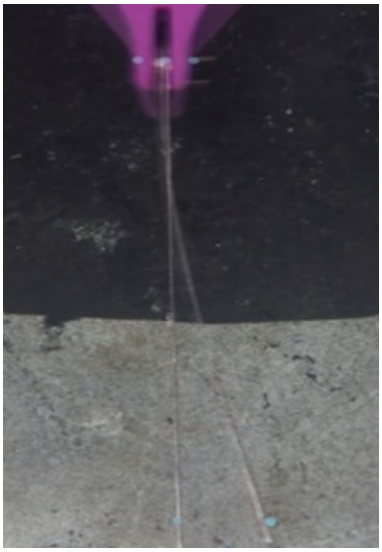

(c) 1 Hz

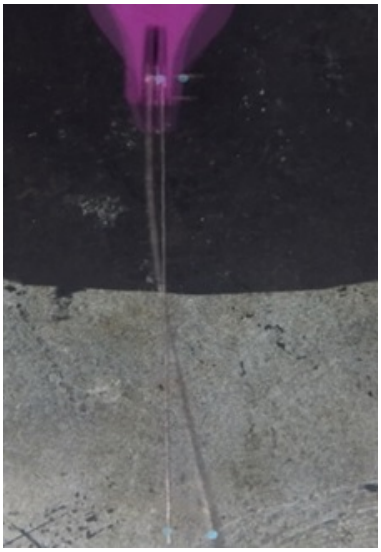

(d) 1.5 Hz

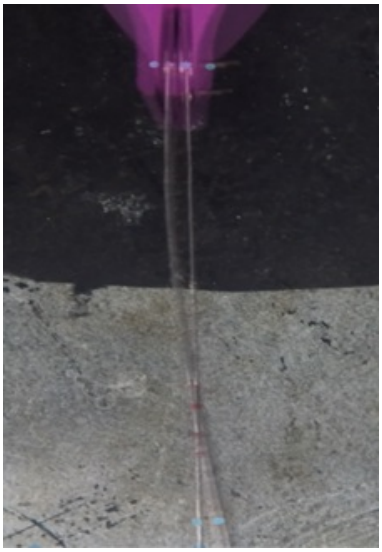

(e) 2 Hz

Figure B.2: Tail deformations generated by panel'c' subjected to various frequency inputs.

Appendix C

An Initial Guide To Geometric Control On The *MBE*

The modeling of an N-link prototype involves several steps. The first is to express the 3-D equation of motions for a 3-link prototype. The second is to develop a hydrodynamic model based on the quasi-steady assumption and experimental data. Third, is to use tools from geometric control theory [83] to assess control authority and design time-varying control laws for piscifform locomotion. A free-body diagram of the current *MBE* is shown in Figure C.1. The dynamics of the *MBE* can be derived using the Lagrangian:

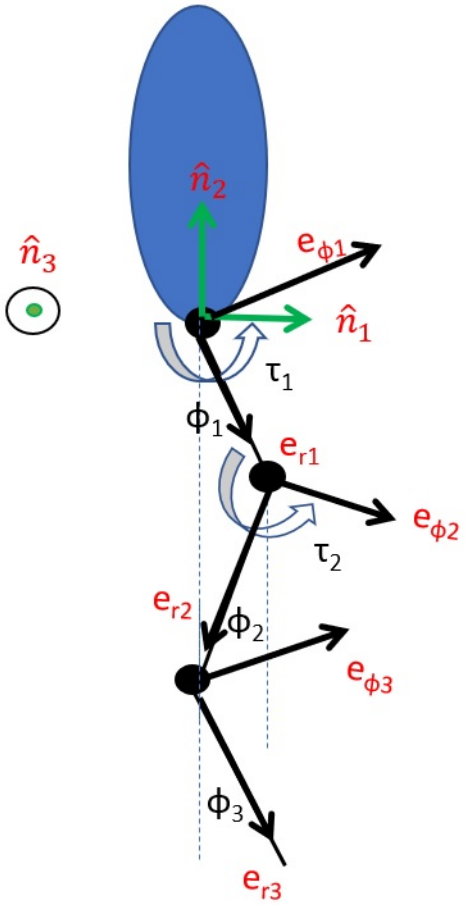

Figure C.1: Dynamic representation of the *MBE*.

$$\frac{d}{dt}\frac{\partial L}{\partial \dot{q}} - \frac{\partial L}{\partial q} = Q \tag{C.1}$$

Here, $q^T = \begin{bmatrix} \text{x} & \theta_1 & \theta_2 & \theta_3 \end{bmatrix}$ are the generalized coordinates in a uniform flow, and Q represents the external forces due to hydrodynamic effects (forces and torques), and control inputs. The MBE is restricted in motion in y and z directions, and the MBE tail can be actuated using three independently controlled servos with angles θ_1, θ_2, θ_3 relative to the inertial frame, each generating torques τ_1, τ_2 and τ_3. Explicitly, we can write the equation of motion as:

$$M\big(q\big)\ddot{q} + C\big(q, \dot{q}\big)\dot{q} = Q_H + Q_C \tag{C.2}$$

Where M is the mass matrix that includes translation and rotation rigid body, and added mass inertia, and C matrix represents the coriolis and centripetal effects. The generalized forces include the control inputs, Q_C and the hydrodynamic force responses Q_H. We can denote the control inputs as u_x, u_{θ_1}, u_{θ_2}, u_{θ_3} and hydrodynamic effects as H_x, H_y, H_z, H_{θ_1}, H_{θ_2}, H_{θ_3}. The hydrodynamic effects can be determined experimentally from the axial force, C_T, lateral force, C_L, yaw moment C_N, and hydrodynamic torques τ_1, τ_2, τ_3 at each link. We now have

$$\begin{pmatrix} \mathrm{Q}_x \\ \mathrm{Q}_y \\ \mathrm{Q}_z \\ \mathrm{Q}_{\theta_1} \\ \mathrm{Q}_{\theta_2} \\ \mathrm{Q}_{\theta_3} \end{pmatrix} = \begin{pmatrix} \mathrm{H}_x \\ \mathrm{H}_y \\ \mathrm{H}_z \\ \mathrm{H}_{\theta_1} \\ \mathrm{H}_{\theta_2} \\ \mathrm{H}_{\theta_3} \end{pmatrix} + \begin{pmatrix} \mathrm{u}_x \\ 0 \\ 0 \\ \mathrm{u}_{\theta_1} \\ \mathrm{u}_{\theta_2} \\ \mathrm{u}_{\theta_3} \end{pmatrix}$$

One can further explore the development of hydrodynamic models by initially assuming quasi-steady hydrodynamics. The quasi-steady hydrodynamic model can be formulated using the thrust, force, lateral force, and yaw moment coefficients determined from the experimental data as state-space variables.

The geometric control of the pisciform can utilize averaging theories for mechanically controlled systems using tools and techniques from Vela et al. [81, 82], Bullo [83] and Morgansen et al. [64].

In the context of underwater vehicles, for a mechanically controlled system, Vela et al. [81, 82] describes Bullo's work, [83] by relaxing some assumptions. Vela et al. [81] represents the dissipation term in the dynamic model as:

$$E(q, \dot{q}) = E_0(q, \dot{q}) + R(q)\dot{q} \tag{C.3}$$

C.3 defines the effects of generalized coordinates that are linear and quadratic in velocity. The term E_0 can represent axial, lateral, and yaw moments that can have non-linear dependence on the generalized coordinates.

Given the configuration of the system here (one forebody, two faired modules, and one trailing

edge hydrofoil), the set of external forces on the system can be divided into a lift and drag acting on each link. The two peduncles can be approximated as ellipsoids with forces acting on their center of mass, and the tail can be modeled as an airfoil, with forces acting from the quarter chord. The added mass in the direction of the accelerated object is one source of fluid force transmission. The other mechanism of force transmission is through the lift and drag, which are resolved in orthonormal components as a result of pressure differential. Forces can be expressed as a lump sum on the body and each link. The hydrodynamic model can initially be assumed to be inviscid, irrotational, and incompressible. These assumptions place limits on the accuracy of the behavior of the model, which represents a finite space where 3-D fluid effects are significant.